UNIVERSITY OF MODENA AND REGGIO EMILIA

“Enzo Ferrari” PhD in “Industrial and environmental engineering”

32nd cycle

ANALYSIS OF ULTRA HIGH PERFORMANCE CONCRETE (UHPC)-FILLED STEEL TUBE COLUMNS CYCLIC BEHAVIOR

in cooperation with Fuzhou University

Applicant: ZHOU Jun

Italian Tutoring Professor: Angelo Marcello Tarantino

Chinese Tutoring Professor: Bruno Briseghella

PhD Programme Coordinator: Professor Alberto Muscio

UNIVERSITÀ DEGLI STUDI
DI MODENA E REGGIO EMILIA

Dottorato di ricerca in "*Enzo Ferrari*" in "Ingegneria industriale e del territorio"

Ciclo XXXII

ANALISI DEL CONCRETO DI ALTA PRESTAZIONE (UHPC)-TOBE COLUMNS CICLI

in cooperazione con Fuzhou Università

Candidata: ZHOU Jun

Relatore italiano (Tutor): Prof. Angelo Marcello Tarantino

Relatore cinese (Tutor): Prof. Bruno Briseghella

Coordinatore del Corso di Dottorato: Prof. Alberto Muscio

Abstract

Ultra-high performance concrete (UHPC)-filled steel tube (UCFST) column is a kind of new-type composite structure which is made by filling UHPC into steel tube. It can fully exert the tensile properties of steel tube and avoid the high brittleness of UHPC. Thus, it can improve the force-bearing performance of the composite structure. Nowadays, research on UCFST structure mainly focuses on its static behavior, and the research on hysteretic behavior of this new composite structure is quite rare. Therefore, in this paper, the cyclic behavior of UCFST columns were studied by combining the experimental study and finite element analysis. The main work carried out and the main conclusions obtained are as follows:

(1) Referring to the existing static tests of UCFST columns and quasi-static tests of normal concrete-filled steel tube (CFST) columns, the quasi-static tests of eight UCFST columns were carried out. The effects of axial compression ratio and steel ratio on the hysteretic behavior of the columns were investigated experimentally. The experimental results showed that integral bending failure were occurred in all the specimens. And with the increase of axial compression ratio, the bending capacity of the specimen increased firstly and then decreased, while the ductility and energy dissipation capacity decreased a lot. Furthermore, the bending capacity, ductility and energy dissipation capacity all increased in different magnitude as the steel ratio increased.

(2) According to the research results of UCFST columns static tests, the constitutive model of confined concrete was selected appropriately firstly in this paper and the finite element program OpenSEES was adopted to establish UCFST column models under cyclic load. Furthermore, the influence of axial compression ratio, steel

ratio, steel yielding strength and concrete strength on the plastic bending behavior of UCFST columns was analyzed expandingly by the verified finite element model. And the results of finite element analysis showed that steel ratio, core concrete strength and axial compression ratio were the main parameters that affect the elasticity stiffness of UCFST columns. The yield moment and yield curvature of UCFST columns were mainly affected by steel ratio, steel yielding strength and core concrete strength. And the parameters such as axial compression ratio, steel ratio, steel strength and so on would affect the curvature ductility coefficient of UCFST columns.

(3) According to the results of quasi-static tests and finite element analysis, the bending moment-curvature skeleton curve of UCFST columns can be the well simulated by using the tri-line model. Referring to CFST column theory, the simplified calculation formulas of each characteristic point in the moment-curvature skeleton curve of UCFST columns were obtained by data fitting method. And the characteristic points included the elasticity stiffness, the yield moment, the yield curvature and the strengthening phase stiffness. Finally, the data of quasi-static tests and finite element analysis were used to verify the tri-line model on the bending moment-curvature curve of UCFST columns proposed in this paper, which can provide reference for the research on the seismic behavior of UCFST columns in the future.

Sommario

La colonna di tubi in acciaio rivestiti in calcestruzzo ad alte prestazioni è una sorta di struttura composita di nuovo tipo che viene realizzata riempiendo UHPC in tubi in acciaio.Può esercitare pienamente le proprietà di trazione del tubo di acciaio ed evitare l'elevata fragilità dell'UHPC.In questo modo, può migliorare le prestazioni di forza della struttura composita.Oggi, la ricerca sulla struttura UCFST si concentra principalmente sul suo comportamento statico, e la ricerca sul comportamento isteretico di questa nuova struttura composita è piuttosto rara.Pertanto, in questo documento, il comportamento ciclico delle colonne UCFST è stato studiato combinando lo studio sperimentale e l'analisi degli elementi finiti.I principali lavori svolti e le principali conclusioni raggiunte sono i seguenti:

(1) Facendo riferimento alle prove statiche esistenti delle colonne UCFST e alle prove quasi statiche delle normali colonne di tubi in acciaio riempiti in calcestruzzo, sono state effettuate le prove quasi statiche di otto colonne UCFST.Gli effetti del rapporto di compressione assiale e del rapporto di acciaio sul comportamento isteretico delle colonne sono stati studiati sperimentalmente. I risultati sperimentali hanno dimostrato che in tutti gli esemplari si sono verificati guasti integrali alla curvatura.E con l'aumento del rapporto di compressione assiale, la capacità di curvatura del campione è aumentata in primo luogo e poi diminuita, mentre la capacità di dissipazione dell'energia e della duttilità è diminuita molto.Inoltre, la capacità di flessione, di duttilità e di dissipazione dell'energia è aumentata in misura diversa con l'aumento del rapporto acciaio.

(2) Secondo i risultati di ricerca dei test statici delle colonne UCFST, il modello costitutivo del calcestruzzo confinato è stato selezionato in modo appropriato in primo

luogo in questo foglio e il programma degli elementi finiti OpenSEES è stato adottato per stabilire modelli di colonne UCFST sotto carico ciclico.Inoltre, l'influenza del rapporto di compressione assiale, del rapporto di acciaio, dell'acciaio che produce forza e forza concreta sul comportamento di curvatura plastica delle colonne UCFST è stata analizzata espandidamente dal modello di elemento finito verificato.E i risultati dell'analisi degli elementi finiti hanno dimostrato che il rapporto acciaio, la forza di calcestruzzo e il rapporto di compressione assiale erano i parametri principali che influenzano la rigidità di elasticità delle colonne UCFST.Il momento di resa e la curvatura delle colonne UCFST sono stati influenzati principalmente dal rapporto di acciaio, dall'acciaio che produce forza e dalla forza di calcestruzzo di base.E i parametri come il rapporto di compressione assiale, il rapporto di acciaio, la resistenza in acciaio e così via influenzano il coefficiente di duttilità di curvatura delle colonne UCFST.

(3) In base ai risultati delle prove quasi -statiche e dell'analisi degli elementi finiti, la curva di curvatura della curva del momento -curvatura delle colonne UCFST può essere ben simulata utilizzando il modello a tre linee.Per quanto riguarda la teoria della colonna CFST, le formule di calcolo semplificate di ciascun punto caratteristico della curva scheletrica di curvatura del momento delle colonne UCFST sono state ottenute con il metodo di montaggio dei dati.E i punti caratteristici includono la rigidità di elasticità, il momento di resa, la curvatura della resa e la rigidità di fase di rafforzamento.Infine, i dati delle prove quasi statiche e dell'analisi degli elementi finiti sono stati utilizzati per verificare il modello tri -line sulla curva di curvatura del momento -curvatura delle colonne UCFST proposte in questo documento, che può fornire un riferimento per la ricerca sul comportamento sismico delle colonne UCFST in futuro.

Contents

List of Figures

List of Tables

Chapter 1

Introduction

1.1 Research background and significance

In order to give full play to the characteristics of high compressive strength of concrete and high toughness of steel tube, as early as the 1990s, people combined them to form a composite structure, that is, concrete filled steel tube (CFST) structure (Han, 2004; Zhong, 2006). Compared with empty steel tube or normal concrete structure, this kind of composite structure not only avoids the buckling problem of empty steel tube under load, but also avoids the shortcomings of brittleness and low tensile strength of concrete. It greatly improves the performance of the two materials, so it is widely used in various buildings and bridge structures (Zhong, 2001). However, with the rapid development of economy, the shortage of construction land area, the buildings height needs to be higher and the bridges span needs to be larger. As a result, the bearing capacity requirement of CFST structure is higher and higher (Wei, 2011). As we know, most of the core concretes of CFST structures are normal concrete with heavy self-weight, low strength and poor durability. In order to satisfy the bearing capacity requirements of these buildings and bridges, it is necessary to increase the section area of CFST structures. However, too large cross-sectional area will occupy a large amount of using space, will also affect the aesthetic shape of the structure. And it is not suitable for modern architectural concepts. What's more, these shortcomings will also affect and limit the using scope of CFST structures.

Considering the economy, some scholars have improved the CFST structure in the late 1990s to meet the different requirements of modern architecture. They mainly

studied the concrete material, that is, replacing normal concrete with ultra high performance concrete (UHPC) (Ghafari et al., 2015; Schmidt and Fehling, 2005; Chen et al., 2014) to form UCFST structures (Meng and Chen, 2003; Yang, 2003). Compared with normal concrete, UHPC has a better advantage. Its compressive strength and tensile strength can reach more than 150 MPa and more than 10 MPa, respectively (Federal, 2006; Aziz and Ahmed, 2012). In order to meet the needs of structures with large-span (such as bridges) and buildings in harsh environments, the internal micro-cracks of UHPC can be further reduced and its tensile strength and durability can be improved by improving compactness, reducing porosity and adding fibers (Bonneau and Pouhn, 1996). Thus, UHPC has become a new research hotspot in the field of international engineering materials (Philippot and Korb, 1998; Prabha et al., 2010; Zdeb and Sliwinski, 2011). Nowadays, UHPC has been applied in a lot of architectures in many countries. According to incomplete statistics, many UHPC bridges have been built in the word (Du, 2014; Du et al., 2013).

UHPC has high compressive strength and elasticity modulus, but the toughness and brittleness of plain UHPC (here refers to UHPC without steel fiber) are poor. Many scholars have found that UHPC without steel fiber will produce burst failure under high or complex stress conditions (Shi et al., 2011). However, UHPC without steel fiber can be combined with steel tube to form a new composite structure, i.e. UCFST structure, instead of normal concrete. And the UCFST structure can not only give full play to the advantages of high compressive strength of UHPC, but also greatly improve its ductility, which is more economical and reasonable. Its stress state is showed in Fig. 1-1. Due to the confinement of the outer steel tube, the core UHPC is in a three-dimensional compressive state. At the meantime, because of the restriction of UHPC, the steel tube is also in a three-dimensional stress state and is not easy to buckle. As a result, the bearing capacity and ductility of UCFST structure are greatly improved.

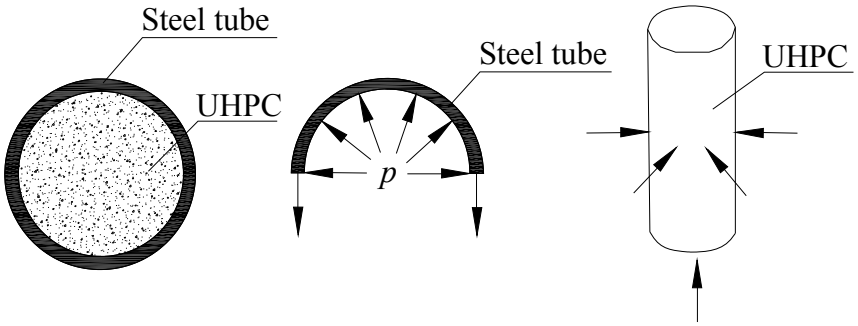

Fig. 1-1 Three-dimensional stress state diagram of UCFST structure

Compared with CFST structure, there are several advantages in UCFST structure, which are as follows:

(1) Coarse aggregate is not contained in UHPC. Thus, with higher fluidity and stronger self-compaction, UHPC is more suitable for combining with steel tube to form as UCFST structure.

(2) UCFST structure has a very high compressive strength because of the high strength of UHPC. And due to this advantage, UCFST structure can further reduce the occupied space and improve the utilization of space. At the same time, it can lighten the self-weight of bridge structure, which is beneficial to the shape design of bridge.

(3) The application of UCFST structure can reduce the amount of sand and cement to improve the economic benefit. At the same time, the use of high-performance materials can reduce energy and resource consumption and add new vitality to the development of composite structure technology.

However, most of the existing research is focused on the static behavior of UCFST members, while the hysteretic behavior of UCFST members is insufficient. And the research on UCFST members shows that there are some differences in static behavior between UCFST structure and CFST structure. The existing theory of static behavior of CFST members cannot be fully applied to UCFST members. At the same time, the research on static behavior of UCFST members is the basis of experimental analysis and theoretical research on hysteretic behavior of UCFST members. Thus, the hysteretic behavior theory of CFST members cannot be fully applied to UCFST members, which leads to the lack of relevant seismic behavior test and theoretical

guidance for the application of UCFST structures. Therefore, it is of great value to study the hysteretic behavior of UCFST structures.

1.2 Research status

Most of the research methods for the static and dynamic behaviors of CFST structures are based on the "confinement coefficient" as the basic parameter, and then experiments and theoretical analysis are carried out. Thus, there is a relatively complete theoretical research system of CFST structures. However, research on UCFST structures mainly focuses on its mechanical properties, such as axial compression behavior, eccentric compression behavior and behavior under bending stress. While the research on hysteretic behavior of UCFST structures is relatively lagging, and the corresponding research is quite rare nowadays.

1.2.1 Static behavior of CFST structures

As we all know, CFST structures have been widely used in buildings and bridges since 1990s. After varies of engineering applications, it is found that CFST members are generally in a complex stress state, rather than unidirectional force state. Due to this fact, scholars in different countries did many researches of CFST members through adopting the combination method of theory and experiment, and they also use finite element analysis to verify their research method.

After summarizing a lot of data, Zhong (2006) put forward that CFST structures should be taken as a whole to study the combined performance, and obtained the combined performance indicators such as the combined compressive yield point, the combined axial compressive elasticity modulus and the combined bending elasticity modulus, etc. On this basis, the formulas for calculating bending capacity of CFST members under complex stress state were derived by using finite element method and experimental method.

Cai and Jiao (1984), Gu and Cai (1991), Cai and Di (1985) carried out a lot of tests on the axial and eccentric bearing capacity of CFST short and long columns with the

parameters of "confinement index", loading form, slenderness ratio and eccentricity ratio, etc. The results showed that " confinement index" was the main factor affecting the bearing capacity of short columns; slenderness ratio was the main factor affecting the bearing capacity of long columns; slenderness ratio and eccentricity ratio were the main factors affecting the eccentric bearing capacity of long columns. Based on the ultimate equilibrium theory, the simplified formulas for calculating the bearing capacity of short columns, long columns and eccentrically loaded columns were derived and verified by many experimental data.

Based on the "unified theory", Han (2004) carried out a lot of tests and numerical analysis on CFST members under unidirectional and composite loads. Based on the statistics and comparison of many test results of CFST short columns, a longitudinal stress-strain relationship model of confined concrete with "confinement coefficient" as the main index was then proposed. Han adopted the "fiber model method" to compute the mechanical properties of CFST members. In the method, the double-broken line model of "Bauschinger effect" was used as the steel tube stress-strain relationship model. Based on the results of a large number of tests and numerical calculations, simplified formulas for calculating the ultimate bearing capacity of axial compression members, the ultimate bearing capacity of pure bending members and the bending bearing capacity of compression-bending members were deduced, which took the "confinement coefficient" as the main index. Furthermore, the formulas were verified by a large experimental data, and showed a good agreement.

On the premise of the proposed numerical constitutive model of CFST members and the calculation method of ultimate bending capacity of pure bending CFST members, Ding et al. (2009) studied the relationship curve of axial force-bending moment-curvature of CFST compression-bending members by the method of cross-section stratification. And, he determined the formula influence coefficient of axial force-bending moment-curvature by deduction and regression. Finally, the calculation model and calculation method were put forward.

Based on the assumption of flat section, no slip and no shear, Li et al. (2016) adopted the constitutive model of core concrete and steel tube provided by Han Linhai and used strip method to analyze the axial force-moment-curvature curve of CFST compression-bending members. The coefficient n_0 related to the concrete compressive strength was deduced theoretically. Lastly, the calculation formula of the axial force-moment curve of CFST members was established through data fitting.

Adopting the confined constitutive model of compressive concrete proposed by Sun Yuping, the tension confined constitutive model of concrete proposed by Guo Zhenhai and the rational elastic-plastic constitutive model of steel tube, Qian et al. (2004) firstly carried out bending tests on twelve specimens of high-strength concrete filled steel tube (HCFST) members, and then calculated the moment-curvature relationship of HCFST members by strip method. Lastly, based on the experimental results and numerical results, she proposed the moment-curvature tri-line model of HCFST members and the formulas for calculating the full curve.

1.2.2 Static behavior of UCFST structures

Because of its excellent performance, UHPC has attracted wide attention since its birth. However, due to its high brittleness, the popularization of UHPC has been hindered. To bring into full play for the characteristics of both UHPC and steel tube, UHPC can be poured into steel tube to form UCFST structure. Therefore, the advantages of UCFST structure are favored by many researchers, and a series of work on static behaviors of UCFST structure has been carried out.

Some tests on UCFST short and long columns under axial or eccentric loading were carried out in China, as well as finite element model analysis. In 2003, Wu and Lin (2005), taking UHPC strength and confinement coefficient as the main parameters and keeping the length to diameter ratio as 3, carried out the axial compression test of twenty-two UCFST short columns by means of full section loading. The stress-strain curves and ultimate failure modes of UCFST short columns during the whole loading process were studied. It was found that shear failure and buckling failure modes

occurred in UCFST columns. When the confinement coefficient was less than 0.311, the steel tube couldn’t provide enough lateral force for UHPC. Finally, a formula for calculating the bearing capacity of UCFST short columns was obtained by fitting large amounts of experimental data.

Taking confinement coefficient, UHPC strength and length to diameter ratio as the main parameters, Zhang (2003) carried out the tests of 18 UCFST short columns loaded with core UHPC only. Different formulas for calculating UCFST short columns bearing capacity in various codes in the word were compared and analyzed. Based on the experimental results, the formulas for calculating the bearing capacity of CFST columns proposed in CECS28:90 were regressed. Finally, a simplified formula for calculating the bearing capacity of UCFST short columns was established. Yang (2003) designed and tested twenty-two UCFST short columns under axial compression with parameters of loading mode, confinement coefficient, UHPC strength and length to diameter ratio. The experimental results showed that Cai Shaohuai's formula for calculating the bearing capacity of HCFST specimens based on "limit equilibrium theory" can be applied to UCFST specimens.

Feng (2008) firstly studied the mechanical properties of UHPC specimens, and then designed a series of UCFST short columns with UHPC strength and confinement coefficient as parameters. In the paper, the axial compressive properties of UCFST columns were studied, and the formulas for calculating the confinement force of UCFST columns and the bearing capacity of HCFST specimens were presented.

Taking the effect of different curing system as the main parameter, Yan et al. (2011) carried out five UCFST short columns tests with the same cross-section under full cross-section axial loading. Large amounts of test results of UCFST columns under axial compression were counted, and ultimately a formula for calculating the bearing capacity of UCFST columns was put forward based on limit equilibrium theory.

Liew and Xiong (2012) studied the effect of steel fiber on the ductility and strength of twenty-seven UCFST columns under axial compression. It was found that steel fiber have little effect on the ductility and strength of UCFST columns, but they can

greatly affect the ductility and strength of UCFST columns. Furthermore, Eurocode EC4 was used to predict the bearing capacity of UCFST columns under axial compression and verified by the test results. The results showed that the prediction of bearing capacity of UCFST columns by Eurocode EC4 was relatively low and safe.

An and Fehling (2017) took UCFST short columns as the research object and took confinement coefficient and diameter-thickness ratio as the parameters to study their effects on the strength and ductility of UCFST columns under axial compression. The effects of different codes (EC4, AISC, AIJ) on the calculation of the bearing capacity of UCFST short columns under axial compression were compared and analyzed. Finally, a formula for calculating the bearing capacity of UCFST short columns under axial compression was established.

Based on the experimental results in the literature, Patela et al. (2019) made a non-linear finite element analysis of UCFST short columns and compared it with the experimental results. The results showed that the peak load and stress-strain response of UCFST short columns under axial compression obtained by finite element simulation were in good agreement with the experimental results. Furthermore, expanded parameters of UCFST short columns were analyzed by the verified finite element method. Then the applicability of different codes (AS/NZS 5100.6, EC 4, AISC and GB 50936) for calculation of UCFST short columns was verified with the test results. And it was found that the predicted results of AS/NZS 5100.6 and EC 4 were quite ideal.

There are also several researches about UCFST long columns. Yang (2003) designed and tested nine UCFST columns with four different length to diameter ratios. The effect of length to diameter ratio on UCFST columns was preliminarily studied. Based on the results of bearing capacity of short and long UCFST columns, the formulas for calculating the stability factor under axial compression were obtained. And it was also proved that the formula for calculating the bearing capacity of HCFST members proposed by Cai Shaohuai can also be applicable to UCFST members.

Yao (2005) studied preliminarily the influence of confinement coefficient and length to diameter ratio on the bearing capacity and load-deflection curves of UCFST long columns through twelve axial compression tests. The results showed that the bearing capacity of the specimens decreased with the increase of length to diameter ratio or the decrease of confinement coefficient. Finally, based on the experimental data, the formula for calculating the stability factor of UCFST long columns was regressed, and the formula for calculating the bearing capacity of UCFST long columns was also put forward.

Zeng (2015) firstly studied the range of length to diameter ratio, confinement coefficient and eccentricity ratio, and then designed, fabricated, loaded and analyzed the specimens, and put forward the bearing capacity calculation formulas of UCFST eccentrically loaded long columns. ABAQUS software was also used to simulate the axial and biased compression of UCFST columns. And the feasibility of finite element simulation of the mechanical properties of UCFST columns was verified.

Taking slenderness ratio and confinement coefficient as the main parameters, Yang (2013) carried out an axial compression test on forty UCFST long columns, and studied the load-strain curves of the specimens during the whole loading process. At the same time, Han Linhai's confined concrete constitutive model was used to simulate the core UHPC, and ABAQUS software was adopted to establish the finite element model of UCFST columns. The results showed that the calculated results were in good agreement with the experimental results.

Luo (2015) systematically studied the compression mechanism of UCFST columns. Based on the "limit equilibrium theory" and "unified strength theory", the calculation formulas for the bearing capacity of UCFST short and long columns were proposed. The elastic-plastic analysis of steel tube members, core UHPC members and UCFST members was carried out through the combination of experiment and theory. Finally, based on the confined concrete constitutive model of Han Linhai, a confined constitutive model suitable for the core UUPC was proposed.

In summary, by comparing the static behavior of CFST structure with that of

UCFST structure, it can be found that the calculation methods of axial compressive bearing capacity, bending capacity and axial force-moment curve of CFST members have been verified in practice. However, due to that the stress-strain relationship of the core UHPC of UCFST columns has not yet been universally applied, most of the formulas of bearing capacity under axial and eccentric loads are semi-empirical and semi-theoretical. Thus, there is no relevant research on the bending capacity and the axial force-moment curve of UCFST members. In addition, by comparing the axial and eccentric compression test results of UCFST column and CFST column, it can be found that there is a great difference between them. As a result, the original theory of CFST members cannot be applied to UCFST members.

1.2.3 Hysteretic behavior of CSFT structures

Hysteretic behavior includes moment-curvature and load-displacement hysteretic relationship. In order to study the strength, stiffness and ductility of UCFST members under seismic load, it is necessary to determine its hysteretic model. For the hysteretic behavior of CFST members, experimental research and numerical analysis are mainly adopted as the research methods. Nowadays, the research on hysteretic behavior of UCFST members is insufficient. And the existing research on hysteretic behavior of CFST members can provide reference for that of UCFST members.

Wakabayashi (1988) conducted an experimental study on CFST piers in order to obtain the effect of steel tube on concrete piers under cyclic compression, bending and shear loads. The test results showed that steel tube can greatly improve the hysteretic behavior of reinforced concrete piers.

Sakino and Tomii (1981) designed and tested fifty concrete filled square steel tubular (CFST) compression-bending members with the main parameters of axial compression ratio and section length-width ratio. It was found that with the increase of section length-width ratio and axial compression ratio, the specimen’s strength gradually degenerated. And at the end of loading, the specimen’s strength gradually stabilized and the specimens had a certain residual bearing capacity.

Taking axial compression ratio and diameter-thickness ratio as the main parameters, Fujinaga et al. (1997) carried out quasi-static test of CFST members with constant axial force. The results showed that with the increase of axial compression ratio and diameter-thickness ratio, the hysteretic characteristics of CFST members, such as energy consumption and ductility, decreased greatly.

Lv and Lu (2000) designed and tested twelve CSFT columns subjected to cyclic loads. The tests mainly investigated the effects of width-thickness ratio, axial compression ratio and concrete strength. And the test results showed that the energy dissipation behavior of CFST columns was better and the strength degradation was smaller than that of normal reinforced concrete columns. Wang and Zhen (2000) adopted a steel constitutive model and an improved confined concrete constitutive model that were suitable for three-dimensional loading state to carry out load-displacement finite element analysis. Six HCFST (concrete cubic strength 77 MPa) members were designed and tested to verify the finite element analysis results.

Han et al. (2003), considering the influence of width-thickness ratio, concrete strength and axial compression ratio, adopted numerical analysis method to establish a moment-curvature restoring force model on the basis of hysteretic test of CFST members. Fujimoto et al. (2014) tested the hysteretic behavior of thirty-two circular and square CFST specimens with concrete strength and axial compression ratio as the main parameters. On the basis of the tests, a correct finite element model was established and the parameters were expanded. Finally, the moment-curvature hysteretic models of circular and square CFST members were proposed respectively. Han et al. (2004) established an applicable numerical calculation method on the basis of eight quasi-static tests of CFST members with axial compression ratio as the main parameter. The hysteretic curves of moment-curvature and load-displacement of CFST members were obtained, which basically coincided with the experimental curves.

Based on the main parameters of axial compression ratio, steel yield strength and concrete strength. You and Han (2005) carried out the quasi-static tests of circular and

square HCFST members. And based on the test results, the calculation method of bearing capacity of HCFST members was proposed.

Wang (2013) used the finite element analysis software Seismo Struct to simulate the hysteretic model of CFST members. And the hysteretic curves obtained by the finite element method were compared with the experimental curves to verify the accuracy of method. On this basis, twelve CFST piers of original bridge sizes with the parameters of axial compression ratio, diameter-thickness ratio and slenderness to diameter ratio were established, and their hysteretic behavior under different parameters was studied.

Yan (2015) firstly established the CFST arch bridge model by using the finite element software ANSYS, and obtained the changes of the in-plane and out-of-plane bending moments of the arch bridge under earthquake action. Then the hysteretic model of CFST members was established by using finite element software ABAQUS. The accuracy of the finite element model was verified by comparing the finite element results with the experimental results. Furthermore, on the basis of the above two, the finite element model of CFST column under the action of axial force and in-plane and out-of-plane bending moments was established. Finally, the moment-curvature restoring force model of CFST members under biaxial compression and bending load was established based on the tri-line model and the multi-parameter data regression by SPSS software.

Serras et al. (2016) took diameter-thickness ratio, steel yield strength and concrete strength as parameters, and used ATENA finite element software to analyze the parameters of CFST short columns under cyclic loads. Empirical formulas for calculating ultimate strength of CFST columns were established and compared with experimental results. It was shown that the proposed analytical model could effectively describe and reliably study the mechanical behavior of CFST columns under cyclic loading.

Wang et al. (2019, 2019) proposed a new type of high-strength concrete filed high strength steel tubular (HCFHST) column. The quasi-static test of the HCFHST

column was carried out with the test parameters of concrete compressive strength, steel yield strength, axial compression ratio and diameter-thickness ratio. Based on the non-line fiber beam-column element, the relevant numerical model was established to analyze the load-displacement hysteresis curve, skeleton curve and ductility. The influence of various parameters on the hysteretic behavior of the specimens was studied, and a simplified hysteretic model was established.

In summary, research on hysteretic behavior of CFST members has been quite mature, and some scholars put forward moment-curvature restoring force model of CFST members based on experimental, numerical analysis and finite element method, and verified it with a large number of experimental and finite element data. However, most of the research about UCFST structures are mainly focused on the axial and eccentric pressure characteristic. There is no report on the moment-curvature hysteresis behavior of UCFST members. Therefore, it is necessary to draw on the research methods and results of hysteretic behavior of CFST members and carry out the research of hysteretic behavior of UCFST members, so as to provide reference for the application of such members in practical engineering.

1.3 Main Content

In this paper, the hysteretic behavior of UCFST columns was studied by means of experiment and finite element analysis and the main work is as follows:

(1) Pseudo-static tests of eight UCFST columns were firstly carried out with the main parameters of axial compression ratio and steel ratio. Then load-displacement hysteretic curves and moment-curvature hysteretic curves of UCFST columns were obtained. And the main factors affecting the ductility, energy dissipation and stiffness degradation of UCFST columns were analyzed.

(2) The general finite element software ABAQUS and the program OpenSEES were used to simulate the test results, and the accuracy of the two finite element models was verified by comparing with the test results. On this basis, OpenSEES was used to analyze the main factors affecting the hysteretic behavior of UCFST columns,

such as the axial compression ratio and the steel ratio.

(3) On the basis of the above tests and finite element analysis, referring to the calculation method of static and hysteretic performance indexes of CFST members, the simplified calculation formulas of key parameters in the bending moment-curvature skeleton curve of UCFST columns was deduced through data analysis and regression. Thus, the bending moment-curvature skeleton curve model of UCFST columns was established. And the results were compared with the experimental and finite element results to verify its accuracy.

Chapter 2

Quasi-Static Test of UCFST Columns

2.1 Test overview

2.1.1 Design of specimen parameters

Referring to the moment-curvature research of CFST columns (Han, 2004), eight UCFST columns with different axial compression ratios (varying from 0.03 to 0.11) and steel ratios (varying from 0.275 to 0.361) were designed, as shown in Table 2-1. The nomenclature of the specimens (e.g., GU-T8-N03) was designed as follows: G referred to the steel tube, U referred to the UHPC, T8 indicated that the thickness of the steel tube was 8 mm, and N03 indicated that the axial compression ratio (n) was 0.03.

Table 2-1 Main parameters of UCFST columns

Specimen number	Steel tube diameter D (mm)	t (mm)	L_s (mm)	f_y (MPa)	f_{cu} (MPa)	α	N_0 (kN)	$n=N_0/N_u$
GU-T8-N03	140	8	1900	390	153	0.275	111	0.03
GU-T8-N06	140	8	1900	390	153	0.275	223	0.06
GU-T8-N11	140	8	1900	390	153	0.275	446	0.11
GU-T8-N17	140	8	1900	390	153	0.275	668	0.17
GU-T8-N23	140	8	1900	390	153	0.275	891	0.23
GU-T5-N11	140	5	1900	386	153	0.160	378	0.11
GU-T6-N11	140	6	1900	391	153	0.196	400	0.11
GU-T10-N11	140	10	1900	392	153	0.361	489	0.11

According to the results of the preliminary finite element analysis, the benchmark

parameters were chosen as outer diameter D=140 mm, steel tube thickness t=8 mm, length L_s=1900, and axial compression ratio n=0.11. The axial compression ratio equaled to N_0/N_u, where N_0 was the applied axial force, and N_u was the bearing capacity of the specimen corresponding to the yield of the steel tube (Han, 2004).

Table 2-2 Material properties of steel tube

Steel type	Thickness t (mm)	f_y (MPa)	f_u (MPa)	E_s (MPa)	v
Steel tube	5	386	590	2.01×10P5	0.29
Steel tube	6	391	600	2.02×10P5	0.29
Steel tube	8	390	605	2.01×10P5	0.30
Steel tube	10	392	615	2.03×10P5	0.31

(1) Material properties of steel tube

The steel tube was made of Q345 steel. Three standard tensile specimens were made of steel tube with thickness of 5mm, 6mm, 8mm and 10mm respectively. The specimens were made according to GB/T228.1 (2010). The physical and mechanical properties of steel specimens, such as yield strength f_y, ultimate strength f_u, modulus of elasticity E_s and Poisson's ratio v, are shown in Table 2-2. Specimen loading progress and the stress-strain curves of the specimen under tension are shown in Fig. 2-1.

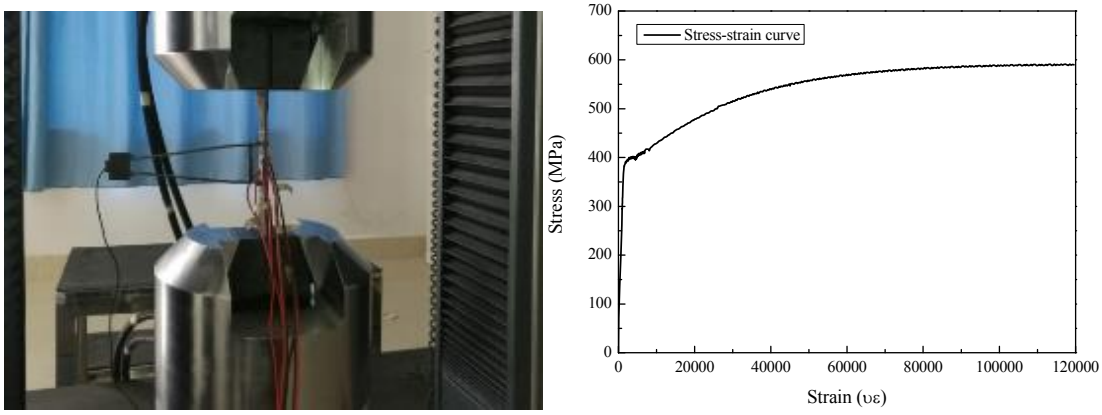

Fig. 2-1 Loading process of steel tube tensile specimen and tensile stress-strain curve

(2) Material properties of UHPC

1) Mix proportion of UHPC

The following components were mainly adopted to compose UHPC:

(a) Cement: Fujian "Stone Refining Brand" P.O 42.5 ordinary concrete Portland cement;

(b) Silica fume: The silica fume was produced in Xining Ferroalloy Plant. Its SiO_2 content was more than or equal to 90%, its specific surface area was 18.92 m^2/g, and its density was 2.0 g/cm^3.

(c) Quartz sand: The quartz sand was produced by Shanghai Jinyuan Quartz Sand Co., Ltd. and had five particle sizes: 0.08-0.12 mm, 0.12-0.24 mm, 0.24-0.41 mm, 0.41-0.83 mm and 0.83-1.65 mm, respectively.

(d) Superplasticizer: CX-8 polycarboxylate superplasticizer selected in the experiment was provided for Fuzhou Pioneer Engineering Materials Co., Ltd.

(e) Water: The water used in the experiment was tap water in Fuzhou area.

Table 2-3 shows the mix proportion of UHPC in this paper.

Table 2-3 Material composition of UHPC (kg/m^3)

Cement	Silica fume	Quartz sand (mm)					Superplasticizer	Water
		0.08-0.12	0.12-0.24	0.24-0.41	0.41-0.83	0.83-1.65		
859.5	257.8	74.1	171.7	170.7	260.7	328.5	21.5	178.8

2) Compressive strength

According to the national standard "Reactive powder concrete" (GB/T 31387-2015) compressive strength test method, three UHPC cubes (100×100×100 mm) and six UHPC prisms (100×100×300 mm) were prepared and steam cured for three days at 90℃ for 28-day compressive strength test. The results showed that the UHPC cube had a compressive strength of 153 MPa, the UHPC prism had a compressive strength of 135 MPa and an elastic modulus of 43000 MPa. Fig. 2-2 is the loading diagram of UHPC specimens.

(a) UHPC cube specimen (b) UHPC prism specimen

Fig. 2-2 Loading diagram of UHPC specimens

2.1.2 Making of UCFT columns

Seamless steel tube was used for the circular high strength steel tube in this paper. And the specimens were processed and assembled in the steel factory. Firstly, the hollow steel tube was machined by mechanical cutting according to the required length to ensure the smooth cross section at both ends. Then, two square steel plates with 300 mm side length and 20 mm thickness were machined as cover plates for each specimen. Four bolt holes with 24 mm diameter were opened on the four corners of each cover plate. One hole with 100 mm diameter in the middle of one cover as a casting hole and four air holes were opened. In order to prevent the ends of the specimen from being damaged during loading, eight stiffeners with thickness of 10 mm and height of 100 mm were welded at the top and bottom of each steel tube. The weld was designed in accordance with the national standard "Standard for design of steel structures" (GB50017-2014). The detailed dimension of the reference member is shown in Fig. 2-3.

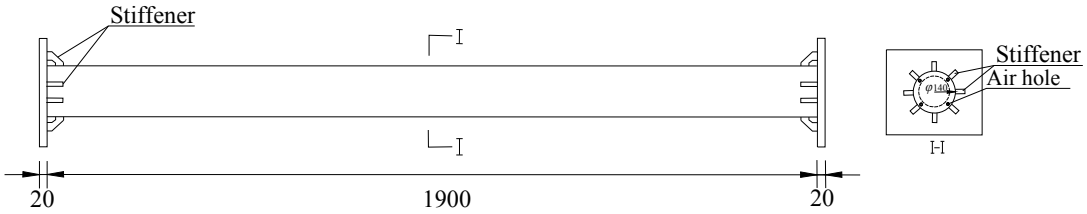

Fig. 2-3 Design of UCFST columns (mm)

Different curing conditions will affect the strength of UHPC. Steam curing accelerates the hydration and hardening speed of UHPC, and then improves the early strength of UHPC, which changes relatively little in the later period. The strength of UHPC under standard curing will increase with the accumulation of time, and the change is relatively large, which is the same as other scholars' conclusions (Guo, 2017). Therefore, 90 ℃ steam curing was adopted to ensure that the strength of UHPC did not change too much with time.

The mixing of UHPC and the maintenance of UCFST columns were carried out in the laboratory of Fuzhou University. The mixed UHPC was slowly poured into the steel tube, and the vibration of the steel tube was carried out by using the plane vibration bar. After three days of stationary laying, the UCFST columns were steam cured at 90 C with the UHPC test specimens. After three days of steam curing, the UHPC specimens and UCFST columns were moved into the room for room temperature curing to 28 days. The UCFST columns are shown in Fig. 2-4.

Fig. 2-4 Picture of UCFST columns

2.2 Test loading scheme

2.2.1 Loading method

The loading device for the cyclic experiment is schematically shown in Fig. 2-5, in which a concentrated load was applied and kept constant at the midspan of the specimen with two hinged supports. The loading device consisted of jack, front fixture support, pin support, posterior fixture support, lateral support and rigid fixture.

In order to satisfy the normal use under large axial force, two pin supports which can withstand 200t force were designed, and were respectively connected with front fixture support and posterior fixture support with high-strength bolts to form one support which could move horizontally and rotate unilaterally, and the other could only rotate unilaterally. In order to prevent the MTS actuator loading head from turning out of plane, two lateral supports were designed. At the same time, considering that the lateral support would affect the test results, the spring device was installed on the lateral support, and the stiffness of the control spring was guaranteed to restrain the MTS actuator loading head, without too much influence on the test results. Furthermore, considering the connection between the MTS actuator loading head and the specimen, a rigid fixture which could withstand 100t force was designed to ensure that the fixture would not deform during loading.

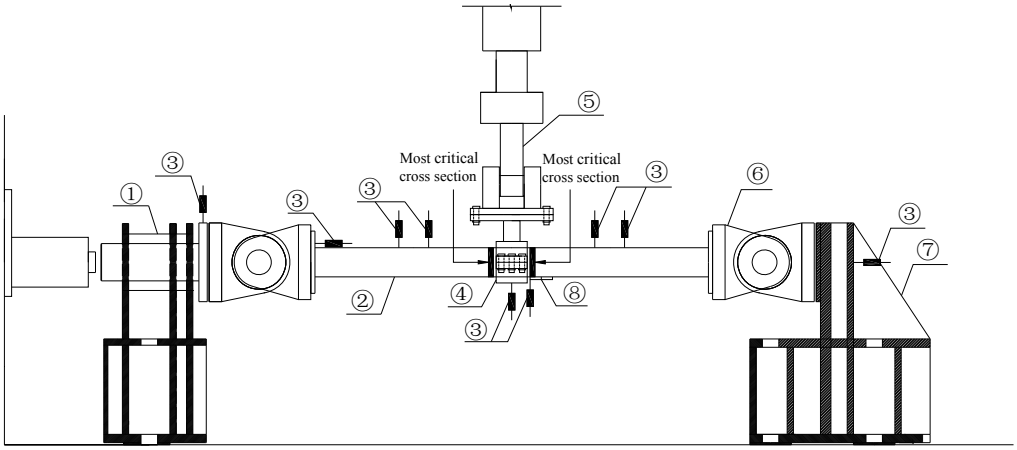

Fig. 2-5 Experimental setup: (① Front fixture support; ② Specimen; ③ Displacement meter; ④ Rigid fixture; ⑤ MTS actuator; ⑥ Pin support; ⑦ Posterior fixture support; ⑧ Curvimeter).

Before loading, the front and posterior fixture supports were fixed in the groove through ground anchor, and then the specimen was connected with the two pin supports with high-strength bolts. Finally, the MTS actuator loading head and the specimen were connected with the rigid fixture. At the same time, the lateral supports were installed to ensure that there was a little distance between the lateral supports and the MTS actuator loading head. During the test loading, the axial force was applied by a 200t hydraulic jack placed horizontally. And a special oil pump device was manually controlled to maintain the stability of the axial force. The specific layout of the loading device is shown in Fig. 2-6.

Fig. 2-6 Experimental diagram of UCFST column

2.2.2 Test loading system

Displacement control mode provided by "Specification for seismic test of buildings " (JGJ/T 101-2015) was adopted as the test loading system. Before yielding, each stage displacement was loaded twice. After yielding, the loading displacement was multiplied by the yield displacement, and each stage displacement was loaded three

times. The loading mode is shown in Fig. 2-7. And the specific loading scheme was consistent with that in literature (Ghafari et al., 2015), as shown in the following:

(1) Applying horizontal load. Before loading formally, the horizontal load was applied to $0.5N_0$ (N_0 was the design value of the axial force when loading formally), then the uniform unloading was carried to zero to eliminate the non-uniformity within the specimen, and the graded loading was applied to the design load N_0 and remains constant.

(2) Applying vertical displacement. The load was carried out in the form of displacement control. Before yielding, the specimen was subjected to graded loading with a multiple of 1 mm, and each stage displacement cycle was twice. After yielding, the specimen was subjected to loading with the multiple of the yield displacement corresponding to the yield of the specimens as the control displacement, i.e. $1\delta_y$, $1.5\delta_y$, $2\delta_y$, $2.5\delta_y$, $3\delta_y$,... Each displacement cycle lasted three times until the specimen was destroyed. The criteria for judging the failure of members were: (1) the load under a certain displacement decreased to 85% of the maximum load; (2) the steel tube at both sides of the fixture were cracked.

(3) End of loading. When the vertical load of the UCFST specimen decreased to about 85% of the peak load or the specimen was unsuitable for further loading, the test was completed.

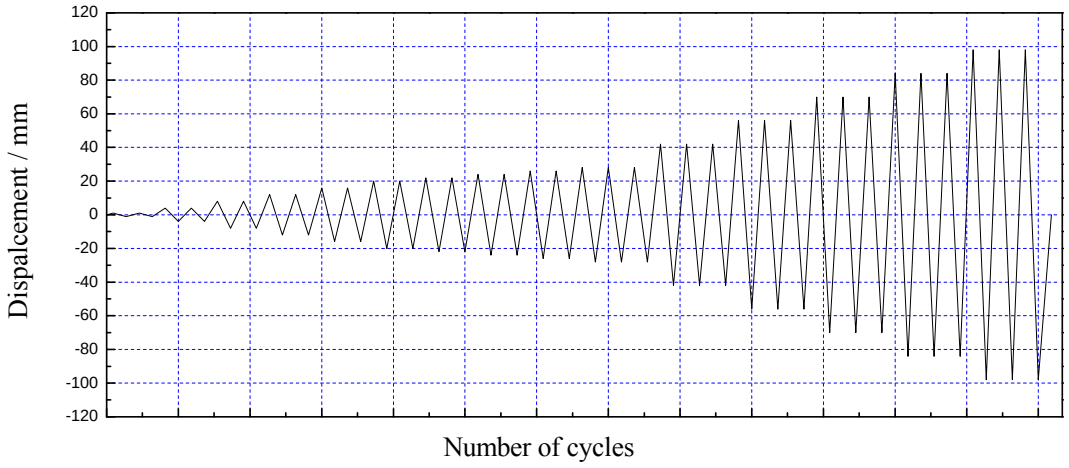

Fig. 2-7 Displacement control mode

2.2.3 Measurement

In the process of loading, the strain and displacement at the key position of the specimen need to be measured to analyze the stress of the specimen in the process of loading. During the loading process, the main observation was whether the steel pipe on both sides of the rigid fixture buckles or not, and whether the end of the steel pipe buckled.

(1) Displacement measurement

The displacement measurement can be divided into the measurement of the specimen deformation and the displacement of the test device. The displacements at the quarter points of the two pin supports centers and the specimen ends were measured by the No. 3, No. 7 and No. 4, No. 6 displacement meters arranged vertically, respectively; the mid-span deflection was measured simultaneously by the MTS actuator loading system and the No. 9 displacement meter placed at the mid-span; the axial displacement of the specimen was measured by the No. 2 displacement meter horizontally placed at the end of the specimen. The vertical displacement of the pin supports was measured by the No. 1 vertical displacement meter, and the corresponding No.8 displacement meter was arranged on the posterior fixture support to measure whether the displacement of the posterior fixture support would occur. The displacement meter layout is shown in Fig. 2-8.

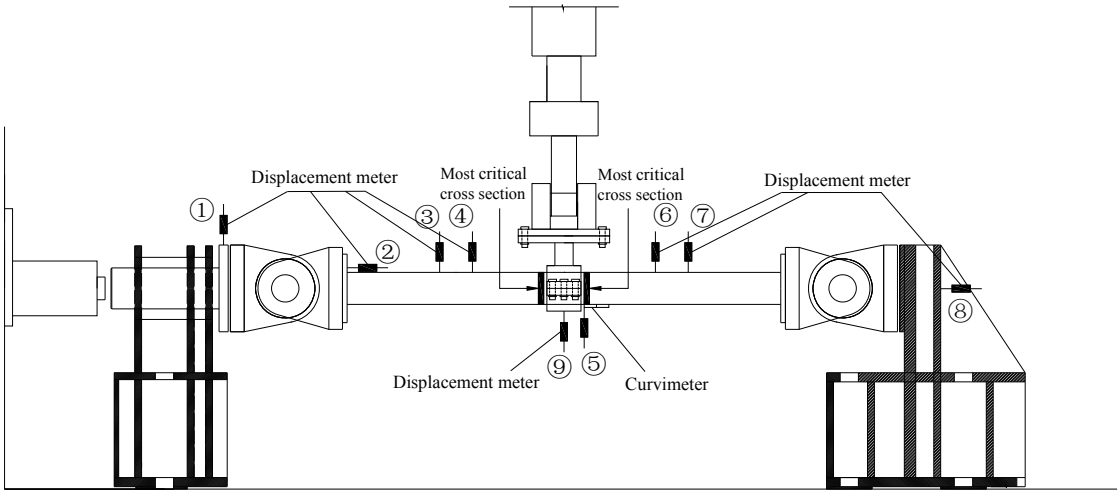

Fig. 2-8 Displacement meter layout

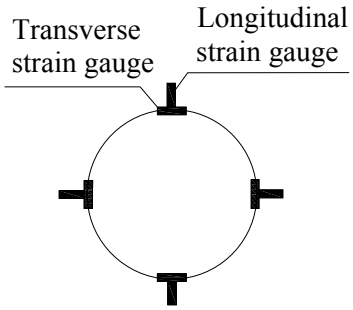

Fig. 2-9 Layout of the strain gauges at the most critical cross section

(2) Strain measurement

The most critical cross section of the specimen was located on both sides of the rigid fixture as shown in Fig. 2-8. Therefore, the longitudinal and transverse strains of the steel tube at both sides of the rigid fixture were measured by the bidirectional strain gauges arranged across the cross-section at both sides of the rigid fixture, so as to judge the initial yield point of the outer edge of the steel tube and the beginning of the specimen hoop. The strain gauge layout diagram of the specimen is shown in Fig. 2-9

(3) Curvature measurement

Two methods were used to measure the curvature of the most critical cross section of the UCFST specimens in the test, as follows:

(a) Curvature meter method

The schematic diagram of the curvature meter device is shown in Fig. 2-10 and the layout is shown in Fig. 2-8 above. During the test, the curvature meter was fixed with rubber belt at the section to be tested, and the displacement obtained by the curvature meter test method can be replaced by the following Eq. (2-1):

$$y = c_1 x^2 + c_2 x + c_3 \tag{2-1}$$

The above formula satisfies the boundary conditions:

$$\begin{Bmatrix} c_3 = 0 \\ c_1 a^2 + c_2 a = 0 \\ c_1 b^2 + c_2 b = f \end{Bmatrix} \tag{2-2}$$

The simultaneous Eq. (2-1) and Eq. (2-2) can be obtained:

$$\begin{cases} c_1 = \dfrac{f}{b(b-a)} \\ c_2 = \dfrac{af}{b(b-a)} \end{cases} \tag{2-3}$$

For the second derivative of y, the formula for calculating curvature φ is obtained.

$$\phi = \frac{2f}{b(b-a)} \tag{2-4}$$

In this test, the parameters a=100mm, b=200mm and f is the deformation value measured by C-point displacement meter.

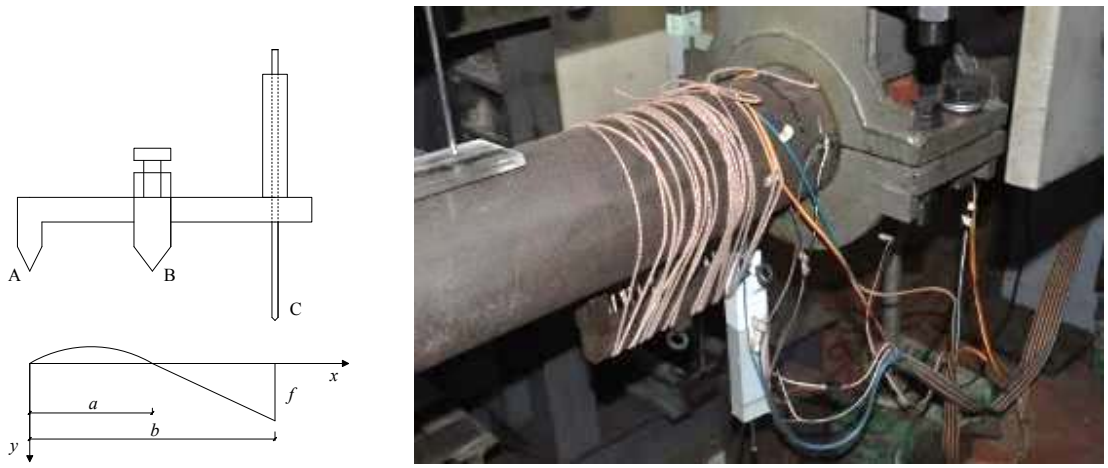

Fig. 2-10 Schematic diagram of curvature meter device

(b) Half-wave sin method

Assuming that the deformation curve of the specimen is consistent with the half-wave sine curve, the deflection curve equation of the specimen is as follows:

$$y = \mu_m \sin\left(\frac{\pi}{L}x + \frac{\pi}{2}\right) \tag{2-5}$$

Where, μ_m is the maximum deflection of the specimen under various loads.

Then, the curvature of the specimen can be calculated according to the following formula:

$$\phi(x) = \left|y''\right| = \left|\mu_m \left(\frac{\pi}{L}\right)^2 \sin\left(\frac{\pi}{L}x + \frac{\pi}{2}\right)\right| \tag{2-6}$$

Thus, the maximum curvature of the mid-span section is:

$$\phi(o) = \mu_m \left(\frac{\pi}{L}\right)^2 \tag{2-7}$$

2.3 Analysis of quasi-static test results

2.3.1 Experimental phenomena

(1) Elastic stage

The increment of 1 mm was used to load step by step from the zero point of displacement. With the increase of displacement, there was no phenomenon on the surface of the specimens, but when loaded to 5-10 mm, there was abnormal sound inside the steel tube, which would be the sound produced by the staggering of the steel tube and the core UHPC. When the load-displacement curve begun to appear the bending phase, that was, the strain of the outer side of the steel tube reached 2000, then the specimen can be judged to enter the elastic-plastic stage.

(2) Elastic-plastic stage

With the increase of vertical displacement, the specimen yielded, and there was no bulging phenomenon in the early stage of the specimen yield. Only when the vertical displacement was large enough, the specimen would buckle. The sound of UHPC breaking in the steel tube could be heard in the late stage of the specimen yield. By analyzing the loading process of the eight specimens, it was found that when the axial compression ratio was less than or equal to 0.2, the buckling phenomenon occurred in the yield stage. When the buckling happens, the steel tube's compression side was about 30 mm away from the edge of the rigid fixture, and there was no obvious change on the tension side. When the reverse loading occurred, the compression side became the tension side and the original tension side became about 30 mm away from the edge of the rigid fixture. While in the later stage of yield, the buckling of compression side of specimens gradually developed toward circular direction, and the buckling deformation became more and more obvious. When the specimens were loaded backward, the original buckling of compression side could not be flattened, and the bearing capacity of specimens decreased gradually. However, when the axial compression ratio was 0.17 and 0.23, no drumming occurred in the yield stage as well as when the bearing capacity of the two specimens decreased. When the specimen

was loaded to 1 δ_y, it was found that the end of MTS actuator rotates slightly outward, which resulted in inconsistency of tensile and compressive bearing capacity.

(3) Damage stage

(a)GU-T8-L19-N03 (b)GU-T8-L19-N06

(c)GU-T8-L19-N11 (d)GU-T8-L19-N17

(e)GU-T8-L19-N23 (f)GU-T5-L19-N11

(g)GU-T6-L19-N11 (h)GU-T10-L19-N11

Fig. 2-11 Integral bending failure diagram of UCFST columns

With the increase of the loading displacement, the bearing capacity of the specimens decreased gradually. When the bearing capacity decreased to 85% of the maximum bearing capacity. It can be judged that the specimen cannot continue bearing the load. When the specimens GU-T8-N17 and GU-T8-N23 were damaged, there were large residual deformation and bending failure. While when the specimens GU-T8-N11, GU-T5-N11, GU-T6-T11 and GU-T10-N11 were damaged, the drum was very obvious, and the specimens had large residual deformation, and ultimately the bending failure occurs. As for GU-T8-N03 and GU-T8-N06, they had very large residual deformation at the end of loading. Before the bearing capacity of the specimens drops to 85% of the maximum bearing capacity, the steel tube was suddenly pulled apart, and the bearing capacity dropped to 0, which made it

impossible to bear the load. The buckling deformation and overall bending failure of the specimens were shown in Fig. 2-11 and Fig. 2-12.

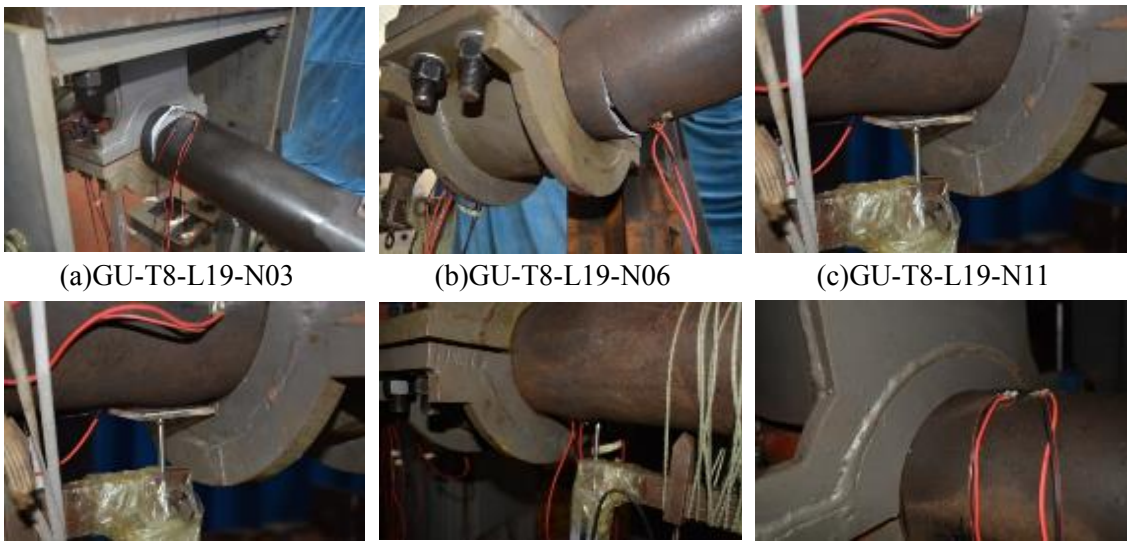

(a)GU-T8-L19-N03 (b)GU-T8-L19-N06 (c)GU-T8-L19-N11

(d)GU-T5-L19-N11 (e)GU-T6-L19-N11 (f)GU-T10-L19-N11

Fig. 2-12 Local drum diagram of UCFST columns

2.3.2 Strain analysis

From Section 2.3.1 of this chapter, we can see that the strain development at the most critical cross section (i.e. longitudinal and transverse strain gauges were attached to both sides of the rigid fixture) was measured before loading. The load-strain hysteresis curves of the most critical cross section of typical specimens are given in Fig. 2-13, and the longitudinal strain-vertical displacement curves of the most critical cross section of typical specimens are given in Fig. 2-14.

Fig. 2-13 shows the typical relationship between load-strain (including the longitudinal strain and transverse strain) hysteresis curves of the steel tube of typical UCFST members. Clearly, the load-strain hysteresis curves were approximately linear during the initial loading, indicating that the steel tube was in the elastic stage. As the vertical displacement increased, the steel entered the yield stage, resulting in a sudden increase in longitudinal strain and, consequently, an increase in the area of the hysteretic loop that could exceed the measurement range of the strain gauge. In general, the magnitude of the transverse strain was very small at the initial stage of

loading. This is because there was no interaction between the steel tube and core UHPC as the Poisson's ratio of the steel tube was larger than that of core UHPC. The increase of loading displacement resulted in an increase of the transverse strain of the steel tube. When the steel tube yielded. However, the specimen showed a large deformation in the elastic-plastic stage, and the Poisson's ratio of the core UHPC at the midspan was higher than that of the steel tube. As a consequence, the core UHPC could exert radial and circumferential force on the steel tube, resulting in a large transverse strain of the steel tube.

Fig. 2-14 shows the longitudinal strain at the most critical cross section of the specimens corresponding to each vertical loading displacement. It can be seen in the figure that at the initial stage of loading, when the specimen was in the elastic stage, the curve was basically straight line; and when the loading displacement increased and the specimen entered the elastic-plastic stage, the longitudinal strain suddenly increased and the slope of the curve increased at first. The figure shows that as the increase of the displacement, the slope of the curve decreased gradually which was due to the increasing progressive residual deformation.

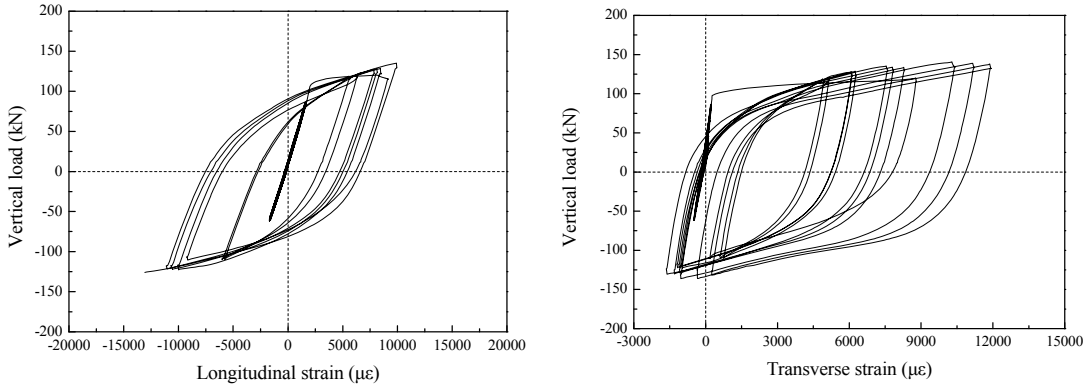

(a) GU-T8-L19-N03

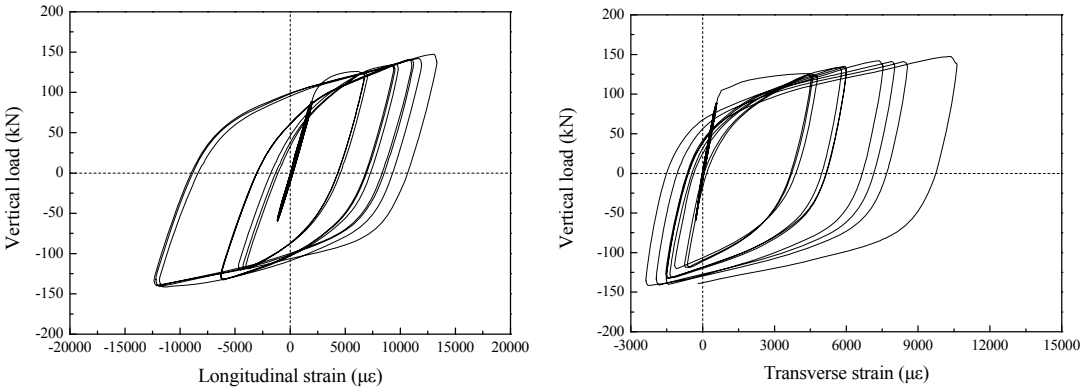

(b) GU-T8-L19-N06

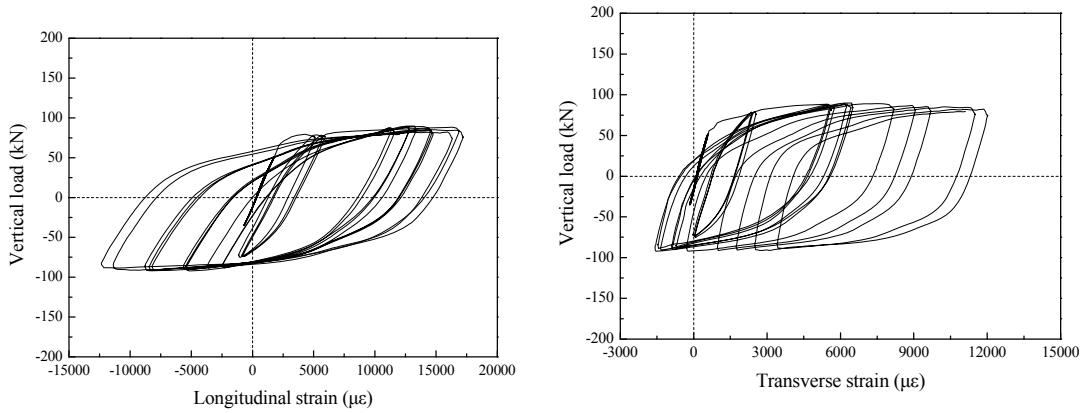

(c) GU-T5-L19-N11

Fig. 2-13 Typical vertical load-strain hysteresis curve

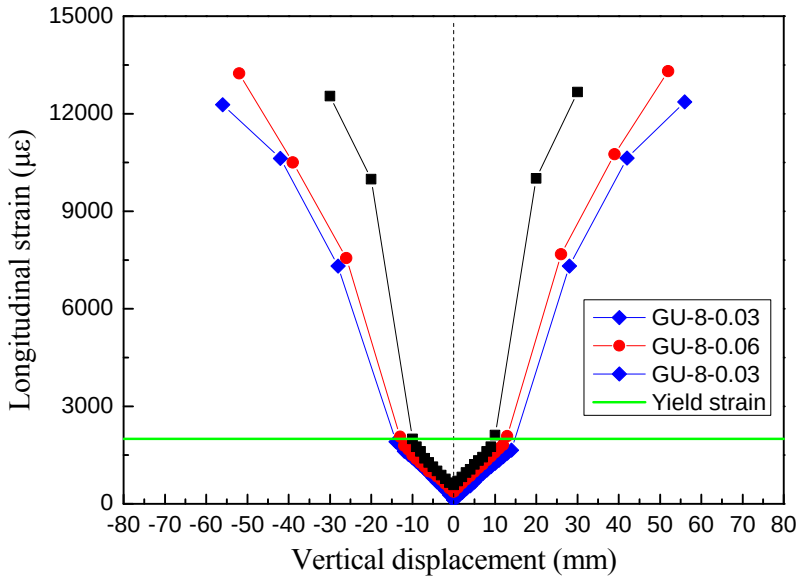

Fig. 2-14 Typical Longitudinal strain-vertical displacement curves

2.3.3 Load-displacement hysteresis curve

Fig. 2-15 shows the load-displacement hysteresis curves of all the UCFST columns. It can be seen that the load-displacement hysteresis curves were full and there was no pinch phenomenon. It shows that the structure composed of UHPC and high strength steel had good energy dissipation capacity. In the elastic stage, the hysteresis curve passed through the origin, and the elastic bending rigidity of the specimen remained constant without plastic deformation. As the vertical displacement increased, the hysteresis curve was no longer linear and residual deformation occurred after unloading, forming a hysteretic loop which was symmetric about the origin. The displacement increased at a rate different from that of the load, indicating that the specimen was in the elastic-plastic stage. Once the steel tube begun to yield and the vertical load reached the peak load, the bearing capacity of the specimen corresponding to each loading displacement level was decreased, the loading rigidity was reduced slowly, the unloading rigidity remained unchanged, and the residual deformation increased after unloading. The area enclosed by the loading and unloading curves increased, and the hysteretic loop was spindle shaped with good plastic energy dissipation and deformation ability. As the vertical load decreased below 85% of the maximum load, the load was unloaded to zero, resulting in large residual deformation and bending failure. Importantly, the maximum vertical load at each loading level was observed at the end of unloading rather than at the maximum displacement due to the Bauschinger's effect of the steel, which became more pronounced with the increase of axial compression ratio.

It can be seen that the skeleton line of the load-displacement curve was basically linear in the later stage when the axial compression ratio was small, and there was no obvious decline. When the axial compression ratio was large, the skeleton curve of the hysteretic curve had obvious decline section. With the increase of steel ratio, the larger and fuller the area enclosed by hysteretic curve was, and the flatter the skeleton curve was in the later stage, while other parameters remained unchanged. It can be seen from the above that the axial compression ratio and steel ratio had great

influence on the load-displacement hysteretic curve of UCFST columns.

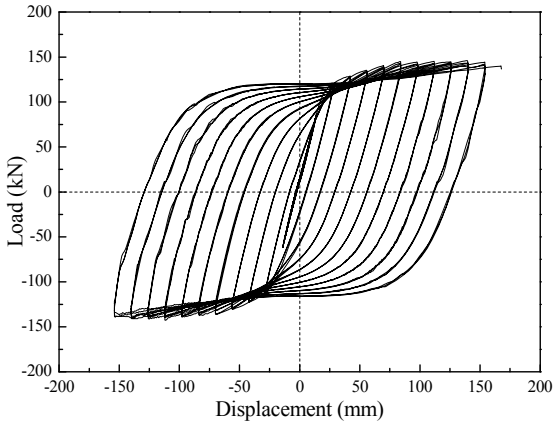

(a)GU-T8-L19-N03

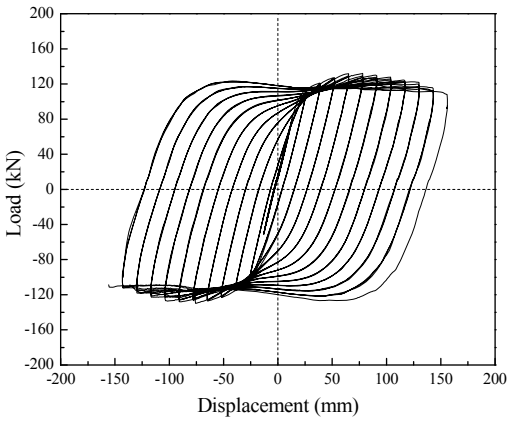

(b)GU-T8-L19-N06

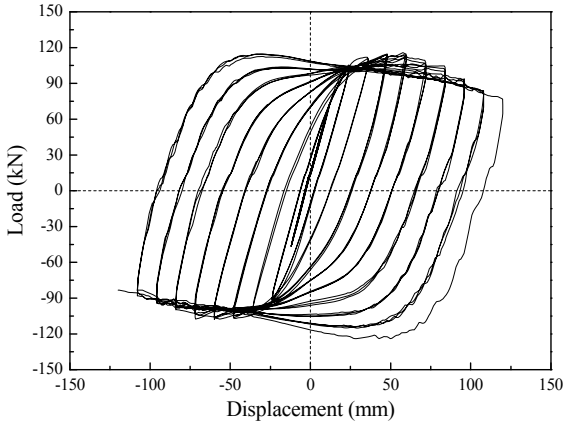

(c)GU-T8-L19-N11

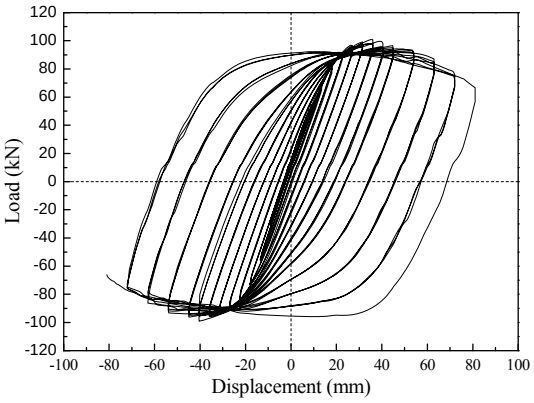

(d)GU-T8-L19-N17

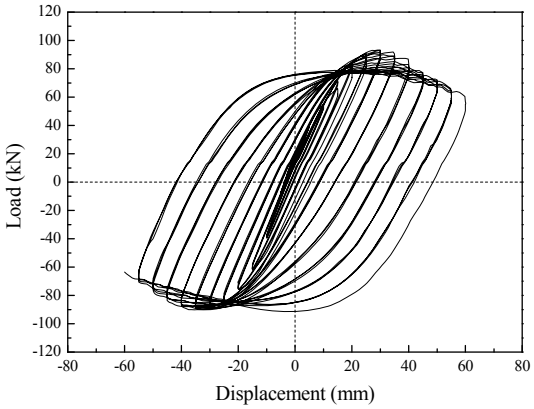

(e)GU-T8-L19-N23

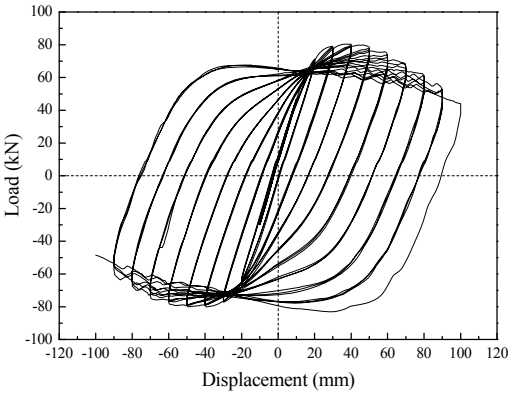

(f)GU-T5-L19-N11

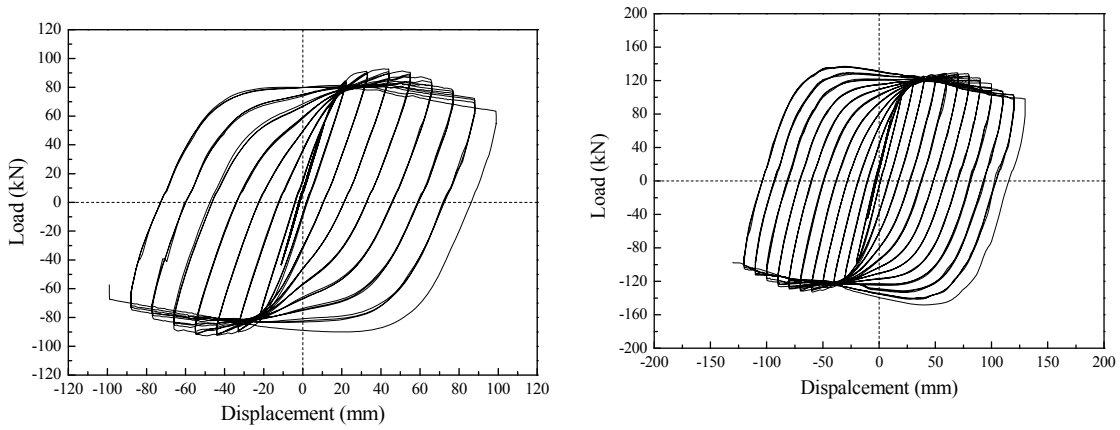

(g)GU-T6-L19-N11 (h)GU-T10-L19-N11

Fig. 2-15 Load-displacement hysteretic curve of UCFST columns

Because the specimens were single-leg circular columns in the test, although the lateral support was designed, the load head of MTS actuator would rotate outward to a certain extent with the increase of displacement, especially when applied pressure, which resulted in the difference of the tensile and compressive bearing capacity of the columns. At the same time, because the horizontal load of the test device was provided by the hydraulic jack, manual operation made the oil pressure not completely constant. Especially when the displacement was large, the oil pressure was difficult to maintain stability, making the curve not smooth and symmetrical about the origin.

2.3.4 Moment-curvature hysteresis curve

Hysteretic performance reflects the energy dissipation capacity, ductility and stiffness degradation of specimens under low cyclic loading, which is mainly reflected by hysteretic curves. Hysteresis curves includes load-displacement curves and bending moment-curvature curves. The measured physical quantities in the test process were the load P and displacement Δ of the specimen middle span. While, the bending moment and curvature in the cross section should be further converted. Among them, the calculation formula of bending moment M was as follows, where L was the calculated length, which equaled to the sum of the specimen length and the two distances from the end plate at both ends of the component to the front and rear

supports seat hinge center, N was the applied axial force.

$$M = 1/4P \cdot L + N \cdot \Delta \tag{2-8}$$

The experimental deflection curves and half-wave sinusoidal deflection curves at one quarter of the measured points are shown in Fig. 2-16. The black dotted line in the figure represented half-wave sinusoidal curve, and the black solid line represented the measured deflection curve of the specimen. From the figure, it can be seen that the deflection curve of the specimen basically coincided with the half-wave sinusoidal curve. Because of the drumming of the specimen, the curvature measured by the curvature meter was confused in the later stage of loading and cannot be used.

Comparing the M-φ hysteretic curves obtained by curvature meter method and half-wave sine method, it was found that the M-φ hysteretic curves calculated by curvature meter method were inaccurate, the data of initial loading curves were more accurate, and the data of later loading curves were confused, which may be due to the local buckling of the columns at the curvature meter measurement site, resulting in inaccurate data. The M-φ hysteretic curves obtained by half-wave sinusoidal method can ensure that the data accuracy of the whole loading process meted the requirements. Therefore, half-wave sinusoidal method was used to calculate M-φ hysteretic curves in this paper.

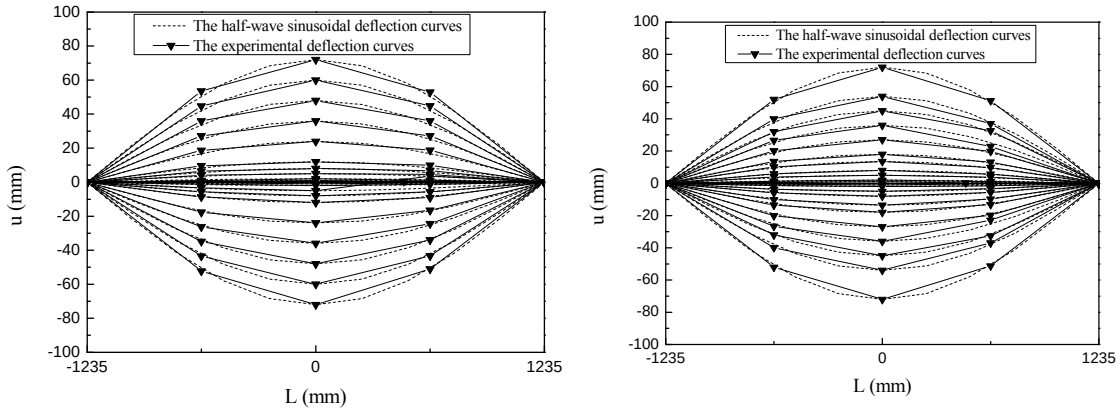

(a)GU-T8-N11 (b)GU-T8-N17

Fig. 2-16 Deflection curves of UCFST columns

2.3.5 Moment-curvature hysteresis curve skeleton curve

According to Fan and Zhuo (2001), geometric drawing method, equal energy method and general yield moment method can be used to determine the yield curvature. In this paper, the general yield moment method was used to calculate the yield curvature. For the ultimate curvature, the curvature corresponding to the ultimate displacement when the bearing capacity was reduced to 85% was chosen as the ultimate curvature in this paper. The specific definition is showed in Fig. 2-17 below. Because the skeleton curve of this test was not completely symmetrical about the origin, and the positive and negative ultimate bending moments were different, the positive and negative curvature ductility coefficients calculated by the general yield moment method were not equal. In order to compare the curvature ductility of each specimen conveniently, the curvature ductility coefficients of this paper were the average value of positive and negative curvature ductility coefficients. The yield moment was the moment corresponding to the yield curvature determined by the geometric drawing method at point Y in Fig. 2-17. And the ultimate moment was the moment corresponding to the vertical load in the middle span reduced to 85% of the maximum bearing capacity at point U in Fig. 2-17.

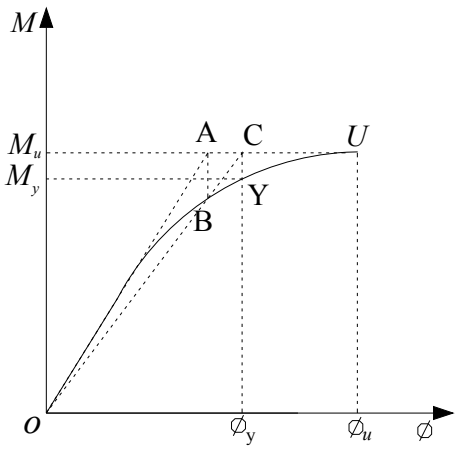

Fig. 2-17 Determination of eigenvalues of moment-curvature skeleton curve

Fig. 2-18 (a) compares the effects of different axial compression ratios on moment-curvature skeleton curves. From Fig. 2-18, it can be seen that the skeleton

curves with different axial compression ratios coincided basically in the elastic stage. Combining with Table 2-5, it can be found that the yield moment increased firstly and then decreased with the increase of axial compression ratio. When the axial compression ratio increased from 0.03 to 0.23, the ultimate bending moment decreased from 104.4 kN·m to 89.59 kN·m, decreased by 14.2%. While curvature ductility coefficient changed from 3.71 to 1.63, decreased by 56.1%. The above data showed that with the increase of the axial compression ratio, the yield moment increased firstly and then decreased, while the ultimate bending moment and curvature ductility coefficient decreased gradually, which indicated that the axial compression ratio had a greater impact on the seismic behavior of UCFST columns.

Table 2-4 Eigenvalues of moment-curvature skeleton curve

Specimen number	M_{yu} (kN·m)	Φ_{yu} (1/m)	M_u (kN·m)	Φ_u (1/m)	u_Φ
GU-T8-L19-N03	77.88	0.070	104.40	0.26	3.71
GU-T8-L19-N06	78.13	0.066	104.01	0.24	3.64
GU-T8-L19-N11	78.38	0.056	99.09	0.17	3.04
GU-T8-L19-N17	80.42	0.050	93.75	0.1	2.00
GU-T8-L19-N23	79.88	0.049	89.59	0.08	1.63
GU-T5-L19-N11	56.12	0.050	67.36	0.12	2.4
GU-T6-L19-N11	64.34	0.050	78.66	0.13	2.6
GU-T10-L19-N11	91.80	0.064	120.65	0.20	3.12

Note: M_{yu}、Φ_{yu} were the yield moment and its corresponding curvature; M_u、Φ_u were the ultimate moment and its corresponding curvature; u_Φ was curvature ductility coefficient.

Fig. 2-18 (b) compares the effects of different steel ratio on moment-curvature skeleton curves. With the increase of steel ratio, the stiffness and ultimate bending moment of skeleton curve in elastic stage increased gradually. Combined with Table 2-5, it can be seen that the yield moment increased from 56.12 kN·m to 64.34 kN·m, 78.38 kN·m and 91.80 kN·m with the steel ratio changing from 0.160 to 0.196, 0.275 and 0.361, respectively, increasing by 14.6%, 39.6% and 63.6%. And the ultimate bending moment increased from 67.36 kN·m to 78.66 kN·m, 99.09 kN·m and 120.65 kN·m, respectively, increasing by 16.8%, 47.1% and 76.5%. The curvature ductility coefficient changed from 2.4 to 2.6, 3.04 and 3.12, which increased by 8.3%, 26.6%

and 30.0% respectively. The above data showed that with the increase of steel ratio, the yield moment and ultimate moment increased greatly, and the curvature ductility coefficient increased gradually. When the thickness of steel tube was 5 mm, 6 mm and the axial compression ratio was 0.11, the curvature ductility coefficient was less than 3 and the ductility of specimens was poor, which indicated that the steel tube had insufficient binding force on UHPC. When the steel ratio was 0.275, 0.361 and the axial compression ratio was 0.11, the curvature ductility coefficient was greater than 3, which indicated that the specimens had good seismic performance.

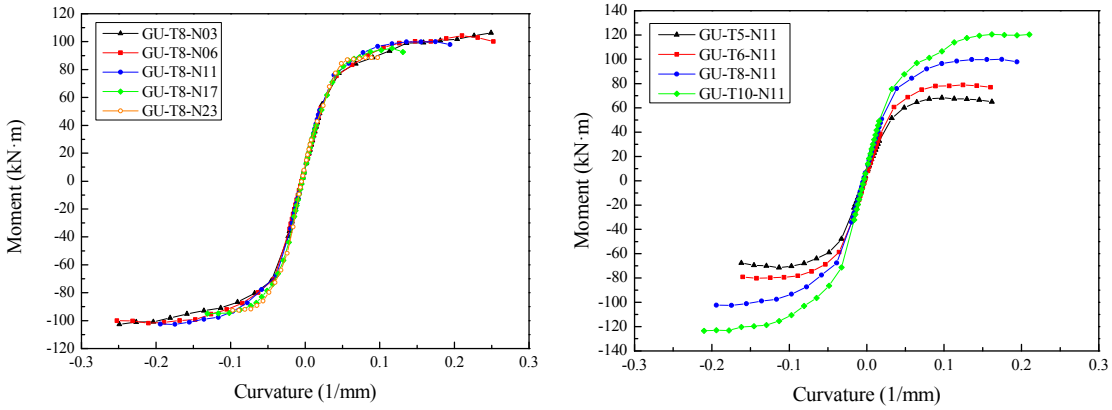

(a) Axial compression ratio and (b) Steel ratio.

Fig. 2-18 Skeleton curves of moment-curvature hysteresis curves

2.3.6 Strength and stiffness degradation

(1) Strength degradation

The degradation of strength referred to the continuous decrease in the bending strength at the midspan when subjected to cyclic loading, which can be described by the reduction coefficient λ (You and Han, 2005). And it can be calculated as follows:

$$\lambda = \frac{M_i^n}{M_{max}} \tag{2-10}$$

where M_i^n was the bending moment at the midspan corresponding to the last cycle of each load level, and M_{max} was the maximum midspan bending moment at the midspan.

Fig. 2-19 shows the curve of the reduction coefficients of the specimens calculated

by Eq. (2-10) changing with curvature. The values of the reduction coefficients when the specimens reached the limit curvature are listed in Table 2-5. From Table 2-5, it can be seen that the bending moment hardly decreased during the whole loading process, and the bending moment reduction coefficients fluctuated slightly around 1.

Fig. 2-19 (a) compares the effects of different axial compression ratios on the moment reduction coefficient. In combination with Table 2-5, it can be found that when the axial compression ratio changed from 0.03 to 0.23, the reduction coefficient corresponding to the ultimate curvature increased, but the change was very small, all around 1. When the axial compression ratio was 0.17 and 0.23, the bending moment corresponding to the ultimate curvature was the maximum bending moment. Therefore, it can be concluded that the axial compression ratio had little effect on the moment reduction factor.

Fig. 2-19 (b) compares the effect of different steel ratio on the moment reduction coefficient. In combination with Table 2-5, it can be found that when the steel ratio changed from 0.160 to 0.196, 0.275 and 0.361, the reduction coefficient increased from 0.986 to 0.992, 0.995 and 0.998, with little change. It can be seen that with the increase of steel ratio, the reduction coefficient would increase slightly. Generally speaking, the strength of cross-section had not deteriorated.

Table 2-5 List of peak moment reduction coefficients corresponding to ultimate curvature

Specimen number	GU-T8-N03	GU-8-N06	GU-T8-N11	GU-T8-N17	GU-T8-N23	GU-T5-N11	GU-T6-N11	GU-T10-N11
λi	0.979	0.982	0.995	1	1	0.986	0.992	0.998

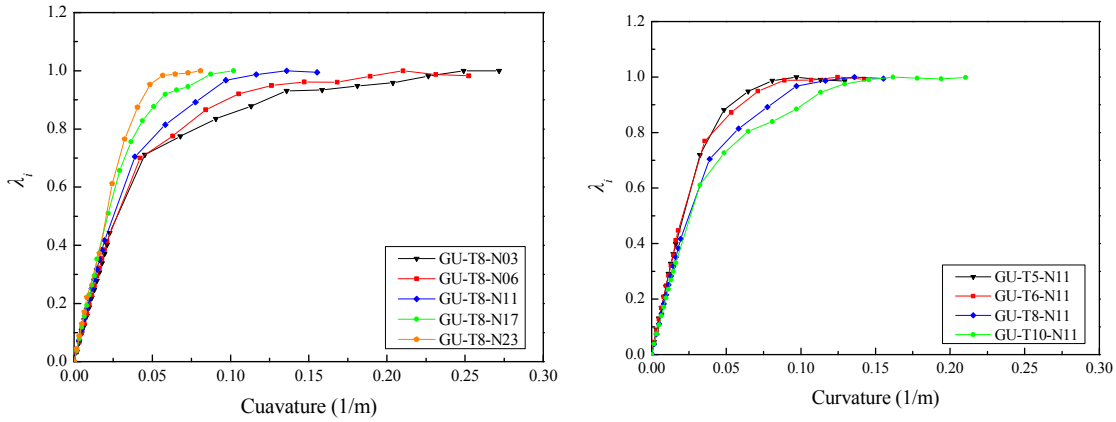

(a) Axial compression ratio (b) Steel ratio

Fig. 2-19 Changes in curvature ductility coefficient

(2) Stiffness degradation

With the increase of vertical displacement, the bending stiffness begun to decrease as the UCFST columns entered into plasticity, and stiffness degradation occurred. The bending stiffness can be expressed by the secant stiffness K_i (You and Han, 2005), shown as the slope of straight-line AB in Fig. 2-20.

$$K_i = \frac{|+M_i|+|-M_i|}{|+\varphi_i|+|-\varphi_i|} \tag{2-11}$$

where M_{i+} was the moment at the i^{th} peak point, and φ_i was the curvature at the i^{th} peak point at the same loading level.

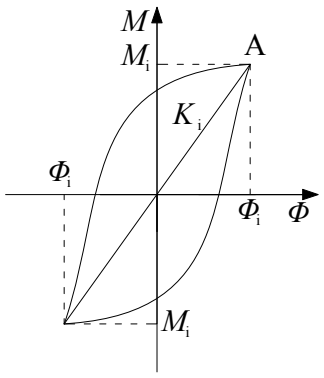

Fig. 2-20 Calculation diagram of the secant stiffness

Fig. 2-21 shows the bending stiffness curves calculated by Eq. (2-11) varying with curvature, in which K_i was the average secant stiffness corresponding to each level of

displacement. The initial secant stiffness, the final secant stiffness and the stiffness degradation rate are listed in Table 2-6. When the vertical displacement was small, the bending stiffness was basically unchanged. When the vertical displacement increased, the plastic deformation of the specimens begun, and the bending stiffness gradually degenerated. Until the later stage of loading, the bending stiffness gradually tended to be stable. The main reason for the degradation of bending rigidity was that the Bauschinger effect of steel tube under repeated loading was obvious, and the steel bending rigidity was decreasing. Moreover, under repeated loads, steel tube yielded and UHPC cracks occurred continuously, which reduced the bending rigidity of the specimens.

Fig. 2-21 (a) shows the bending stiffness curves varying with curvature under different axial compression ratios. It can be seen from the graph that the degradation trend of bending stiffness of each curve was similar. According to Table 2-6, as the axial compression ratio changing from 0.03 to 0.06, 0.11, 0.17 and 0.23, the initial bending stiffness changed from 2147 $kN \cdot m^2$ to 2185 $kN \cdot m^2$, 2212 $kN \cdot m^2$, 2274 $kN \cdot m^2$ and 2162 $kN \cdot m^2$; The final bending stiffness changed from 378 $kN \cdot m^2$ to 396 $kN \cdot m^2$ 522 $kN \cdot m^2$, 715 $kN \cdot m^2$, and 933 $kN \cdot m^2$. The stiffness degradation rate of the specimens changed from 82.39% to 81.88%, 76.40%, 68.56% and 56.85%, respectively, with 1.34%, 7.27%, 16.79% and 31.00%. The above indicated that axial compression ratio had a certain influence on initial bending stiffness of the specimens.

Fig. 2-21 (b) shows the curves of the bending stiffness varying with curvature under different steel ratio. It can be seen from the graph that the degradation trend of the bending stiffness was similar. With the increase of steel ratio, the bending stiffness also increased. According to Table 2-6, when the steel ratio changed from 0.160 to 0.196, 0.275 and 0.361, the initial bending stiffness increased from 1809 $kN \cdot m^2$ to 2049 $kN \cdot m^2$, 2212 $kN \cdot m^2$ and 2514 $kN \cdot m^2$. And the final bending stiffness increased from 410 $kN \cdot m^2$ to 487 $kN \cdot m^2$, 522 $kN \cdot m^2$ and 580 $kN \cdot m^2$. The degradation rate of the bending stiffness changed from 77.34% to 76.23%, 76.40%, 7.40% and 6.93%, which changed by 1.43%, 1.21% and 0.53% respectively. It shows that the initial and

final bending stiffness increased with the increase of steel ratio, but the stiffness degradation rate had little effect.

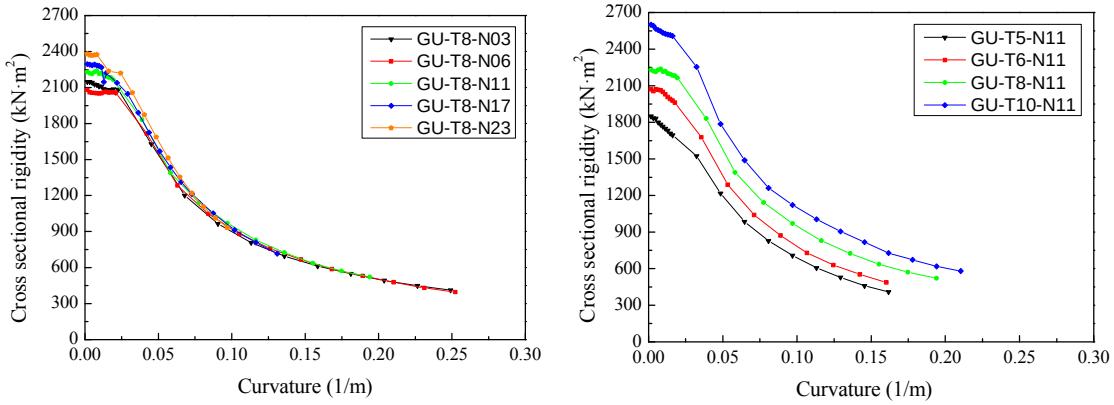

(a) Axial compression ratio (b) Steel ratio

Fig. 2-21 Cross sectional stiffness degradation curve

Table 2-6 Variation list of cross-sectional stiffness

Number	Initial stiffness (kN·mP2)	Final stiffness (kN·mP2)	Stiffness degradation (%)
GU-T8-N03	2147	378	82.39
GU-T8-N06	2185	396	81.88
GU-T8-N11	2212	522	76.40
GU-T8-N17	2274	715	68.56
GU-T8-N23	2162	933	56.85
GU-T5-N11	1809	410	77.34
GU-T6-N11	2049	487	76.23
GU-T10-N11	2514	580	76.93

2.3.7 Energy dissipation ability

The area of hysteretic loop formed by loading and unloading at each stage can be used to judge the energy dissipation of the specimen. It is an important index for evaluating the seismic performance of the specimen (Fan and Zhuo, 2001; Xie, 2005). According to the national standard "Specification for seismic test of buildings" (JGJ/T 101-2015), the energy dissipation ability of UCFST columns was described by the energy dissipation coefficient E and the equivalent viscous damping coefficient h_e, which could be calculated from the area of the last hysteretic loop at each loading level:

$$E = \frac{S_{(ABC+CDA)}}{S_{(OBE+ODF)}} \tag{2-12}$$

$$h_e = \frac{1}{2\pi} E \tag{2-13}$$

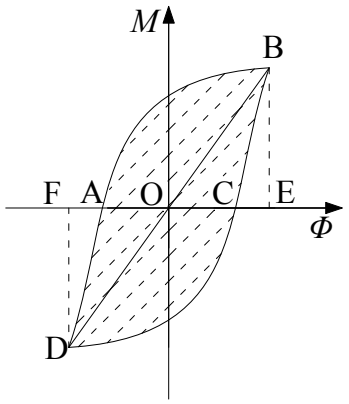

Fig. 2-22 A schematic for the calculation of energy dissipation coefficient

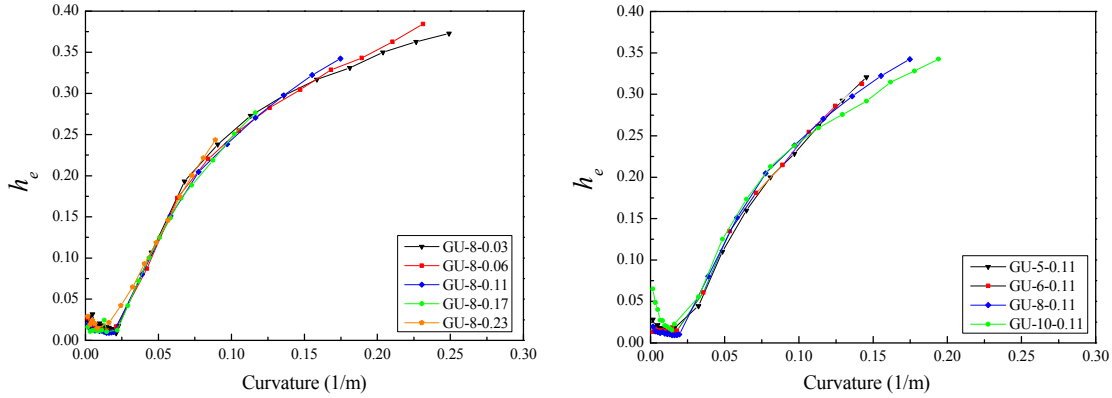

(a) Axial compression ratio (b) Steel ratio

Fig. 2-23 Equivalent viscous damping coefficient-curvature curve

Fig. 2-23 shows the equivalent viscous damping coefficient h_e as a function of curvature. It is clear that the equivalent viscous damping coefficient increased with the increase of curvature. As a result, the area of the hysteretic loop increased, indicating that the energy dissipation ability of UCFST columns was improved with the increase of curvature. Fig. 2-23 (a) shows that the five curves were basically coincident during the initial loading, but failure occurred in those specimens with a large axial compression ratio during the later loading period. Thus, increasing the axial compression ratio resulted in a decrease in the energy dissipation ability of

UCFST columns. Fig. 2-23 (b) shows that as the steel ratio increased, the energy dissipation coefficient of specimen increased, indicating an improvement of the energy dissipation ability.

2.4 Summary of Chapter 2

(1) The eight UCFST columns with an axial compression ratio of 0.03-0.11 and a steel ratio of 0.275-0.361 showed different failure modes. As the loading displacement at the midspan increased, buckling was observed at both sides of the rigid fixture in the yield stage in the six specimens with an axial compression ratio equaled to or lowered than 0.11. As the bearing capacity dropped below 85% of the maximum bearing capacity of the specimen, an obvious bending deformation was observed.

(2) The hysteretic curves of UCFST columns were plump with no significant pinch phenomenon, and no descending stage was observed in the moment-curvature curve. Axial compression ratio had a negligible effect on the bending rigidity in the elastic stage. However, as the axial compression ratio increased, the yield moment firstly increased and then decreased; whereas the ultimate moment, final bending rigidity and moment reduction coefficient showed a decreasing trend. Increasing the steel ratio resulted in an increase in the bending rigidity in the elastic stage, yield moment, ultimate moment, curvature ductility coefficient, initial and final bending rigidity.

(3) Axial compression ratio and steel ratio had a small effect on the moment reduction coefficient, and no cross-sectional strength degradation was observed. As the axial compression ratio increased, the initial bending rigidity firstly increased and then decreased. In addition, the final bending rigidity and rigidity reduction coefficient decreased with the increase of deformation. Increasing the steel ratio could significantly improve the initial and final bending rigidity of the cross section, but had no effect on the rigidity reduction coefficient.

(4) Increasing the axial compression ratio resulted in a decrease in the energy

dissipation ability of UCFST columns; while the opposite could be obtained by increasing the steel ratio.

Chapter 3

Finite Element Analysis of UCFST Columns Hysteretic Behavior

Firstly, based on the pseudo-static test analysis of UCFST columns in Chapter 2, ABAQUS finite element analysis software was used to analyze the hysteretic behavior of UCFST columns, so as to better understand the working mechanism and failure mode of UCFST columns. Secondly, OpenSEES was used to simulate the UCFST columns, and the accuracy of the finite element model was verified by comparing with the experimental results and ABAQUS simulation results. Finally, the validated finite element model was used to analyze the expanded parameters of UCFST columns. The finite element parameters included axial compression ratio, steel ratio, steel yield strength and core concrete strength. The influence degree of each parameter on the main parameters of hysteretic curve skeleton curve of UCFST columns was analyzed.

3.1 Establishment of ABAQUS finite element model

3.1.1 Material constitutive model

3.1.1.1 Steel tube

Material hardening in ABAQUS includes ideal plasticity, isotropic hardening law, kinematic hardening law, mixed isotropic/kinematic hardening law and Johnson-Cook plasticity. Among them, ideal plasticity is suitable for impact analysis, forming analysis and general failure analysis, and isotropic hardening law is suitable for monotonic loading. In the case of cyclic loading, the motion hardening rule can only

be applied in/Standard, while Johnson-Cook plasticity can be applied to simulate high strain rate deformed metal materials, and can only be applied in/Explicit.

In this paper, the constitutive law of steel tube was described by the motion hardening rule, which included the bilinear follow-up hardening model and the non-linear follow-up hardening model. For high strength steel, the bilinear model was generally adopted, that was, the model only contained the elastic phase and the hardening phase, and the modulus of the hardening phase was 0.01 times that of the elastic phase, i.e. 0.01Es, as shown in Fig. 3-1.

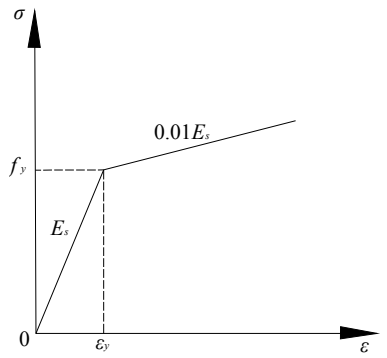

(a) Stress-strain relationship of steel tube

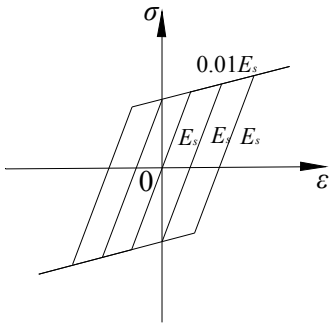

(b) Stress-strain relationship of steel tube under cyclic load

Fig. 3-1 Constitutive model of steel tube

According to the steel tube constitutive experimental data and the stress-strain relationship mentioned above, the constitutive characteristic values of steel tube corresponding to Q345 steel can be obtained, including elasticity modulus, Poisson's ratio, yield stress, ultimate stress and ultimate strain. The specific data of steel tube properties can be found in the pseudo-static test analysis of UCFST columns in Chapter 2.

3.1.1.2 Concrete

(1) Determination of uniaxial compression constitutive of UHPC

The constitutive relation and failure criterion of concrete are the basis of the structural non-linear finite element analysis and design theory, which affect the development of materials. The stress-strain relation of structural materials is the summary of the relationship between material force and deformation in the structural loading process.

Up to now, many scholars have put forward many kinds of stress-strain curve equations of concrete under axial compression, and some literatures have also been reviewed and commented on. For UCFST members, under the action of external steel tube, UHPC is in a three-dimensional compressive state. At this time, the uniaxial constitutive law of unconfined UHPC cannot be used alone, so the confined concrete constitutive relationship was adopted.

a. Yan Guangjie's UHPC uniaxial compression constitutive

Yan (2005), Yan and Yan (2007) carried out uniaxial compression, biaxial tension-compression and conventional triaxial tests on UHPC specimens respectively. Based on Wang et al.'s constitutive equation, the mathematical expressions of the constitutive model of UHPC under uniaxial compression were derived, as shown in the following Eq. (3-1) and Eq. (3-2). The failure criteria, initial yield criteria and non-uniformity strengthen criteria of UHPC specimens under complex stresses were established.

Ascending phase: $$y=\frac{Ax-x^2}{1+(A-2)x} \qquad 0\le x<1 \tag{3-1}$$

Descending phase: $$y=\frac{Bx}{1+(B-2)x+x^2} \qquad x\ge 1 \tag{3-2}$$

b. Mander's uniaxial compressive constitutive law of confined concrete

Based on the results of Popovics, a stress-strain constitutive model of concrete confined by stirrups with different cross-section shapes was proposed by Mander et al. (1988). The mathematical expressions are as the following Eq. (3-3). Among them, $f_{cc}^{'}$ and ε_c are the compressive strength of concrete confined by stirrups and the corresponding peak strain; $f_{c0}^{'}$ and ε_{c0} are the unconfined concrete strength and corresponding strain respectively; E_c is concrete elasticity modulus. And the stress-strain curve is shown in Fig. 3-2.

$$f_c=\frac{f_{cc}^{'}xr}{r-1+x^r} \tag{3-3}$$

where $x=\frac{\varepsilon_c}{\varepsilon_{cc}}$, $\varepsilon_{cc}=\varepsilon_{c0}\left[1+5\left(\frac{f_{cc}^{'}}{f_{c0}^{'}}-1\right)\right]$, $r=\frac{E_c}{E_c-E_{\sec}}$, $E_c=5000\sqrt{f_{c0}^{'}}MPa$, $E_{\sec}=\frac{f_{cc}^{'}}{\varepsilon_{cc}}$ 。

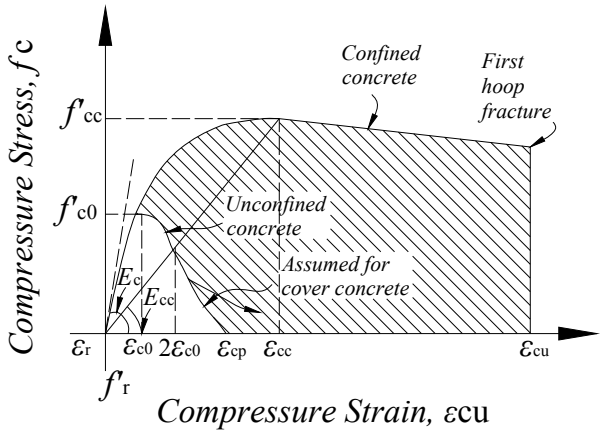

Fig. 3-2 Mander's constitutive of confined and unconfined concrete

c. Saenz's constitutive of confined concrete under uniaxial compression

Saenz's constitutive model of confined concrete (Seanz, 1964) based on the diameter-thickness ratio of steel tube, as shown in Fig. 3-3. The stress-strain relationship is shown in the following Eq. (3-4) and Eq. (3-5). Among them, f_1 is the confined compressive stress of steel tube to core concrete, E_c is the elasticity initial modulus of concrete, which is related to the compressive strength of concrete as $E_c = 4700\sqrt{f_c'}$, f_c' is taken as the concrete compressive strength and it is the same as that of the Mander's model. ε_c' is the corresponding strain of f_c', which is the same as that of the Mander's model.

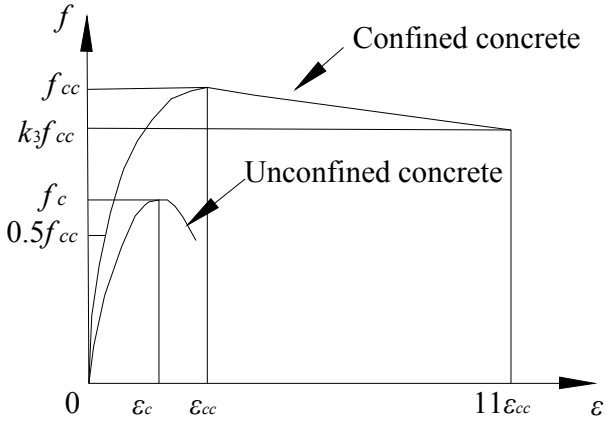

Fig. 3-3 Saenz's constitutive of confined concrete under uniaxial compression

Ascending phase: $$f_c = \frac{E_c \varepsilon_c}{1 + (R + R_E - 2)(\frac{\varepsilon_c}{\varepsilon_{cc}^{'}}) - (2R - 1)(\frac{\varepsilon_c}{\varepsilon_{cc}^{'}})^2 + R(\frac{\varepsilon_c}{\varepsilon_{cc}^{'}})^3} \quad (3\text{-}4)$$

where $R = \frac{R_E(R_\sigma - 1)}{(R_\varepsilon - 1)^2} - \frac{1}{R_\varepsilon}$, $R_E = \frac{E_c \varepsilon_{cc}^{'}}{f_{cc}^{'}}$, $f_{cc}^{'} = f_c^{'} + k_1 f_1$, $\varepsilon_{cc}^{'} = \varepsilon_c^{'}(1 + k_2 \frac{f_1}{f_c^{'}})$;

$k_1 = 4.1, k_2 = 20.5$; R_σ=4, R_ε=4 .

The descending phase is linear, and the stress-strain relationship at the end is respectively:

$$f_c = k_3 f_{cc}^{'} \qquad \varepsilon_c = 11\varepsilon_{cc}^{'} \quad (3\text{-}5)$$

where $\frac{f_1}{f_y} = \begin{cases} 0.043646 - 0.000832(\frac{D}{t}) & (21.7 \le D/t \le 47) \\ 0.006241 - 0.00003557(\frac{D}{t}) & (47 \le D/t \le 150) \end{cases}$;

$$k_3 = \begin{cases} 1 & (21.7 \le D/t \le 47) \\ 0.0000339(\frac{D}{t})^2 - 0.010085(\frac{D}{t}) & (47 \le D/t \le 150) \end{cases}$$

d. Han Linhai's constitutive of confined concrete under uniaxial compression

By sorting out and calculating the test results of more than 400 CFST short specimens under axial compression, considering the influence of confinement coefficient, the stress-strain relationship model of the core concrete was proposed as the following Eq. (3-6) and Eq. (3-7) by Han (2004). The stress-strain curves are shown in Fig. 3-4.

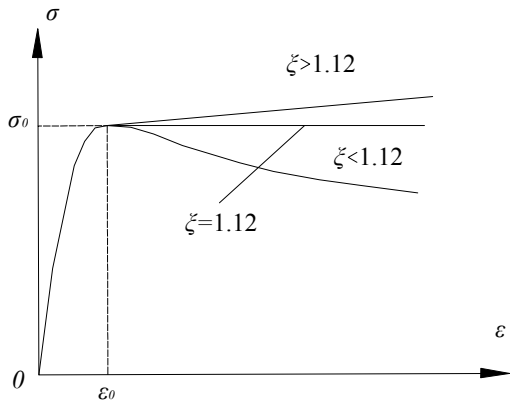

Fig. 3-4 Han Linhai's constitutive of confined concrete

$$y = 2x - x^2 \quad (3\text{-}6)$$

$$(x \le 1)$$

$$y = \begin{cases} 1+q\left(x^{0.1\xi}-1\right) & (\xi \ge 1.12) \\ \dfrac{x}{\beta(x-1)^2+x} & (\xi < 1.12) \end{cases} \qquad (x > 1) \tag{3-7}$$

where $y = \sigma / \sigma_0$; $x = \varepsilon / \varepsilon_0$; $\sigma_0 = \left[1+\left(-0.054\xi^2+0.4\xi\right)\cdot\left(\dfrac{24}{f_c'}\right)^{0.45}\right]\cdot f_c'$;

$\varepsilon_0 = \varepsilon_{cc} + \left[1400+800\left(\dfrac{f_c'}{24}-1\right)\right]\cdot\xi^{0.2}$ $(\mu\varepsilon)$; $\varepsilon_{cc} = 1300+12.5\cdot f_c'$ $(\mu\varepsilon)$;

$q = \dfrac{\xi^{0.745}}{2+\xi}$; $\beta = \left(2.36\times10^{-5}\right)^{0.25+(\xi-0.5)^7}\cdot f_c'^{2}\cdot 3.51\times10^{-4}$.

In order to select the concrete constitutive model suitable for the finite element analysis of the hysteretic behavior of UCFST columns, the three constitutive models of Yan Guangjie's UHPC uniaxial compression constitutive, Saenz's constitutive of confined concrete under uniaxial compression and Han Linhai's constitutive of confined concrete under uniaxial compression were applied to the finite element analysis of the axial compressive performance of UCFST columns. The experimental results in the literature were compared to verify the applicability of each constitutive model. The results are shown in Fig. 3-5 below.

Taking the above constitutive relationships as the constitutive model of UHPC, ABAQUS was adopted to analyze 82 UCFST short columns in relevant literature. The application of different concrete constitutive models in the finite element analysis of UCFST columns was studied. Among the three concrete constitutive models, the error of the finite element results obtained by the Han Linhai's confined concrete constitutive model in the simulation of UCFST columns under axial compression was the smallest, and during the whole process of axial compression, the results of each phase were most consistent with the test results, so it can be seen that Han Linhai's confined concrete constitutive model under axial compression was the most consistent with the test results. Thus, in this paper, Han Linhai's confined concrete constitutive model was used as the UHPC axial compression constitutive model to carry out the

finite element analysis.

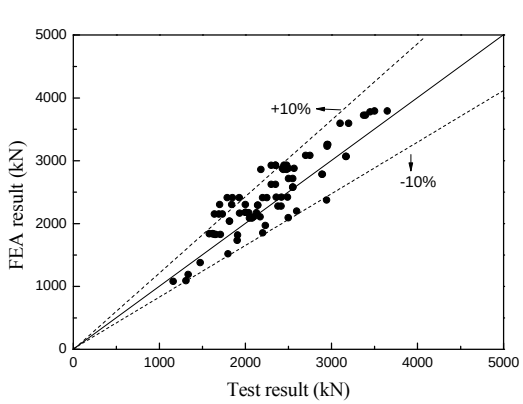

(a) Han Linhai's

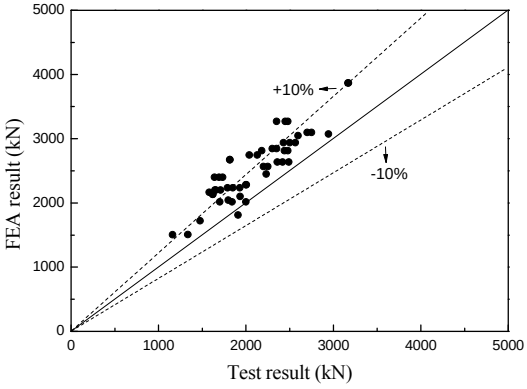

(b) Saenz's

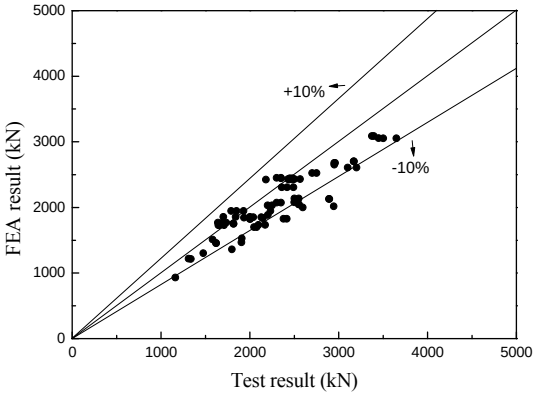

(c) Yan Guangjie's

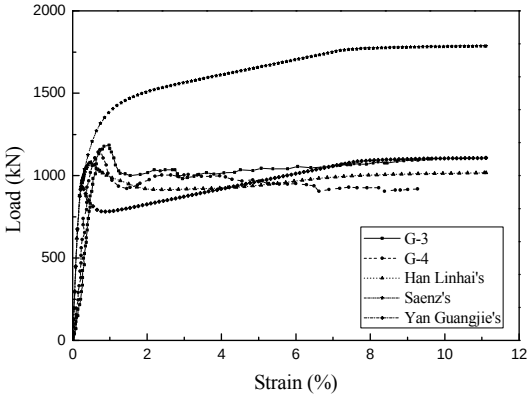

(d) Comparing results with the test results in literate

Fig. 3-5 Comparison of different constitutive of confined concrete

(2) Uniaxial tensile constitutive of UHPC

Shen's tension concrete constitutive equation (Shen, 1993) was adopted as the UHPC uniaxial tension constitutive, as shown in the following Eq. (3-8), where σ_p is the peak tension stress and ε_p is the peak tension strain.

$$y=\begin{cases}1.2\left(\varepsilon/\varepsilon_b\right)-0.2\left(\varepsilon/\varepsilon_b\right)^2 & \varepsilon\le\varepsilon_b\\ \dfrac{\left(\varepsilon/\varepsilon_b\right)}{0.31\sigma_p^2\left(\varepsilon/\varepsilon_b-1\right)^{1.7}+\left(\varepsilon/\varepsilon_b\right)} & \varepsilon>\varepsilon_b\end{cases} \tag{3-8}$$

where $\sigma_p=0.26\left(1.25f_c^{'}\right)^{\frac{2}{3}}$, $\varepsilon_p=43.1\sigma_p\cdot10^{-6}$.

(3) Determination of damage coefficient *d* of UHPC damage model

From the macroscopic point of view, most materials and structures inevitably have macroscopic crack lines. Before their appearance, micro cracks and micro voids have been generated. The appearance and expansion of micro defects in materials and structures are called damage. Damage coefficient *d* can be used to describe the damage process of structures. In the process of ABAQUS modeling, the damage constitutive model of concrete was selected to define the attributes of UHPC. In this paper, the formula of damage coefficient *d* in Birtel and Mark' model (Birtel and Mark, 2006) was used to calculate the compression (tension) damage factors needed in the numerical simulation, as shown in Eq. (3-9) and Eq. (3-10).

$$d_c = 1 - \frac{\sigma_c \cdot E_c^{-1}}{\varepsilon_c^{pl} \cdot (1/b_c - 1) + \sigma_c \cdot E_c^{-1}} \tag{3-9}$$

$$d_t = 1 - \frac{\sigma_{t0} E_c^{-1}}{\varepsilon_t^{pl} (1/b_t - 1) + \sigma_{t0} E_c^{-1}} \tag{3-10}$$

According to the test data obtained from UHPC material properties test, and combined with the above-mentioned confined concrete constitutive and damage coefficient calculation method, a series of data required by concrete damage model in ABAQUS were obtained, and the constitutive characteristic data of UHPC were completed.

3.1.2 ABAQUS finite element modeling process

3.1.2.1 Cell selection and mesh generation

ABAQUS provides different element types to choose from, such as eight-node linear hexahedron element C3D8R, six-node maternal triangular prism element C3D6, quadruple-node linear tetrahedron element C3D4 and shell element S4R. In order to reduce integration and finite hourglass control, all components in this model used eight-node linear hexahedron element C3D8R, including steel pipe, core UHPC, end plate and intermediate fixture. After meshing each part, the results of different parameters of UCFST columns were different. Taking GU-T8-L19-N11 as an example, the core UHPC was divided into 960 units, 1197 nodes, steel tube was divided into 320 units, 672 nodes, the end plate was divided into 64 units and 162 nodes

respectively and the fixture was divided into 32 units and 96 nodes. The model in this paper is partitioned as shown in Fig. 3-6.

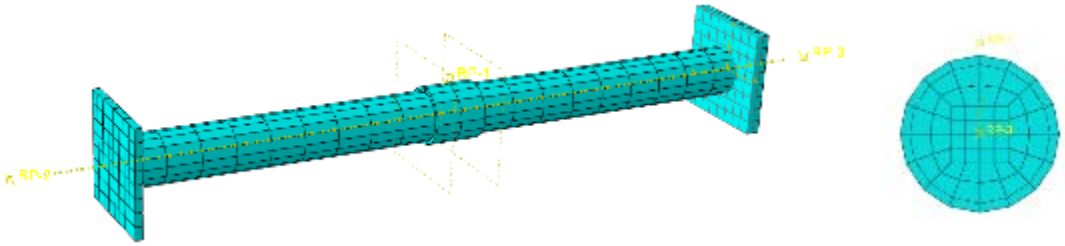

Fig. 3-6 Mesh generation diagram

3.1.2.2 Boundary conditions and loading

Whether a model can successfully reflect the results of the actual test depends on the constraints of the model to reflect the constraints of the actual columns. Consistent with the actual force, the square end plates with the dimensions of 150mm×150mm and the thickness of 20mm were set at the left and right ends of the column, which were bound to the two ends of the column respectively. In order to apply the vertical displacement load of the MTS actuator to the column, a rigid fixture was designed, which can be seen in Chapter 2. In this paper, a ring fixture with an inner diameter of 70 mm, an outer diameter of 80 mm and a length of 150 mm was established, which was placed in the middle of the column and bounded with the outer steel tube to simulate the rigid fixture in the test. In order to transfer the force to the component better, a reference point RP2 and RP3, coupled with the left and right end plates of the column respectively, were established at the left and right ends of the model. And a reference point RP1 was established above the ring fixture in the middle of the column, which was coupled with the ring fixture.

In this paper, the front and posterior fixture supports of UCFST columns were articulated when they were subjected to actual loads. Therefore, for reference point RP2, the displacement in X, Y direction and the rotation angles in Y and Z direction were restrained to release the displacement in Z direction and the rotation angle in X direction; for reference point RP3, the displacement in X, Y and Z direction was restrained to release the rotation angles in X, Y and Z direction.

Consistent with the loading method in the test, taking the loading condition of GU-T8-L19-N11 as an example, 446 kN concentrated force was applied to the reference point RP2 bounded to the left steel plate in the model, and a cyclic displacement load was applied to the reference point RP3 bounded to the ring fixture. The specific loading system was consistent with the test, and the boundary strip of the model and loading process are shown in Fig. 3-7 below.

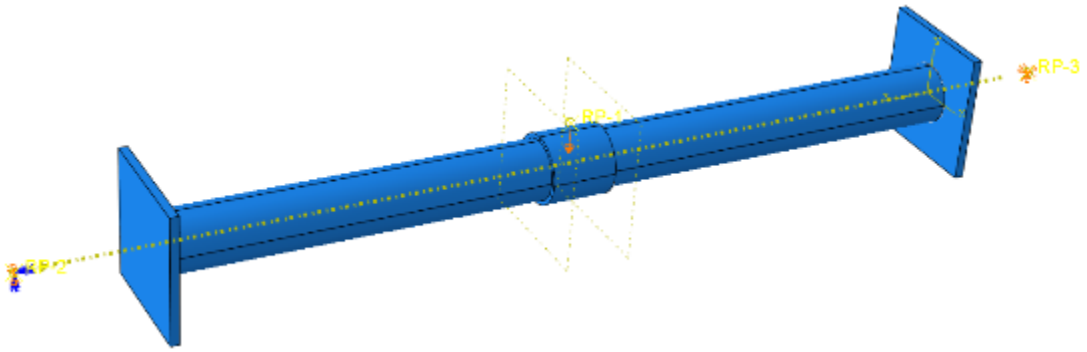

Fig. 3-7 Boundary and loading conditions of UCFST column model

3.1.2.3 Interaction

The main constraints in ABAQUS include binding constraints, rigid bodies, display bodies, coupling, multi-point constraints, shell-entity coupling and so on. The motion relationship is transferred between nodes. Two constraints were adopted in this model, namely binding constraints and coupling. As mentioned in the preceding section, the binding constraints between the left and right end plates and the ring fixture and the UCFST column were surface-to-surface, and the coupling constraints between the three reference points and the two end plates and the ring fixture were point-to-surface.

The interaction of the model also included a contact. The hard contact between the outer steel tube and the core UHPC can transfer the force on the surfaces of the two parts. The contact had three contact attributes: tangential behavior, normal behavior and geometric property. In the normal direction, the force perpendicular to the contact surface can be completely transferred between the interfaces. In the tangent direction, the shear stress at the interface between the steel tube and the core UHPC was

transferred by setting a Coulomb friction model with friction coefficient of 0.25 until the shear stress reached the critical value, as shown in Fig. 3-8.

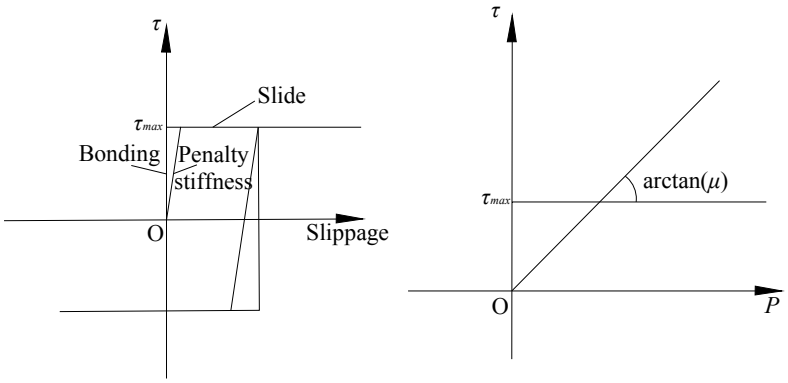

Fig. 3-8 Interface friction and slip critical shear stress

3.2 Component failure patterns

Fig. 3-9 shows the deformation cloud of UCFST columns after cyclic load, which was modeled by ABAQUS. It can be seen that the plastic hinges of UCFST members under cyclic load occurred within a very close range from both sides of the rigid. When the specimen was damaged, the stress on the upper and lower surfaces of the steel tube on both sides of the rigid fixture was the largest, and most of the columns appeared local bulging state. From the graph, it can be seen that the stress on the upper and lower surfaces of steel tubes was not the same. The stress on one side of the curved surface was larger than that on the other side, and the buckling degree of one side of the curved surface was more obvious than that on the other side. For example, when GU-T8-L19-N03 was damaged, the steel tube on one side appeared to be pulled apart, which was consistent with the stress reprogram described in figure (a). With the increase of the axial compression ratio, the stress of each component decreased gradually from the two sides of the rigid fixture to the two ends of the column. However, the stress of both sides of the rigid fixture decreased continuously, and the local bulging phenomenon of the column became less and less obvious. With the increase of steel ratio, the stress distribution range of the columns increased continuously when they were damaged, but the stress on both sides of rigid decreased

continuously, and the degree of bulging decreased with the increase of steel ratio. The failure phenomena of the columns simulated by the above finite element method were consistent with those in the test.

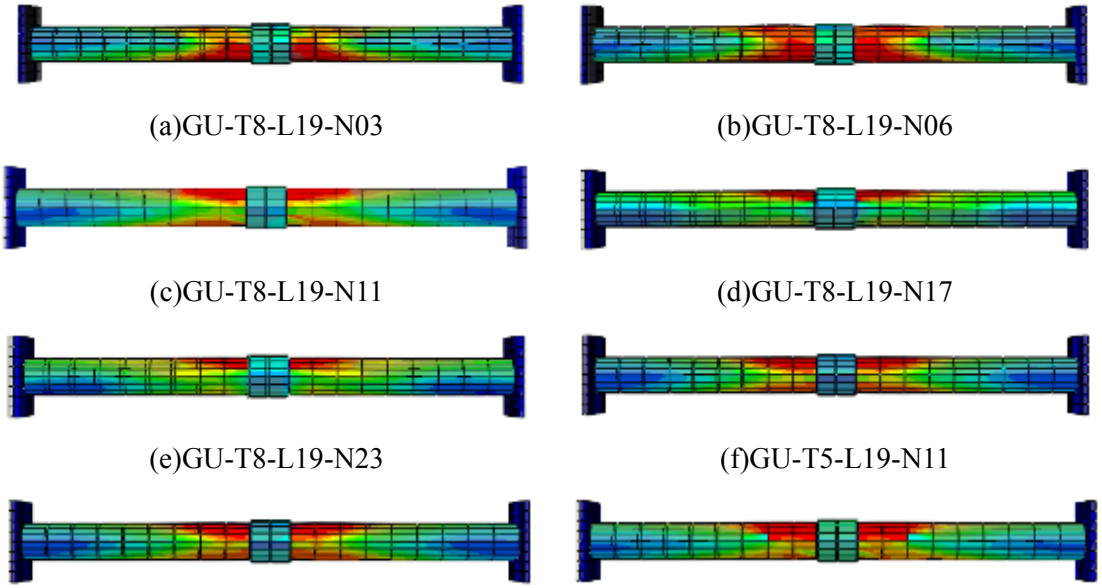

(a)GU-T8-L19-N03 (b)GU-T8-L19-N06

(c)GU-T8-L19-N11 (d)GU-T8-L19-N17

(e)GU-T8-L19-N23 (f)GU-T5-L19-N11

(g)GU-T6-L19-N11 (h)GU-T10-L19-N11

Fig. 3-9 Deformation cloud of UCFST columns

3.3 Establishment of OpenSEES finite element model

3.3.1 Section fiber division and element selection

OpenSEES material library provides a variety of cross-section types, such as elastic cross-section, uniaxial cross-section, fiber cross-section (Mazzoni et al., 2004). The fiber cross-section satisfies the assumption of flat cross-section and ignores shear deformation. It divided the whole cross-section into many small fibers, including outer steel tube and core UHPC, and assigned different constitutive relations to fibers in different regions. Therefore, the fiber cross-section was selected to simulate the composite section of UCFST columns, and the stiffness of the section was calculated by OpenSEES (Xie et al., 2012).

The section of UCFST column included UHPC section and steel tube section, as shown in Fig. 3-10. The number of fiber units in the section affected the accuracy of

calculation. In this paper, the section of UHPC was divided into 30 parts in the circumferential direction and 15 parts in the radial direction by Patch order. The section of steel tube was divided into 30 parts in the circumferential direction and 2 parts in the radial direction, as shown in Fig. 3-10.

According to the existing element type of OpenSEES (Ning and Duan, 2009), the finite element model of UCFST columns was established by using the non-linear beam-column macro-element in the bar system model.

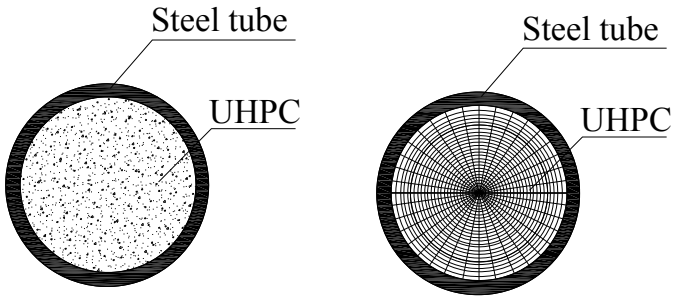

Fig. 3-10 Fiber section partition diagram of UCFST column

3.3.2 Material constitutive relation

(1) Constitutive model of steel tube

OpenSEES provides three steel constitutive models: Steel01, Steel02 and Reinforcing Steel.

Steel02 can well simulate the development process of steel from elastic phase to plastic phase after yield and the Bauschinger effect of steel. The input of parameters is simple, and the calculation efficiency of the model is high and easy to converge. It is suitable for simulating repeated loading and unloading of steel. Steel01 is similar to Steel02, but Steel01 is unable to simulate the properties of steel under repeated loading without considering the Bauschinger effect of steel. Compared with Steel02, Reinforcing Steel model not only considers the equivalent reinforcement and Bauschinger effect of steel bars, but also defines the degradation of steel strength and stiffness caused by buckling and repeated loading of steel tubes and simulates the fracture of steel bars. However, due to the large number of parameters, the calculation

process was slow, and considering that the strength and stiffness degradation of the specimens was not obvious during the test process, the Reinforcing Steel model was not suitable. The Steel02 model provided by OpenSEES can accurately simulate the hysteretic behavior of steel tubes under repeated loads. Therefore, Steel02 model was used as the constitutive model of steel. The hysteretic response-strain curve of Steel02 material is shown in Fig. 3-11.

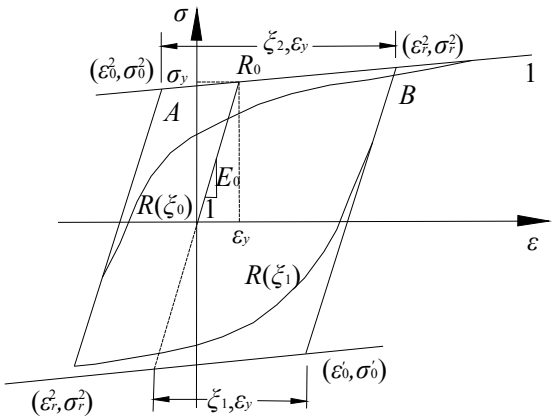

Fig.3-11 Hysteretic stress-strain relation curve of Steel02

(2) Constitutive model of concrete

A variety of concrete hysteretic constitutive models are provided in OpenSEES, of which Concrete01 model and Concrete02 model are the most widely used. The compressive skeleton curves of these two models are based on the modified Kent-Park uniaxial concrete model, but Concrete02 takes into account the tensile behavior of concrete. As the UHPC selected in this paper was not doped with steel fibers, the tensile strength can be neglected. Therefore, the Conrete01 model was adopted in the core UHPC constitutive model, and the stress and strain at the peak point and the limit point in the Conrete01 model were selected with appropriate confined concrete stress-strain relationship. In this paper, Han Linhai's confined concrete stress-strain relationship was adopted to simulate the core UHPC in OpenSEES modeling.

3.4 Verification of the two finite element models

3.4.1 Load-displacement hysteresis curve

Fig. 3-12 compares the load-displacement hysteretic curves of UCFST columns with those obtained by finite element method using ABAQUS and OpenSEES software respectively. It can be seen that the shape of load-displacement hysteresis curves of UCFST columns was relatively full, and there was no obvious pinching phenomenon, regardless of whether there was a downward phase of load-displacement hysteresis curve or not, which conformed to the hysteresis curve characteristics of CFST structures. The results of the finite element simulation in this paper were basically in agreement with the experimental results, in which the stiffness of the hysteretic curve of the finite element was larger than that of the hysteretic curve of the test. The main reasons were as follows: firstly, in the finite element simulation analysis, the simulated environment was ideal, only considering the bending deformation of the UCFST columns, but not the shear deformation, which made the stiffness of the hysteretic curve of the finite element analysis on the high side. Another reason was that in the quasi-static test of UCFST columns, there were joint gaps and friction forces between the columns and the components of the test device, which were set as relatively ideal constraints in the finite element method, thus resulting in the lower stiffness of the actual test curve. With the increase of the axial compression ratio, the more difficult it was to control the axial force, the more obvious this phenomenon was. For example, in this batch of UCFST columns, the stiffness of columns whose axial compression ratio was greater than or equal to 0.11 was worse.

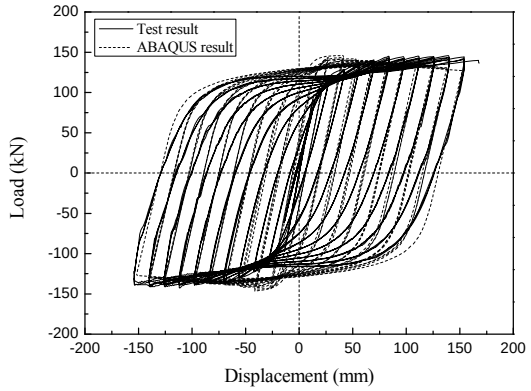

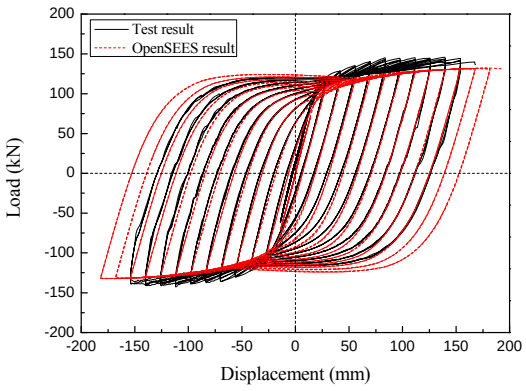

(a)GU-T8-L19-N03

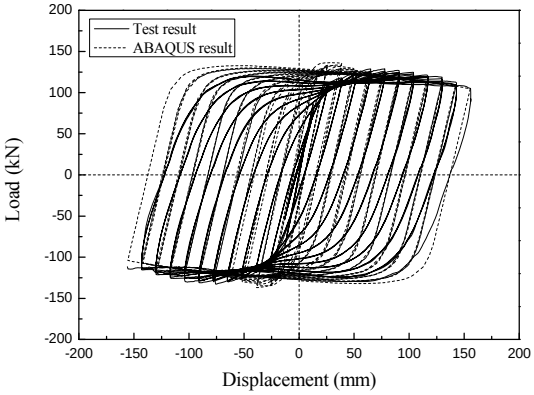

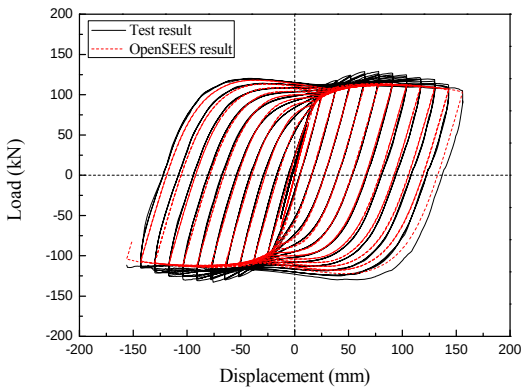

(b)GU-T8-L19-N06

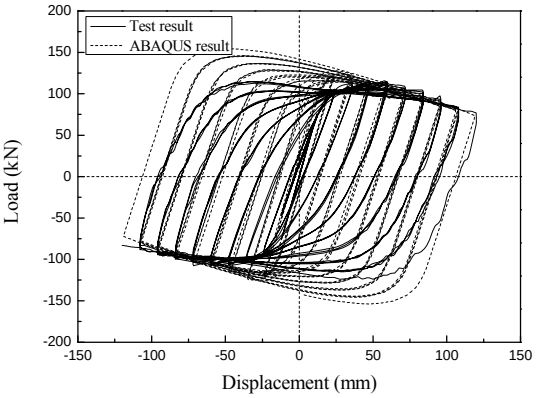

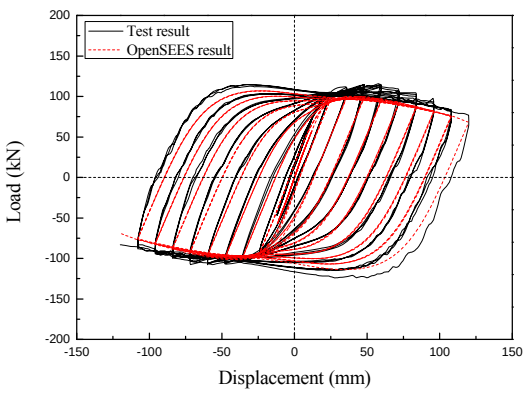

(c)GU-T8-L19-N11

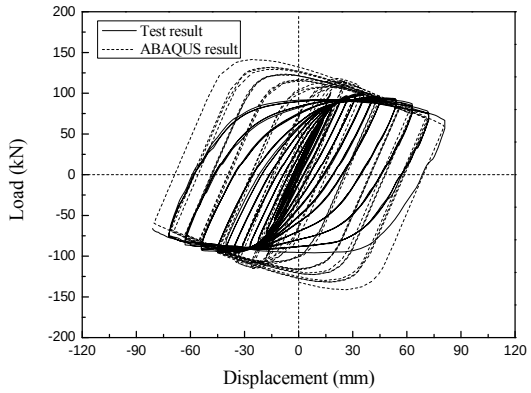

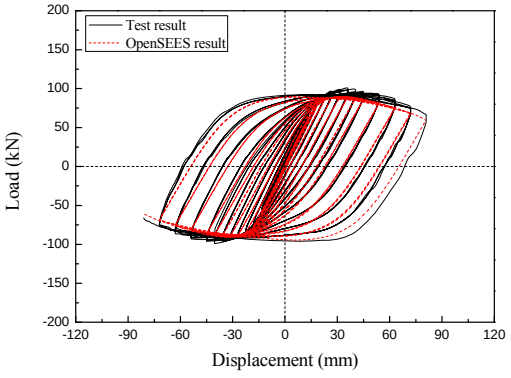

(d)GU-T8-L19-N17

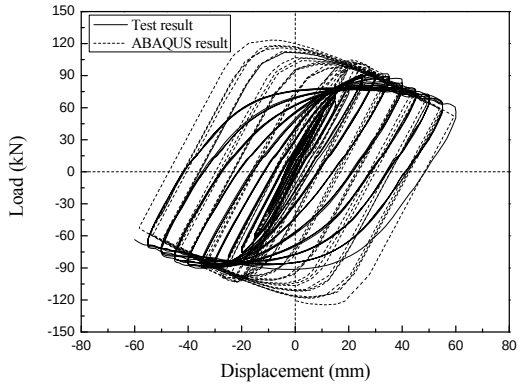

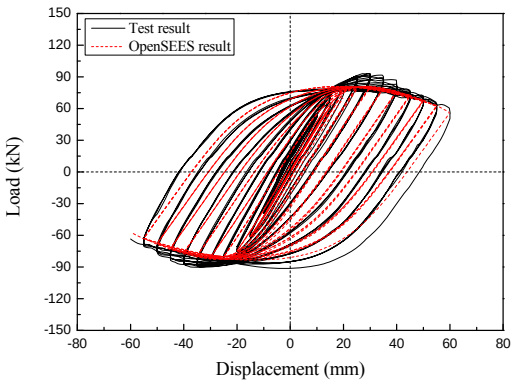

(e)GU-T8-L19-N23

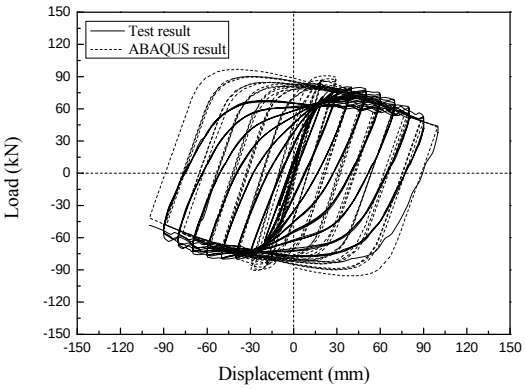

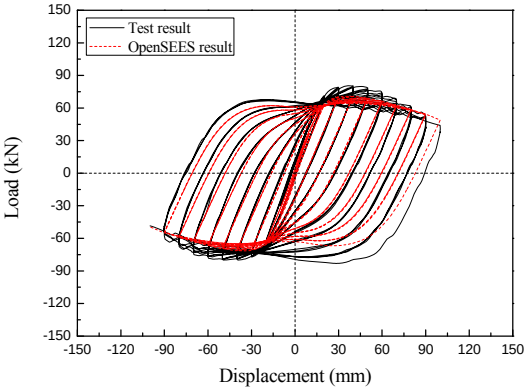

(f)GU-T5-L19-N11

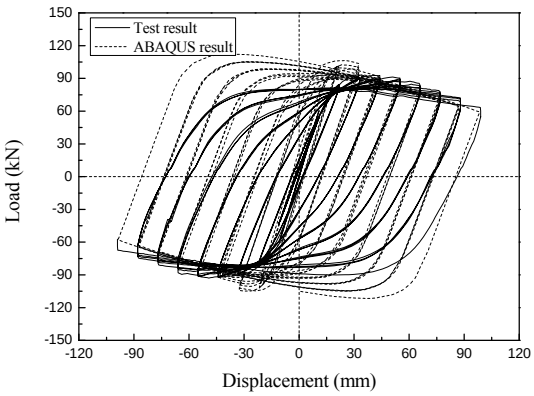

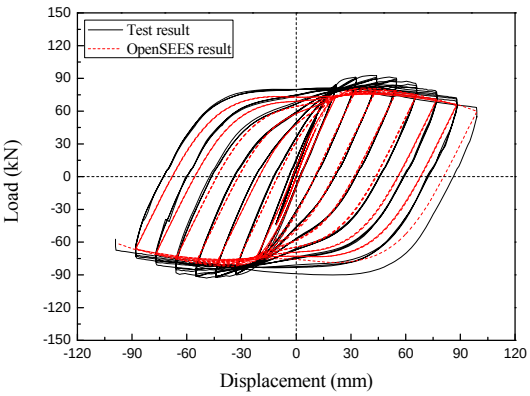

(g)GU-T6-L19-N11

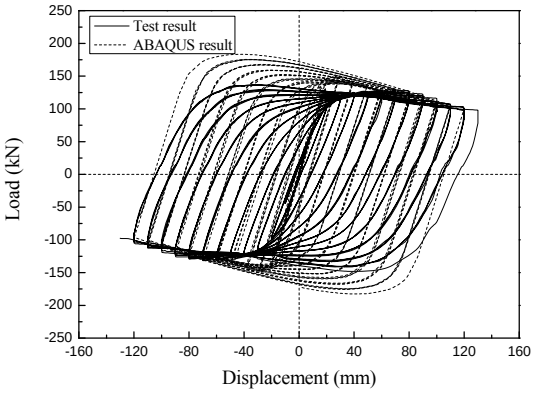

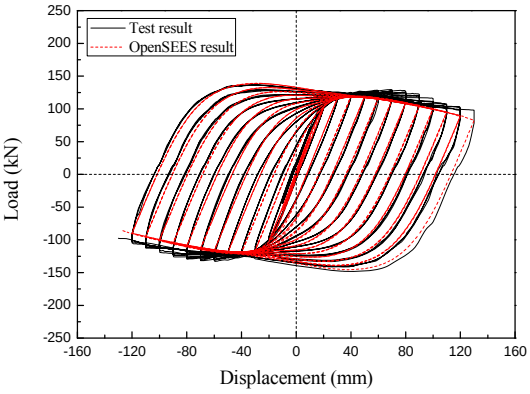

(h)GU-T10-L19-N11

Fig. 3-12 Comparation of the load-displacement hysteretic curves of UCFST columns

3.4.2 moment-curvature hysteresis curve

Fig. 3-13 compares the moment-curvature hysteresis curves of UCFST columns obtained by finite element method using ABAQUS and OpenSEES software with the experimental result respectively. It can be seen that the moment-curvature hysteresis curves of UCFST columns obtained by the two finite element methods were in good agreement with those obtained by experiment. There was no obvious descending phase in the skeleton curves of the two FEA results, which indicated that their angular performance was good. It can also be seen by comparison of the two FEA results that there were some differences between them. And the difference increased with the increase of the axial compression ratio. The main reasons were as follows: the finite element simulation ignored the factors such as the thickness of steel, the uneven pouring of UHPC, the welding quality of end plate and component, and the slip between steel tube and UHPC during the test, which made the stiffness of the moment-curvature hysteretic curve of the finite element increase. Moreover, the lateral support device, the friction resistance of pin support rotation and the deflection of actuator loading head all affected the test results, which reduced the stiffness of the moment-curvature hysteretic curve obtained by the test, so there was a certain deviation between the two, but they can meet the requirements on the whole.

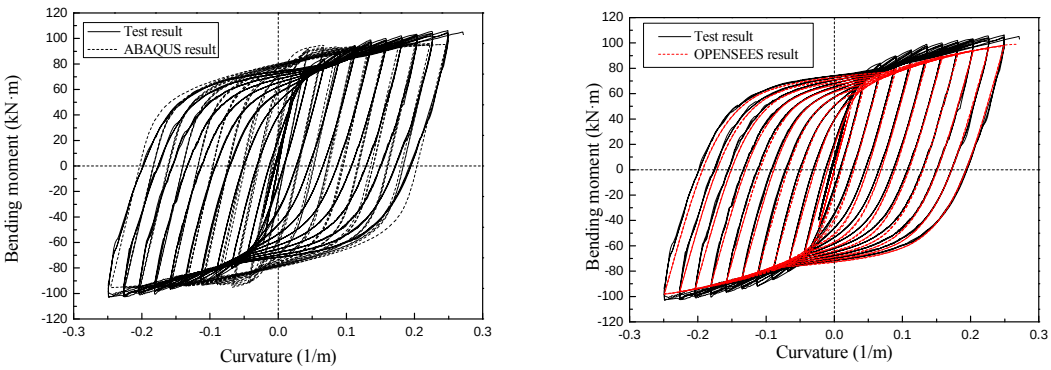

(a)GU-T8-L19-N03

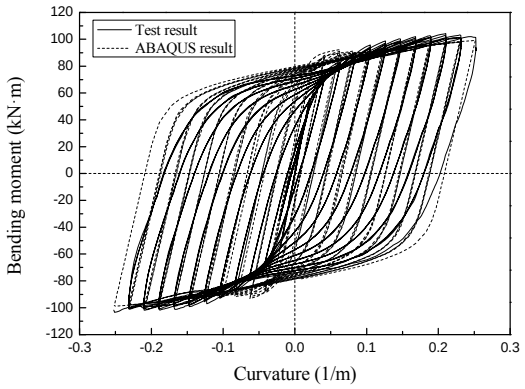

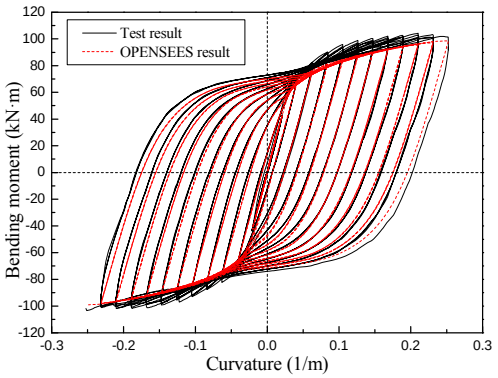

(b)GU-T8-L19-N06

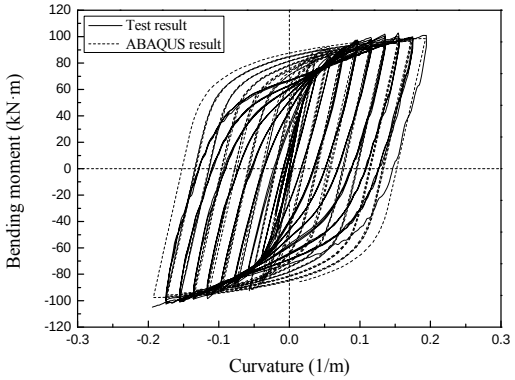

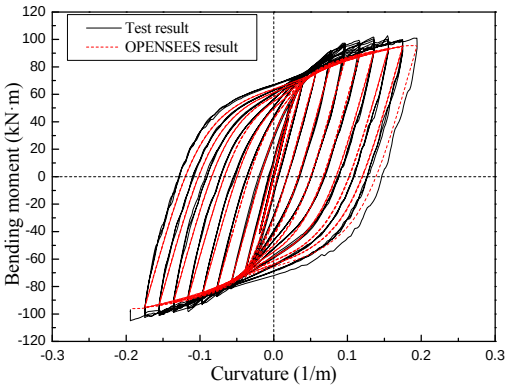

(c)GU-T8-L19-N11

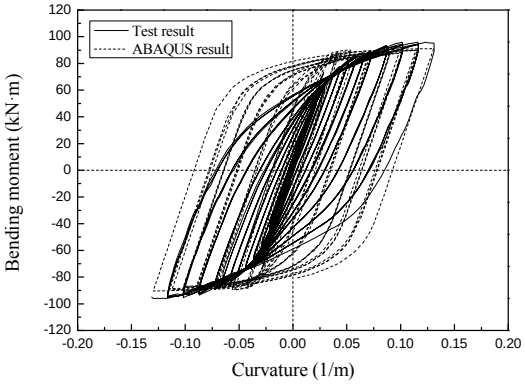

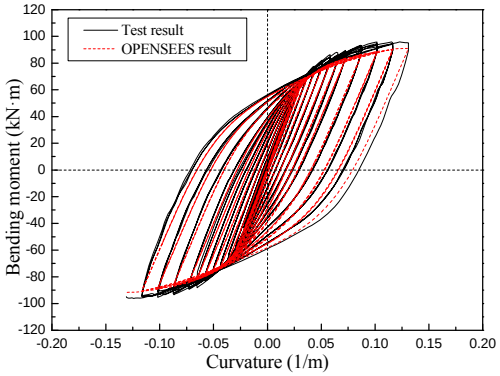

(d)GU-T8-L19-N17

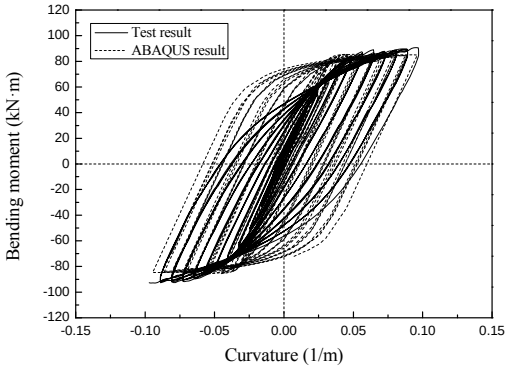

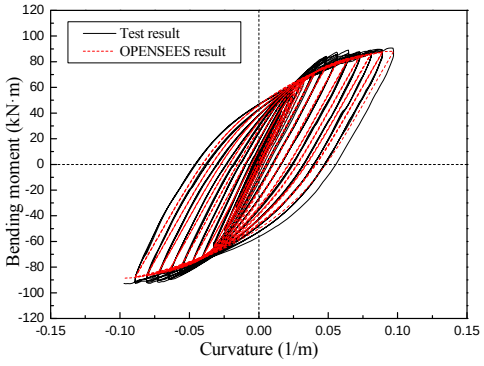

(e)GU-T8-L19-N23

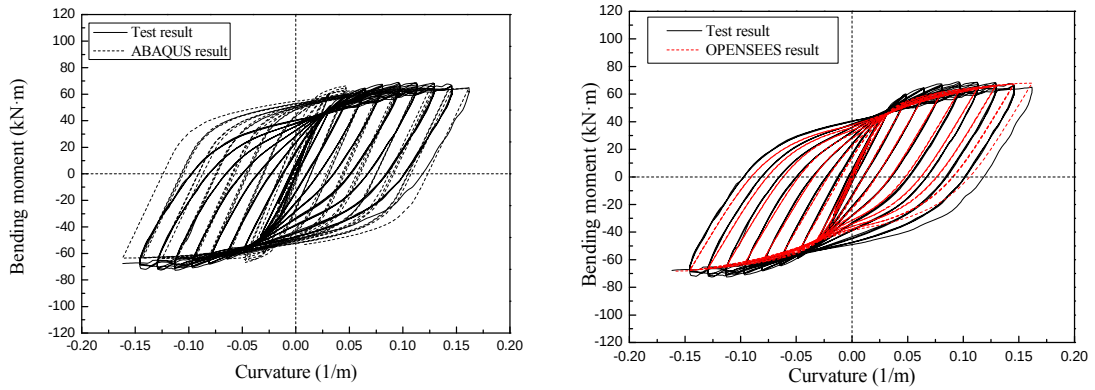

(f)GU-T5-L19-N11

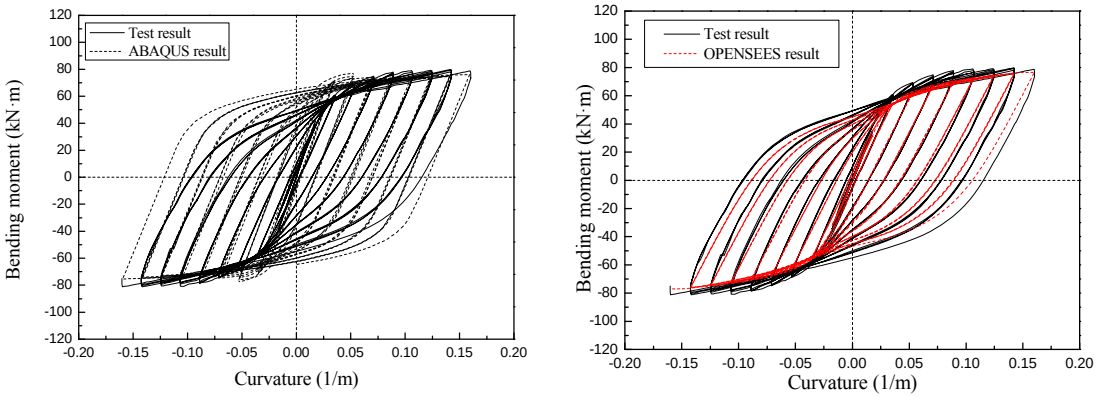

(g)GU-T6-L19-N11

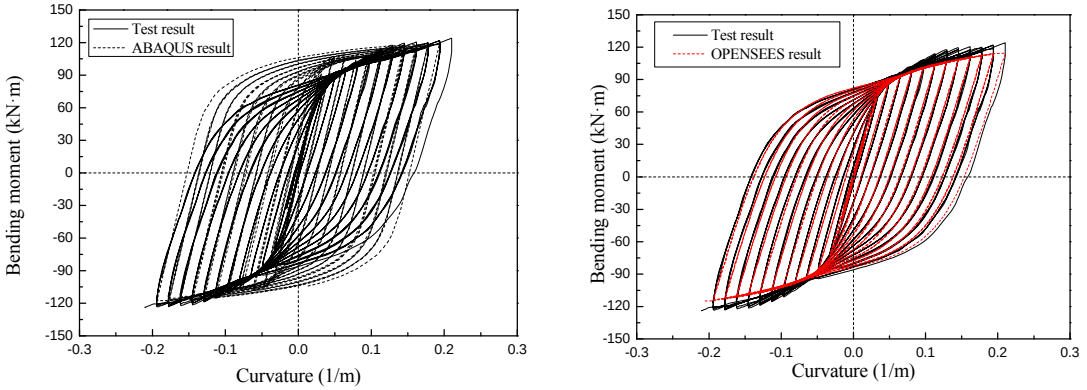

(h)GU-T10-L19-N11

Fig. 3-13 Comparison of moment-curvature hysteresis curves

By comparing the finite element results with the test results, it can be concluded that the above-mentioned finite element analysis method can simulate the hysteretic behavior of UCFST columns perfectly. Therefore, in order to obtain the effect of different parameters on the characteristic points of the hysteretic curve of UCFST columns, the above-mentioned OpenSEES finite element analysis method was adopted to expand the hysteretic behavior of UCFST columns. The hysteretic

behavior of UCFST columns with large parameters was analyzed, which provided a finite element basis for subsequent establishment of hysteretic model of UCFST members.

3.5 Finite element parameter analysis

Considering the limitation of specimen fabrication, loading time and test site, only two main parameters, axial compression ratio and steel ratio, were selected for specimen design. In order to establish the general skeleton curve model of UCFST columns and fully understand the hysteretic behavior of UCFST columns, more test results were needed to analyze and verify. Therefore, using the above OpenSEES finite element model verified by the test results, on one hand, the range of parameters was enlarged, on the other hand, more parameters were selected to design the specimens and establish the finite element model to analyze the plastic bending performance of UCFST columns. Table 3-1 shows the parameters of the finite element benchmark model which have been verified by experiments. The moment-curvature curves are listed in the following parameter analysis. The load-displacement curves are shown in Appendix I.

Table 3-1 Main parameters of finite element benchmark model

Length L_s(mm)	1900	Strength of UHPC (MPa)	135
Thickness t(mm)	8	Elasticity modulus of UHPC (MPa)	43000
Outside diameter D(mm)	140	Yield strength of steel tube (MPa)	390
Axial compression ratio n	0.11	Elasticity modulus of steel tube (MPa)	201000

3.5.1 Axial Compression Ratio

With 0, 0.03, 0.06, 0.11, 0.17, 0.23, 0.3, 0.4 and 0.5 as the axial compression ratio, the remaining parameters remained unchanged, as shown in Table 3-2. Fig. 3-14 shows the moment-curvature hysteresis curves of UCFST columns under different axial compression ratios. Fig. 3-15 shows the moment-curvature skeleton curves of the specimens with different axial compression ratios. The key values of the skeleton curves are listed in Table 3-3.

Table 3-2 Axial compression ratio model parameters

Length L_s (mm)	1900	Strength of UHPC (MPa)	135
Thickness t (mm)	8	Elasticity modulus of UHPC (MPa)	43000
Outside diameter D (mm)	140	Yield strength of steel tube (MPa)	390
Axial compression ratio n	0、0.03、0.06、0.11、0.17、0.23、0.30、0.40、0.50	Elasticity modulus of steel tube (MPa)	201000

In Fig. 3-15, when the axial compression ratio increased from 0 to 0.11, the elastic bending stiffness increased by l3.2% While when the axial compression ratio increased from 0.11 to 0.5, the elasticity stiffness decreased by 13.3%. Thus, in Fig. 3-6, the skeleton curves of UCFST columns were slightly different in the elastic stage; The yield curvature was reduced by 56.79%. And when the axial compression ratio was less than 0.5, the elasticity stiffness decreased by a little. When the axial compression ratio was 0.4 and 0.5, the yield moment decreased by 8.24% and 22.83%, respectively. When the axial compression ratio increased from 0 to 0.5, the yield curvature decreased by 56.79%, the ultimate bending moment decreased by 86.73%, and the curvature ductility coefficient decreased by 69.42%, while the stiffness of the strengthening phase increased gradually and changed greatly. Although the axial compression ratio increased, strengthening stiffness also increased, which may be due to the reduction of the ductility of the specimens, resulting in the reduction of yield curvature and ultimate curvature. While the second-order effect of the axial force had a greater impact on the ultimate bending moment, resulting in a smaller decrease in strengthening stiffness, which leaded to the increase of strengthening stiffness. When the axial compression ratio was greater than 0.11, the curvature ductility coefficient was less than 3, and the seismic performance of the specimens decreased. Therefore, the increase of axial compression ratio had a great influence on the hysteretic behavior of UCFST columns.

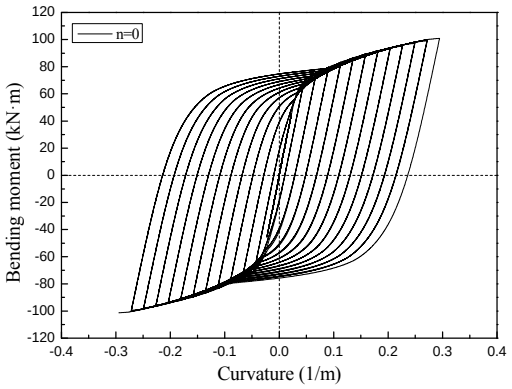

(a) n=0

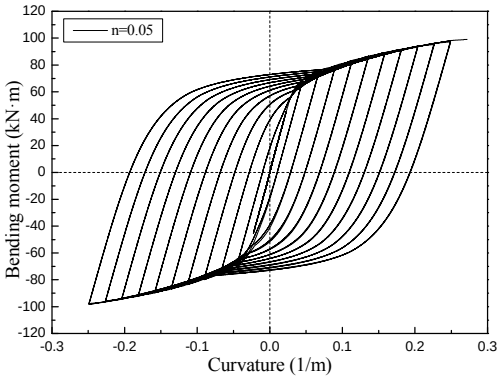

(b) n=0.03

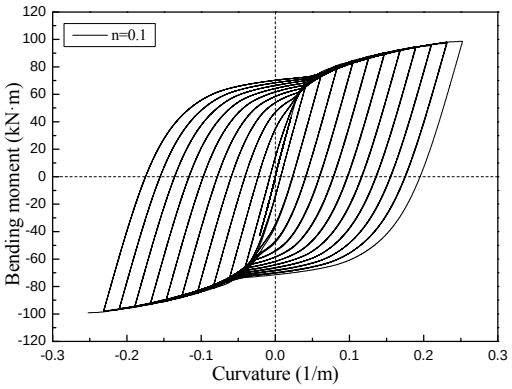

(c) n=0.06

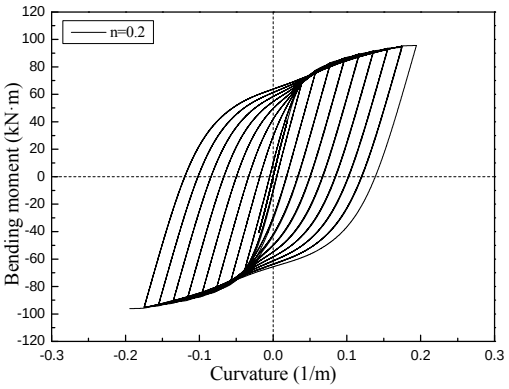

(d) n=0.11

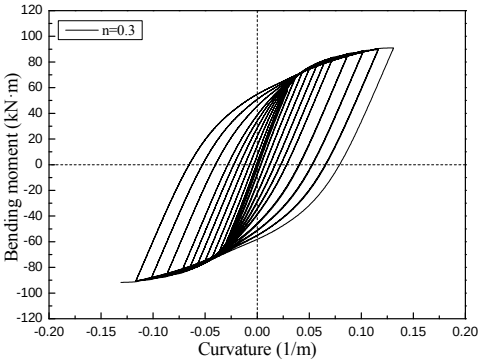

(e) n=0.17

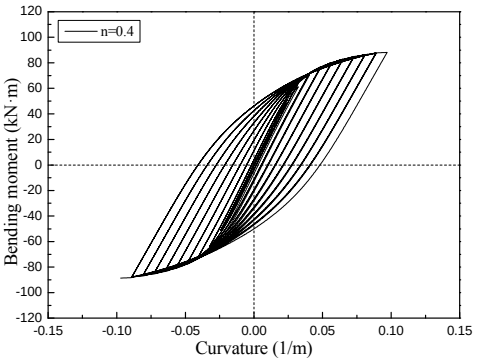

(f) n=0.23

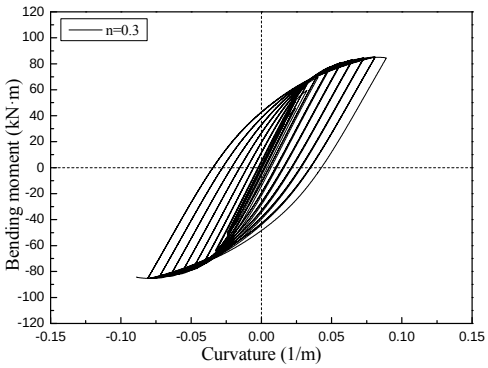

(g) n=0.3

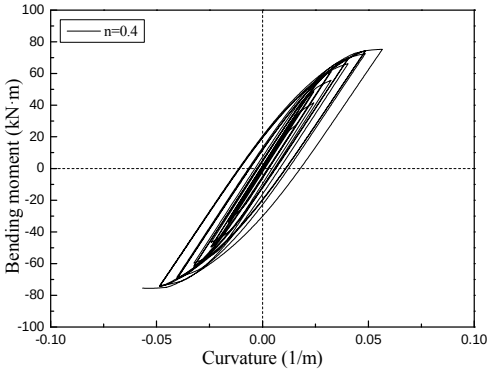

(h) n=0.4

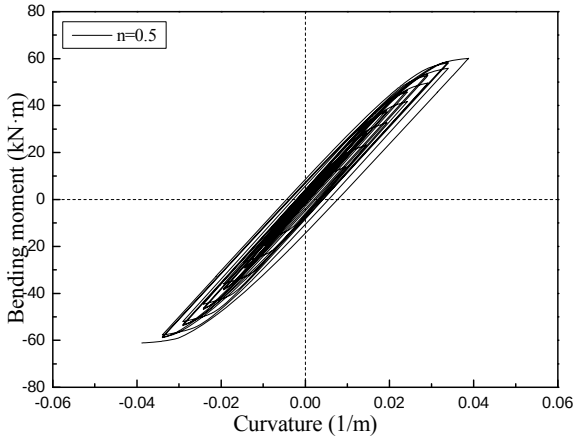

(i) n=0.5

Fig. 3-14 Comparison of hysteretic curves with different axial compression ratios

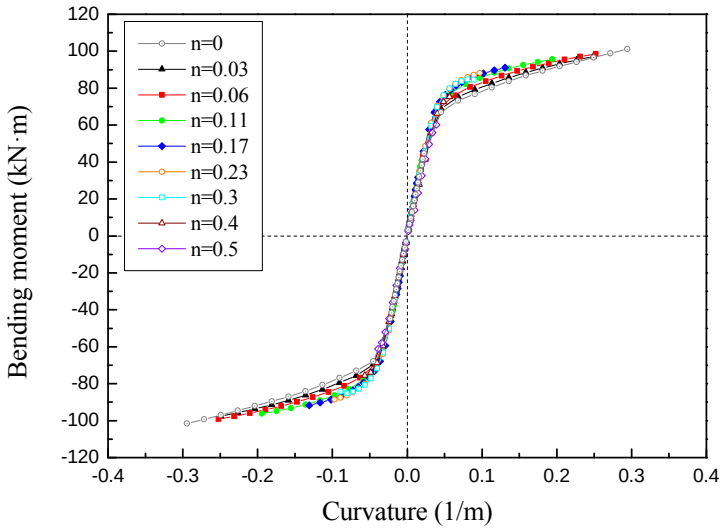

Fig. 3-15 Comparison of skeleton curves with different axial compression ratios

Table 3-3 Main parameters of skeleton curves with different axial compression ratios

Axial compression ratio n	k_a (kN·m2)	φ_{yu} (1/m)	M_{yu} (kN·m)	k_p (kN·m2)	φ_{μ} (1/m)	M_u (kN·m)	μ_{φ}
0	1984	0.081	75.26	126	0.294	105.75	3.63
0.03	2178	0.071	76.04	141	0.250	101.34	3.52
0.06	2237	0.070	76.40	156	0.234	101.99	3.34
0.11	2246	0.056	76.76	186	0.170	98.00	3.04
0.17	2212	0.051	77.21	231	0.100	88.56	1.96
0.23	2192	0.049	77.51	314	0.080	87.29	1.63
0.3	2149	0.046	75.79	406	0.064	82.86	1.39
0.4	2091	0.042	69.06	626	0.050	73.90	1.19
0.5	1947	0.035	58.08	790	0.039	61.10	1.11

Note: k_a was the elasticity stiffness; φ_{yu} was the yielding curvature; M_{yu} was the yielding moment; k_p was the strengthening stiffness; φ_{μ} was the ultimate curvature; μ_{φ} was the curvature ductility coefficient.

In conclusion, the axial compression ratio mainly affected the yield curvature, yield moment, ultimate curvature, ultimate moment, strengthening stiffness and curvature ductility coefficient of the key parameters of the skeleton curve of UCFST columns, but had little influence on the elasticity stiffness of the specimens.

3.5.2 steel ratio

As shown in Table 3-4, the steel ratio parameters were 0.160, 0.196, 0.275 and 0.361, while the other parameters remained unchanged. Fig. 3-16 shows the moment-curvature hysteresis curves of UCFST columns with different steel ratio. Fig. 3-17 shows the moment-curvature skeleton curves of UCFST columns with different steel ratio. The key values of the skeleton curves are listed in Table 3-5.

Table 3-4 Steel ratio model parameters

Length L_s (mm)	1900	Strength of UHPC (MPa)	135
Thickness t (mm)	5、6、8、10		
Steel ratio α	（0.160、0.196、0.275、0.361）	Elasticity modulus of UHPC (MPa)	43000
Outside diameter D (mm)	140	Yield strength of steel tube (MPa)	390
Axial compression ratio n	0.11	Elasticity modulus of steel tube (MPa)	201000

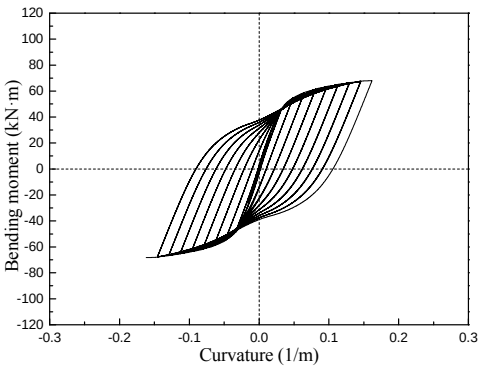

(a) α=0.160

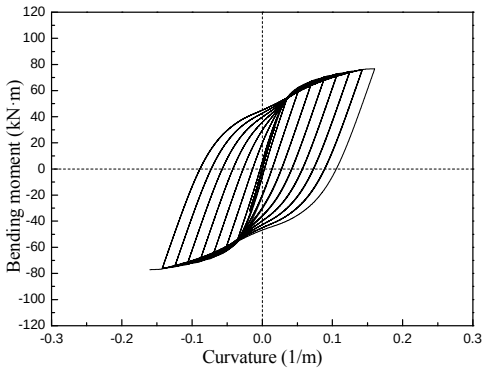

(b) α=0.196

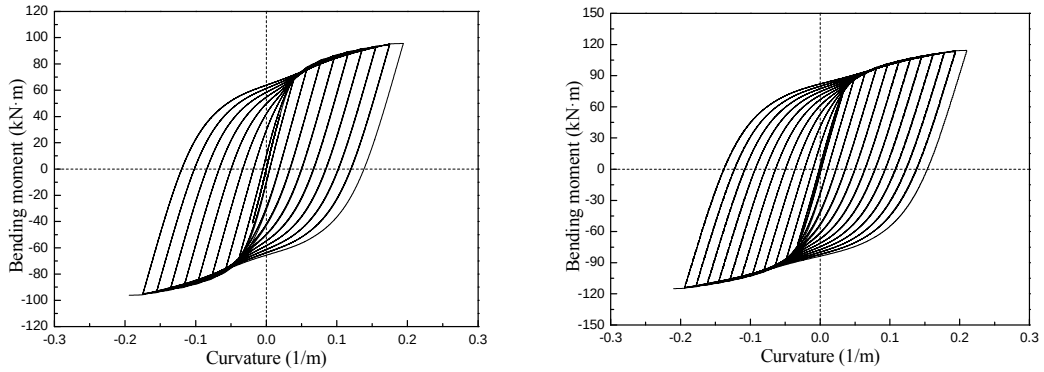

(c) α=0.275 (d) α=0.361

Fig. 3-16 Comparison of hysteretic curves with different steel ratio

In Fig. 3-17, when the steel ratio increased from 0.160 to 0.361, the slope of elastic stage of the skeleton curve of UCFST columns increased, the elasticity stiffness increased greatly by 42.1%; the yield curvature increased by 30.6%; the yield moment increased by 66.0%; the strengthening stiffness increased by 25.5%, the ultimate curvature increased by 66.7%, the ultimate bending moment increased by 79.2%, and the curvature ductility coefficient increased by 30.4%. As shown in Table 3-7, when the steel ratio was 0.16 and 0.196, the curvature ductility coefficient was less than 3, and the seismic behavior of the specimens was not good enough. When the steel ratio was 0.275 and 0.361, the curvature ductility coefficient was greater than 3 and the seismic behavior was good. Therefore, the different steel ratio had a great influence on the hysteretic behavior of UCFST columns.

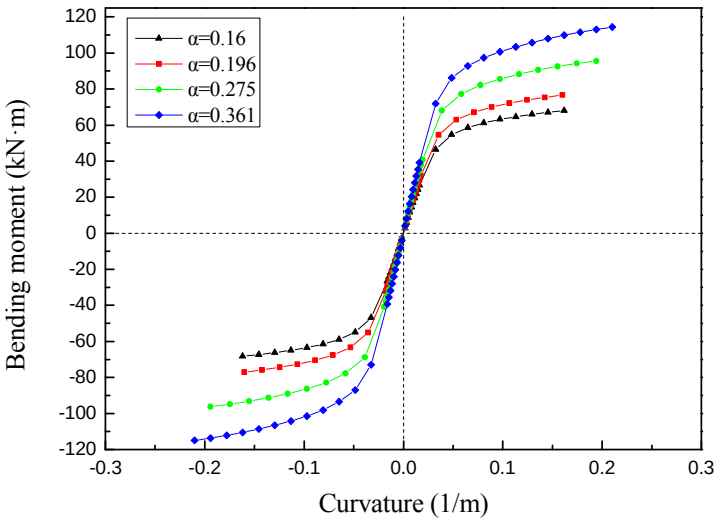

Fig. 3-17 Comparison of skeleton curves with different steel ratio

Table 3-5 Main parameters of skeleton curve with different steel ratio

Steel ratio α	k_a (kN·m2)	φ_{yu} (1/m)	M_{yu} (kN·m)	k_p (kN·m2)	φ_{μ} (1/m)	M_u (kN·m)	μ_{φ}
0.16	1795	0.049	55.31	158	0.12	66.97	2.40
0.196	1951	0.053	62.39	168	0.13	73.38	2.45
0.275	2246	0.056	76.76	186	0.17	98.00	3.04
0.361	2550	0.064	91.83	207	0.20	120.01	3.13

Note: k_a was the elasticity stiffness; φ_{yu} was the yielding curvature; M_{yu} was the yielding moment; k_p was the strengthening stiffness; φ_{μ} was the ultimate curvature; μ_{φ} was the curvature ductility coefficient.

3.5.3 Yield strength of steel tube

In Table 3-6, steel yield strength grades Q235, Q345, Q370, Q390 and Q420 commonly used in bridge structures were selected as steel yield strength analysis. Fig. 3-18 shows the moment-curvature hysteresis curves of UCFST columns with different steel yield strength. Fig. 3-19 shows the moment-curvature skeleton curves of UCFST columns with different steel yield strength. The key values of the skeleton curves are listed in Table 3-7.

In Fig. 3-19, when the steel yield strength changed from Q235 to Q420, the elasticity modulus of steel tube was basically the same and unchanged. The skeleton curves of UCFST columns were basically the same in the elastic stage; the yield curvature of the specimens increased by 22.9%; the yield moment increased by 48.5%; the strengthening stiffness increased by 35.0%; the ultimate moment increased by 42.3% and the curvature ductility coefficient decreased by 18.4%. From Table 3-8, with the increase of steel yield strength, the yield moment and ultimate bending moment of the specimens gradually increased, while the ductility of the specimens decreased to a certain extent, but the curvature ductility coefficient was greater than 3, which shows the seismic behavior of the specimens was good.

When the yield strength of steel tube was Q235, Q345, Q370, Q390 and Q420, the confinement coefficients (Han, 2004) were 0.478, 0.702, 0.753, 0.794 and 0.855, respectively. As can be seen from Fig. 3-19, when the confinement coefficient

increased from 0.478 to 0.702, the yield moment and ultimate moment increased by 35.4% and 27.9%, respectively. When the confinement coefficient increased from 0.702 to 0.855, the yield moment and ultimate moment increased by 9.6% and 11.3%, respectively. In a certain range, the strength of specimens increased with the increase of confinement coefficient, but the increase range decreased gradually.

Table 3-6 Steel yield strength model parameters

Length L_s (mm)	1900	Strength of UHPC (MPa)	135
Thickness t (mm)	8	Elasticity modulus of UHPC (MPa)	43000
Outside diameter D (mm)	140	Yield strength of steel tube (MPa)	Q235、Q345、Q370、Q390、Q420
Axial compression ratio n	0.11	Elasticity modulus of steel tube (MPa)	201000

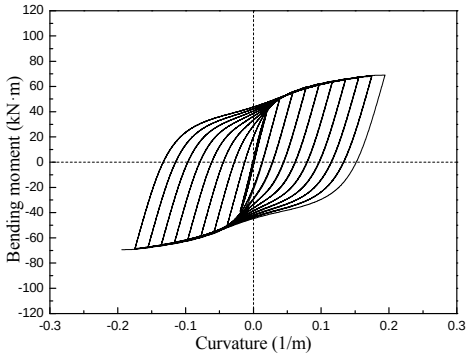

(a)Q235

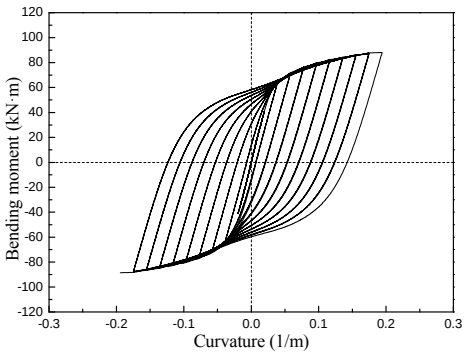

(b)Q345

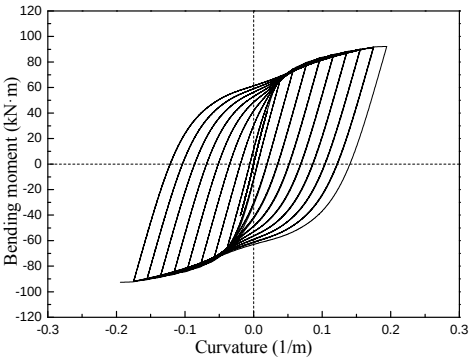

(c)Q370

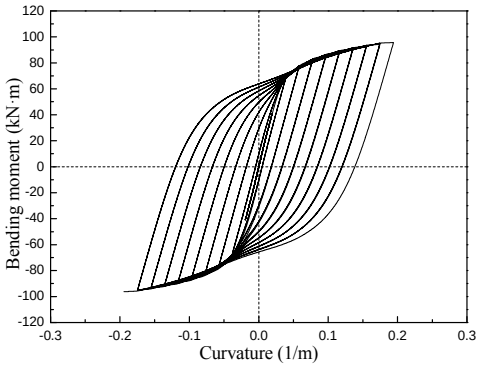

(d)Q390

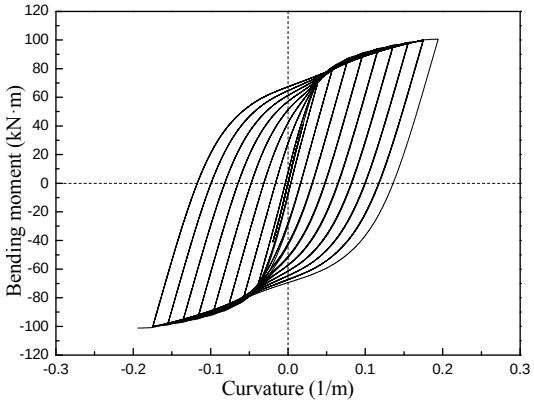

(e)Q420

Fig. 3-18 Comparison of hysteretic curves with different steel yield strength

Table 3-7 Main parameters of skeleton curve with different steel yield strength

Steel yield strength	k_a (kN·m2)	φ_{yu} (1/m)	M_{yu} (kN·m)	k_p (kN·m2)	φ_μ (1/m)	M_u (kN·m)	μ_φ
Q235	2248	0.048	51.98	140	0.17	69.04	3.54
Q345	2251	0.053	70.41	153	0.17	88.31	3.21
Q370	2252	0.054	72.38	173	0.17	92.12	3.15
Q390	2246	0.056	76.40	182	0.17	96.31	3.04
Q420	2247	0.059	77.21	189	0.17	98.25	2.89

Note: k_a was the elasticity stiffness; φ_{yu} was the yielding curvature; M_{yu} was the yielding moment; k_p was the strengthening stiffness; φ_μ was the ultimate curvature; μ_φ was the curvature ductility coefficient.

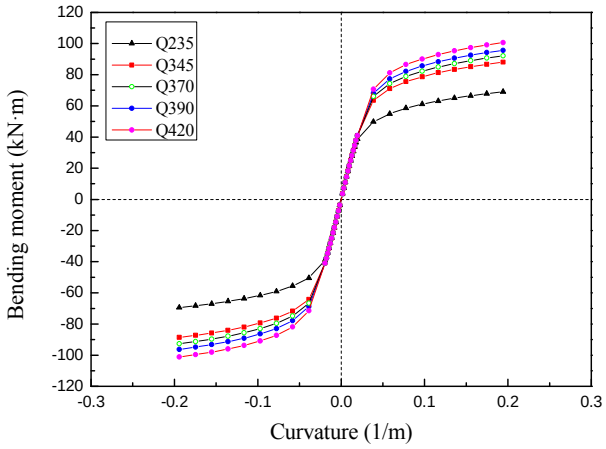

Fig. 3-19 Comparison of skeleton curves with different steel yield strength

In summary, steel yield strength mainly affected the yield curvature, yield moment, ultimate moment, ultimate stiffness and curvature ductility coefficient of the key parameters of UCFST columns skeleton curve, but had little effect on the elasticity stiffness and ultimate curvature.

3.5.4 Core concrete strength

The core concrete grades were C60, C80, C100 and UHPC135, and the other parameters are shown in Table 3-8 in the same way as the standard model. Among them, the axial compressive strength of C60 and C80 concrete was calculated in accordance with the standard "Code for Design of Concrete Structures" (GB 50010-2010). And the axial compressive strength of C100 high-strength concrete was calculated in accordance with Yao et al. (2015). Fig. 3-20 shows the moment-curvature hysteresis curves of UCFST columns with different core concrete strength. Fig. 3-21 shows the moment-curvature skeleton curves of UCFST columns with different core concrete strength. The key values of the skeleton curves are listed in Table 3-9.

In Fig. 3-12, with the increase of concrete strength from C60 to UHPC135, the skeleton curve slope of UCFST columns increased in the elastic stage, which was due to the increase of concrete rigidity, and which the elasticity stiffness of specimens was increased by 7.5%. The yield curvature and curvature ductility coefficient of specimens were basically unchanged. When the core concrete changed from C60 to C80 and C100, the test results were as follows: The yield moment, the strengthening stiffness and the ultimate bending moment of the specimens increased to some extent, but the change range was very small. When the core concrete was replaced by UHPC, the yield moment increased by 9.4%, the strengthening stiffness increases by 30.9%, the ultimate bending moment increased by 9.6%, and the curvature ductility coefficient basically remained unchanged.

Table 3-8 Core concrete strength parameters

Length L_s (mm)	1900	Strength of UHPC (MPa)	C60、C80、C100、UHPC135
Thickness $_t$ (mm)	8	Elasticity modulus of UHPC (MPa)	36000、37000、38000、43000
Outside diameter D (mm)	140	Yield strength of steel tube (MPa)	390
Axial compression ratio n	0.11	Elasticity modulus of steel tube (MPa)	201000

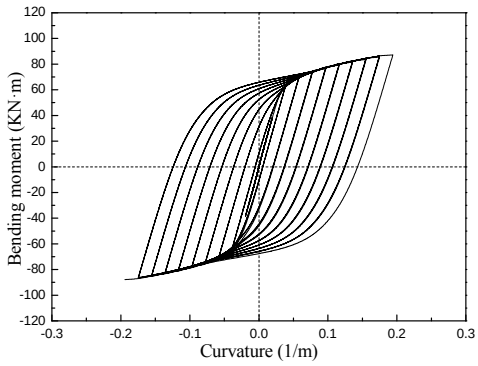

(a) C60

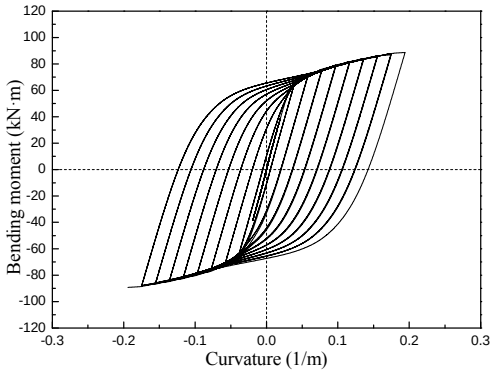

(b) C80

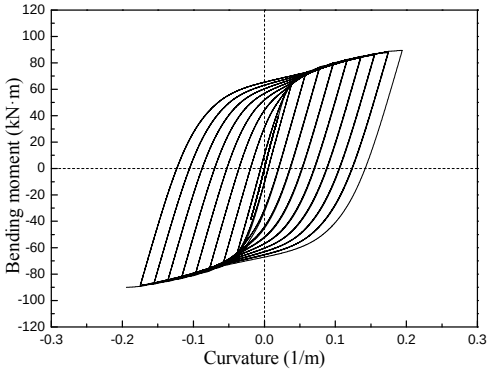

(c) C100

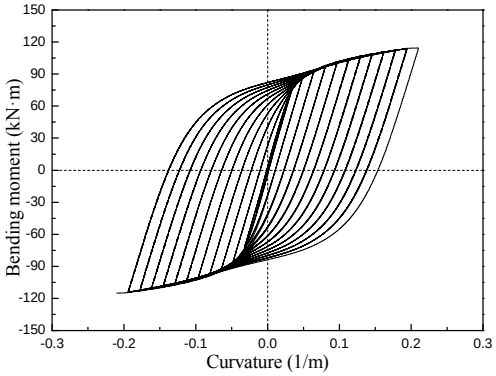

(d) UHPC

Fig. 3-20 Comparisons of hysteretic curves with different core concrete strength

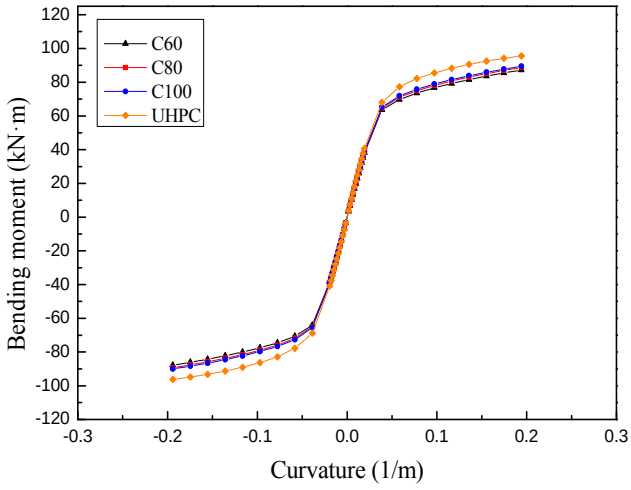

Fig. 3-21 Comparison of skeleton curves with different core concrete strength

Table 3-9 Main parameters of skeleton curve with different core concrete strength

Concrete strength	k_a (kN·m2)	φ_{yu} (1/m)	M_{yu} (kN·m)	k_p (kN·m2)	φ_{μ} (1/m)	M_u (kN·m)	μ_{φ}
C60	2097	0.054	70.14	141	0.17	86.49	3.09
C80	2138	0.055	71.52	143	0.17	87.97	2.98
C100	2160	0.054	72.40	145	0.17	88.74	3.04

UHPC	2246	0.056	76.76	186	0.17	98.00	3.04

Note: k_a was the elasticity stiffness; φ_{yu} was the yielding curvature; M_{yu} was the yielding moment; k_p was the strengthening stiffness; φ_μ was the ultimate curvature; μ_φ was the curvature ductility coefficient.

In summary, the strength of core concrete mainly affected the elasticity stiffness, yield moment, ultimate moment and ultimate stiffness of the key parameters of moment-curvature skeleton curve of UCFST columns, but had little effect on yield curvature, ultimate curvature and ductility coefficient.

3.6 Summary of Chapter 3

(1) Firstly, ABAQUS finite element analysis software was used to analyze the hysteretic behavior of UCFST columns, so as to better understand the working mechanism and failure mode of UCFST columns. Secondly, OpenSEES was used to simulate the UCFST columns. and the accuracy of the finite element model was verified by comparing with the experimental results and ABAQUS simulation results. After verification of the test results, the parameters such as axial compression ratio, steel yield strength and core concrete strength were expanded and supplemented on the basis of the test parameters, and the finite element model was established by OpenSEES to simulate and analyze.

(2) The elasticity stiffness of UCFST columns was mainly affected by the steel ratio and the core concrete strength. Within a certain range, the elasticity stiffness increased in varying degrees with the increase of steel ratio or the core concrete strength. When the axial compression ratio increased from 0 to 0.3, the elasticity stiffness increased, and when the axial compression ratio increased to 0.4 or 0.5, the elasticity stiffness decreased. Analysis of the above results shows that steel ratio had the greatest influence on the elasticity stiffness of UCFST columns.

(3) The yield moment of UCFST columns was affected by such parameters as axial compression ratio, steel ratio, steel yield strength and core concrete strength. Within a certain range, the yield moment of UCFST columns increased firstly and then decreased with the increase of axial compression ratio. With the increase of

steel ratio, steel yield strength or core concrete strength, the yield bending moment of UCFST columns increased in varying degrees.

(4) The curvature at the yield moment of UCFST columns was mainly affected by the axial compression ratio, steel ratio and steel yield strength. Within a certain range, with the increase of the axial compression ratio, the yield curvature of UCFST columns showed a downward trend. With the increase of steel ratio or steel yield strength, the yield curvature of UCFST columns decreased in different extent.

(5) The ultimate bending moment of UCFST columns was affected by such parameters as axial compression ratio, steel ratio, steel yield strength and core concrete strength. Within a certain range, with the increase of axial compression ratio, the ultimate bending moment of UCFST columns tended to decrease, but the range was very small. With the increase of steel ratio, steel yield strength or core concrete strength, the ultimate bending moment of UCFST columns increased in varying degrees, in which steel ratio had the greatest impact on the ultimate bending moment, followed by steel yield strength, and then the core concrete strength.

(6) The curvature of UCFST columns was mainly affected by the parameters such as axial compression ratio and steel ratio. Within a certain range, with the increase of axial compression ratio, the ultimate curvature of UCFST columns showed a downward trend; with the increase of steel ratio, the ultimate curvature of UCFST columns increased slightly.

(7) The curvature ductility coefficient of UCFST columns was mainly affected by the parameters such as axial compression ratio, steel ratio and steel yield strength. Within a certain range, the curvature ductility coefficient of UCFST columns decreased significantly with the increase of axial compression ratio while other parameters remained unchanged. With the increase of steel ratio or steel yield strength, the curvature ductility coefficient of UCFST columns increased in varying degrees.

Chapter 4

Moment-Curvature Skeleton Curve Model of UCFST Columns

The moment-curvature skeleton curve of UCFST columns is one of the preconditions for elastic-plastic seismic analysis of CFST structures. The characteristic values of the curve include elastic bending stiffness, yield bending moment, yield curvature and strengthening stiffness. Although the moment-curvature curves of UCFST columns can be calculated accurately by using finite element software, it is not easy to be used in engineering practice, so it is necessary to establish a simplified model of moment-curvature skeleton curves of UCFST columns. Therefore, based on the pseudo-static test of UCFST columns in Chapter 2 and the finite element parameter analysis in Chapter 3, and referring to the calculation method of characteristic points of skeleton curves of normal CFST members, the simplified calculation formula of eigenvalues in skeleton curves in this chapter was deduced.

4.1 Bending moment-curvature skeleton curve calculation model of UCFST columns

Han (2004) considered the influence of axial compression ratio, steel ratio, steel yield strength and core concrete strength on the skeleton curve of CFST members, carried out a large number of experiments and finite element analysis, thus proposed the moment-curvature skeleton curve model of CFST members, and deduced the simplified calculation formula of each characteristic point of skeleton curve. Therefore, the research on the moment-curvature skeleton curve model of UCFST

columns can refer to the research on that of normal CFST members.

The research object of this paper was the UCFST columns, and the parameters such as axial compression ratio, steel ratio and steel yield strength had great influence on the hysteretic behavior of UCFST columns. And the influence of concrete strength was not considered in this paper. In order to facilitate calculation, the following basic assumptions were adopted:

(1) The member was always flat in the process of deformation.

(2) There was no relative slip between steel tube and concrete.

(3) The two ends of the component were articulated and the deflection curve was a sinusoidal half-wave curve.

From the analysis results in Chapter 2 and Chapter 3, it can be seen that the moment-curvature skeleton curve of UCFST columns was approximately a three-fold line, so the skeleton curve model can be composed of three-fold lines of elastic phase, elastic-plastic phase and strengthening phase, as shown in Fig. 4-1. Point A was the initial yield point of UCFST column, its corresponding bending moment value was M_{ya}, Point B was the complete yield point of the whole section of the specimen, its corresponding bending moment value was M_{yu}, Point C was the failure point of the specimen, and its corresponding bending moment value was M_u. In this chapter, the following simplified formulas for calculating eigenvalues were derived:

1) Elastic phase stiffness;

2) Bending moment M_{ya} and curvature φ_{ya} at point A of initial yield point;

2) Load M_{yu} and curvature φ_{yu} at point B of yield point of full section;

3) The ultimate moment M_u and curvature φ_u at point C of the final failure point.

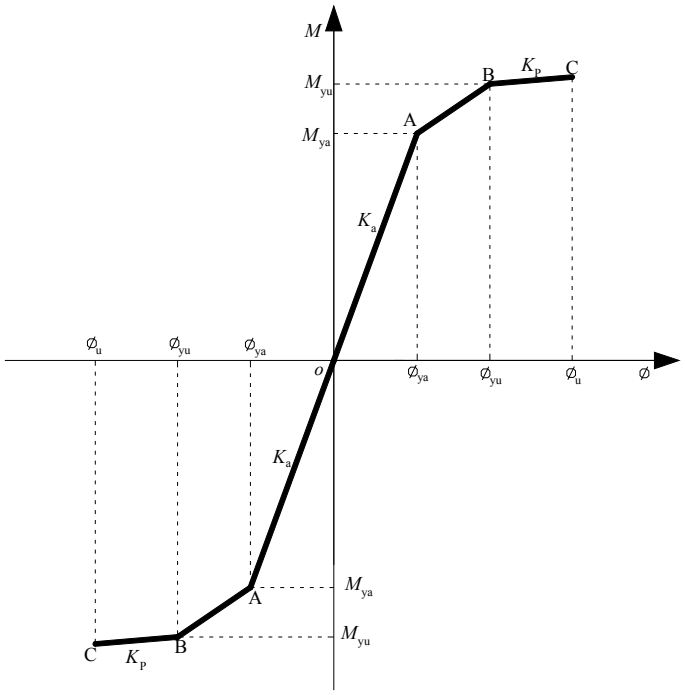

Fig. 4-1 Schematic diagram of bending moment-curvature skeleton curve

4.2 Bending stiffness in the elastic stage

4.2.1 Stiffness superposition calculation method

Nowadays, the research on bending stiffness of CFST members is mainly based on superposition theory and integral theory (GB 50936-2014). The definition of bending stiffness of CFST members is mostly based on superposition theory in national codes, which takes into account the contribution of steel tube and concrete to bending stiffness, and then takes a certain reduction coefficient for bending stiffness of concrete. However, the values of reduction coefficients are different in different specifications. The basic bending stiffness formula of superposition theory is shown as follows:

$$K = E_s \cdot I_s + m \cdot E_c \cdot I_c \tag{4-1}$$

where E_s and I_s are the elasticity modulus and the inertia moment of steel tube; E_c and I_c are the elasticity modulus and inertia moment of concrete, m is the bending rigidity reduction coefficient of concrete.

In this paper, the calculating formulas of bending stiffness of CFST columns in four

common codes were compared with the measured values to determine the calculating formulas of bending stiffness of UCFST columns in the elastic stage in this paper. Table 4.1 shows the formulas for calculating bending stiffness of the codes, where E_s and E_c adopted the measured values of property tests. Fig. 4-2 is a comparison between the results of finite element calculation and those of the four codes. It can be seen from the figure that there was a big gap between the results of the formula considering the reduction of bending stiffness of concrete in the code and those of the finite element method, both of which were smaller than those of the finite element method. Compared with other formulas, the results calculated by BS5400 (1979) formula were closer to the results of finite element analysis.

Table 4-1 Different specifications of bending stiffness

Specification	Bending stiffness calculation formula
ACI (2005)	$K = E_S \cdot I_S + 0.2 \cdot E_C \cdot I_C$
EC4 (2004)	$K = E_S \cdot I_S + 0.6 \cdot E_C \cdot I_C$
BS5400(1979)	$K = E_S \cdot I_S + E_C \cdot I_C$
AISC-LRFD	$K = E_S \cdot I_S + 0.8 \cdot E_C \cdot I_C$

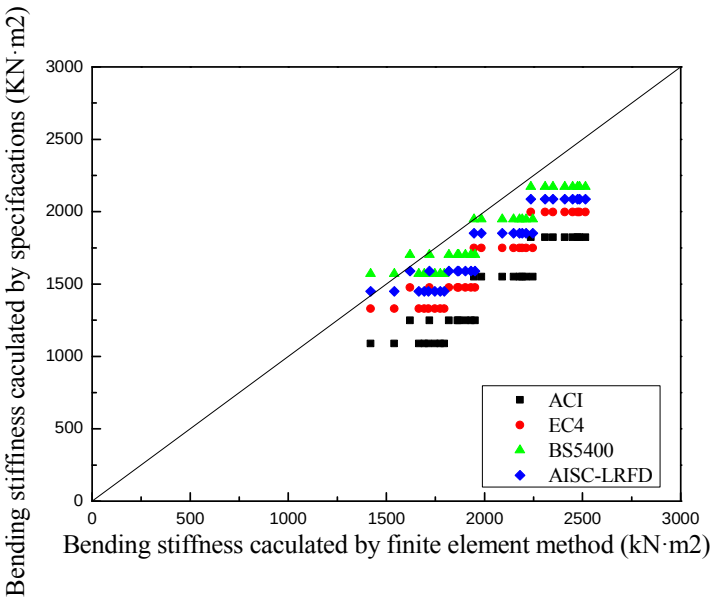

Fig. 4-2 Bending stiffness comparison calculated by finite element method and specifications

According to the parameter analysis in Chapter 3, the main influencing factors of bending stiffness in elastic stage were axial compression ratio and steel ratio. From Fig. 4.1, it can be seen that the bending stiffness increased with the increase of steel ratio, which was mainly realized by the change of steel ratio, and was reflected in the inertia moment I_s of steel tube. With the increase of the axial compression ratio, the bending stiffness increased firstly and then decreased, but the bending stiffness changed little when the axial compression ratio was in a certain range. Therefore, considering the influence of steel ratio and axial compression ratio on bending rigidity, BS5400 (1979) formula without considering the reduction of bending rigidity of concrete was modified.

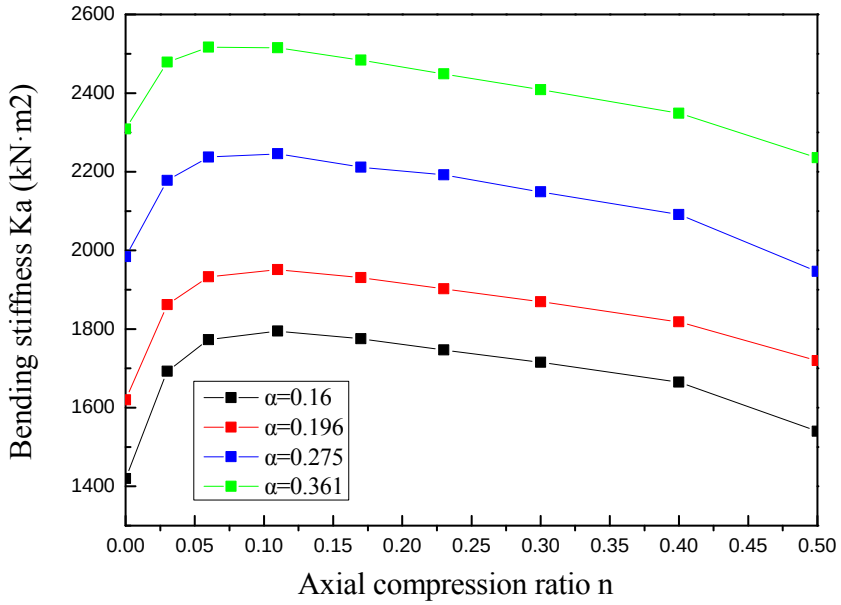

Fig. 4-3 Effect of different axial compression ratios and steel ratio on bending stiffness

Fig. 4-4 shows the relationship between the bending stiffness of each specimen and the ratio of BS5400 (1979) formula and the axial compression ratio. It can be seen from the figure that when the axial compression ratio was greater than 0, the influence of steel ratio on the ratio was very small. With the increase of the axial compression ratio, the ratio of the bending stiffness of each specimen to the calculated results of the formula increased firstly and then decreased. From the regression analysis of the data in the figure, Eq. (4-2) can be obtained:

$$K_a = a \cdot (E_S \cdot I_S + E_C \cdot I_C) \tag{4-2}$$

where $a = \begin{cases} 1 + \frac{56}{3} \cdot n & 0 \le n \le 0.06 \\ 1 + \frac{5}{22} \cdot (0.5 - n) & 0.06 < n \le 0.5 \end{cases}$

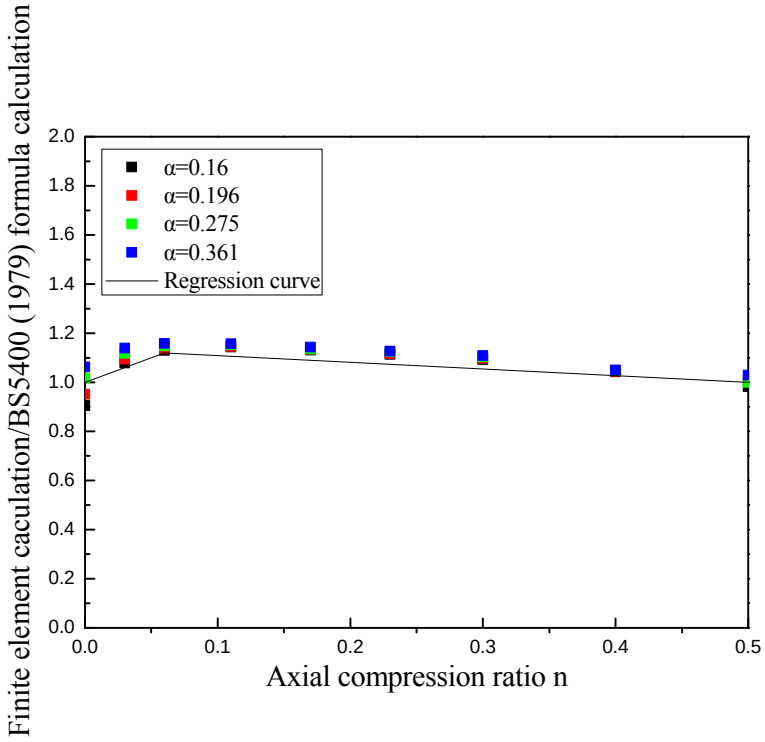

Fig.4-4 Relationship between finite element bending stiffness/BS5400 (1979) formula calculation and axial compression ratio

4.2.2 Accuracy verification

The bending stiffness of UCFST columns in this paper was calculated according to Eq. (4-2). The comparison results of bending rigidity calculated from Eq. (4-2) with experimental and simulated results are listed in Table 4-2. The extended parameters of finite element in Chapter 3 were calculated with the Eq. (4-2), as shown in Fig. 4-5. From the table, we can see that the bending stiffness calculated by the formula was slightly lower than the experimental value. Compared with the experimental value and the finite element value, the error of the formula was within 11%., which showed that it was generally consistent and safe.

Table 4-2 Comparison of bending stiffness calculated from Eq. (4-2) with experimental and simulated results

Specimen number	Calculated by Eq. (4-2)	Test result	Error (%)	Simulated result	Error (%)
GU-T8-N03	2099	2147	-2.2	2178	-3.6
GU-T8-N06	2248	2185	2.9	2237	0.5
GU-T8-N11	2215	2212	0.1	2246	-1.4
GU-T8-N17	2175	2274	-4.4	2212	-1.7
GU-T8-N23	2134	2162	-1.3	2192	-2.6
GU-T5-N11	1691	1809	-6.5	1795	-5.8
GU-T6-N11	1934	2049	-10.5	1951	-0.9
GU-T10-N11	2340	2514	-6.9	2515	-7.0

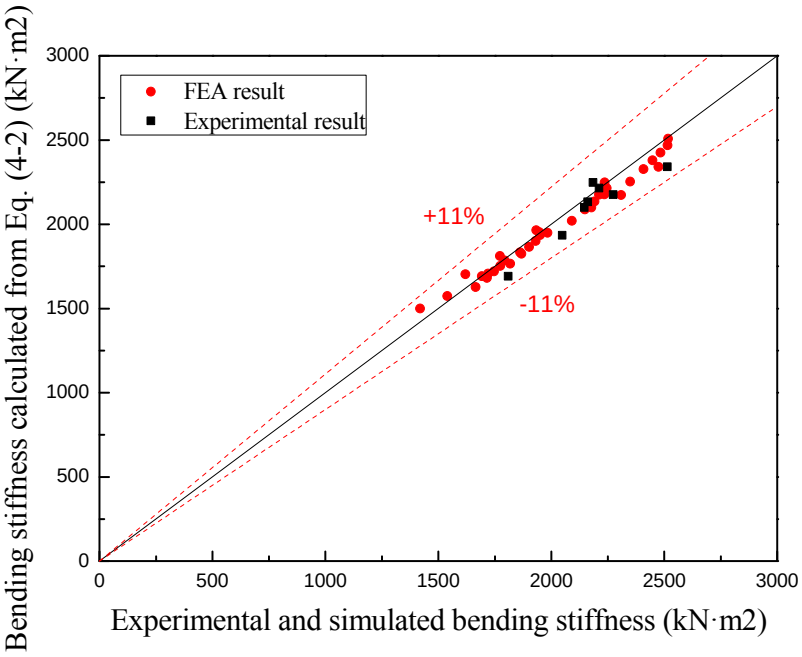

Fig. 4-5 Comparison of bending stiffness calculated from Eq. (4-2) with experimental and simulated results

4.3 Complete and initial yield moment

4.3.1 Method for calculating complete yield moment

In this paper, the moment corresponding to the yield of the most critical entire cross section of UCFST columns was taken as the complete yield moment M_{yu}. According to the calculation formula of the yield moment of CFST structures (Han, 2004), the relationship between axial force and bending moment could be best represented by a

linear or a quadratic function depending on the axial compression ratio, as shown in Eq. (4-3):

$$\begin{cases} \dfrac{N}{N_u}+a\cdot\left(\dfrac{M}{M_{yu}}\right)=1 & \left(N/N_u\geq 2\eta_0\right) \\ -b\cdot\left(\dfrac{N}{N_u}\right)^2-c\cdot\left(\dfrac{N}{N_u}\right)+\left(\dfrac{M}{M_{yu}}\right)=1 & \left(N/N_u<2\eta_0\right) \end{cases} \tag{4-3}$$

$$N_u=f_{ck}\cdot A_{sc}(1.14+1.02\xi) \tag{4-4}$$

$$M_u=\gamma_m\cdot W_{scm}\cdot f_{scy} \tag{4-5}$$

where $a=1-2\eta_0$, $b=\dfrac{1-\zeta_0}{\eta_0^{\,2}}$, $c=\dfrac{2\cdot(\zeta_0-1)}{\eta_0}$, $\zeta_0=0.18\xi^{-1.15}+1$;

$\eta_0=\begin{cases}0.5-0.245\cdot\xi & \left(\xi\leq 0.4\right)\\ 0.1+0.14\cdot\xi^{-1.3} & \left(\xi\geq 0.4\right)\end{cases}$;

N_u is the compressive strength bearing capacity; M_{yu} is the ultimate bending capacity;

W_{scm} is CFST column bending modulus; γ_m is sectional bending resistance coefficient.

Eq. (4-3) shows that the strength bearing capacity N_u and bending ultimate bearing capacity M_{yu} obtained before the formula substituted for calculation. Therefore, the above formulas of strength bearing capacity and bending ultimate bearing capacity of CFST columns was firstly verified for the application to UCFST columns.

According to Section 3.2.2 of Chapter 3, the above Eq. (4-5) were applicable to UCFST columns in this paper. The ultimate bending moment of UCFST columns was related to steel yield strength and steel ratio. Therefore, the finite element model was established with steel yield strength (Q235, Q345, Q390) and steel ratio (0.16, 0.196, 0.275, 0.361) as parameters, and the ultimate bending capacity with different parameters was compared with the calculated value of formula without considering the effect of axial force. The results are shown in Fig. 4-6. From Fig. 4-6, it can be seen that the results of UCFST columns calculated by finite element model were basically consistent with those obtained by using the formula for calculating the bending capacity of CFST columns. Therefore, Eq. (4-5) for calculating the bending

moment of CFST columns can be applied to UCFST columns.

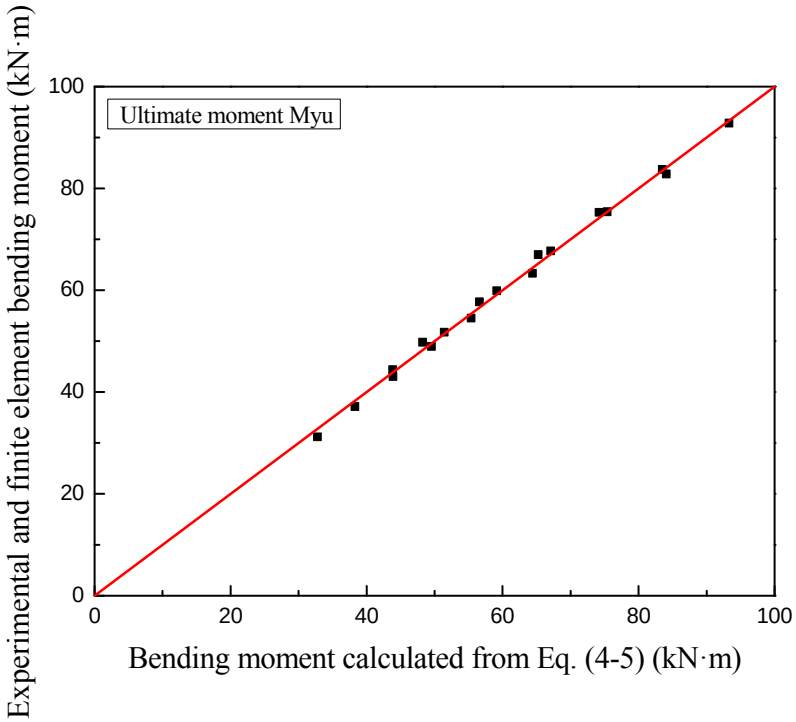

Fig. 4-6 Comparisons ultimate bending moment between Eq. (4-5) calculated results and the finite element results

According to the analysis of the parameters in Chapter 3, the main parameters affecting the yield moment of UCFST columns were steel yield strength, steel ratio and axial compression ratio. Considering the number of finite element models and the size of the influence, comprehensively, the ultimate bending capacity of UCFST columns with steel ratio (steel tube thickness 5 mm, 6 mm, 7 mm, 8 mm, 10 mm) and axial compression ratio (0, 0.03, 0.06, 0.11, 0.17, 0.23, 0.3, 0.4, 0.5) as the main parameters were calculated by Eq. (4-3), and compared with the results of finite element analysis, as shown in Fig. 4-7. As can be seen from the figure, the results of Eq. (4-3) were mostly smaller than those of finite element method, and the larger the difference was with the increase of yield moment. Therefore, it can be explained that the Eq. (4-3) for calculating the axial force and bending moment of CFST specimens was not applicable to the UCFST specimens, and the formula for calculating the axial force and bending moment of the UCFST specimens needed to be redefined.

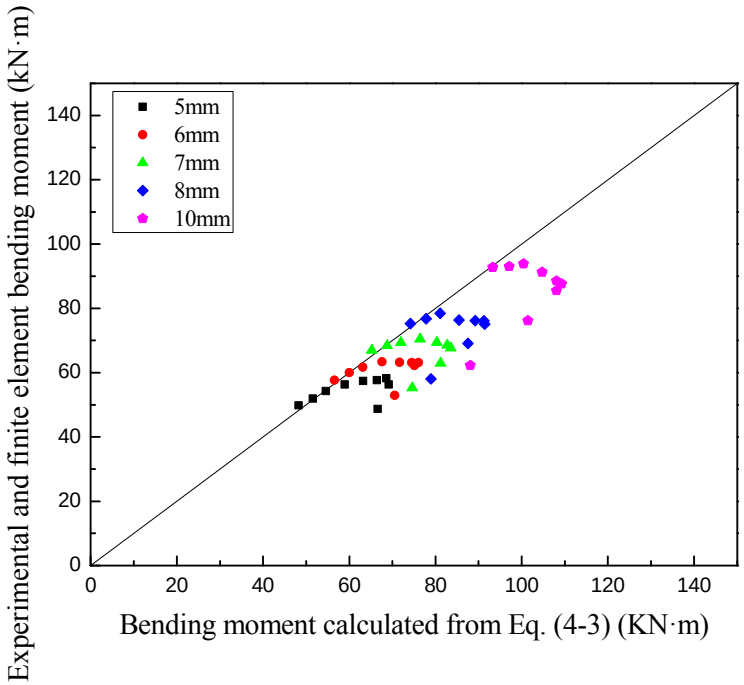

Fig. 4-7 Comparisons bending moment between Eq. (4-3) calculated results and the finite element results

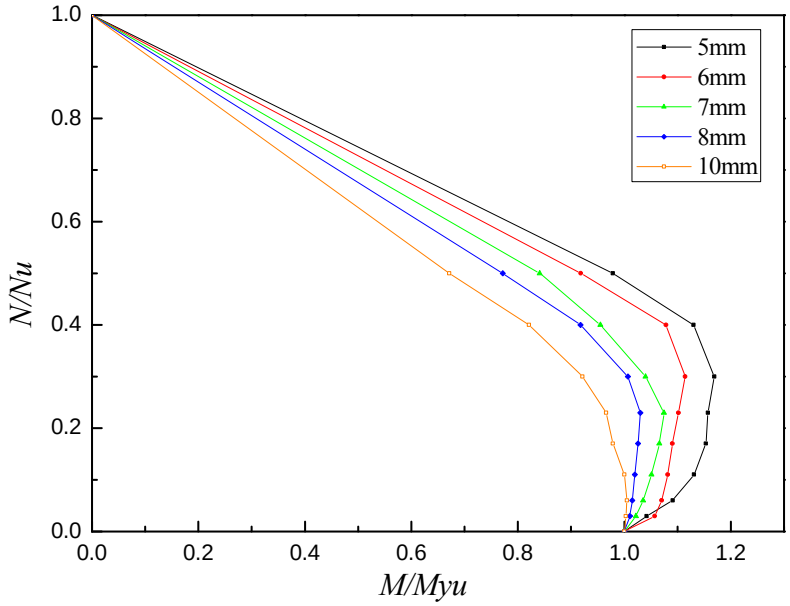

Fig. 4-8 N/Nu-M/M_{yu} relationship curves

Five groups of steel ratio (steel tube thickness 5 mm, 6 mm, 7 mm, 8 mm, 10 mm) and nine groups of axial compression ratios (0, 0.03, 0.06, 0.11, 0.17, 0.23, 0.3, 0.4, 0.5) were orthogonal to each other and 45 UCFST columns finite element model groups of different parameters were calculated. Referring to the axial force-moment

relationship of CFST columns, taking N/N_u as the ordinate and M/M_{yu} as the abscissa, the axial force-moment relationship of the 45 groups is drawn in Fig. 4-8. It can be seen from the figure that the area covered by the curve increased with the increase of steel ratio, but the trend of the curve was basically the same, approximating the double-fold line. Referring to the axial force-moment curve of CFST columns described in reference (Zhong, 2006), the relationship between axial force and bending moment of UCFST columns was expressed by double folded lines, as shown in Fig. 4-9.

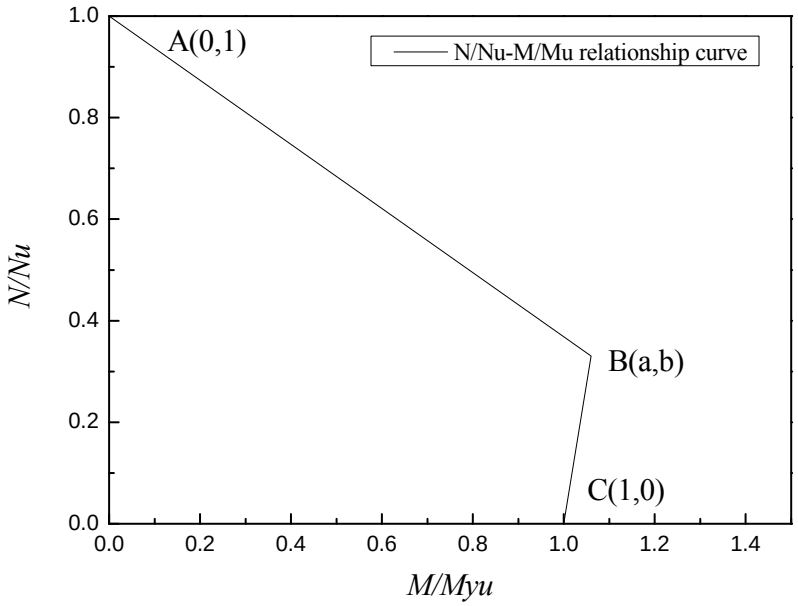

Fig. 4-9 N/N_u-M/M_{yu} relationship curve of UCFST columns

Based on the regression analysis of the results of the 45 finite element models mentioned above, the axial force-moment curve of UCFST columns can be expressed as Eq. (4-6), in which the intersection coordinates B (a, b) and coefficients c and d were respectively expressed by confinement coefficient ξ.

$$\begin{cases} \dfrac{N}{N_u} + c \cdot \left(\dfrac{M}{M_{yu}} \right) = 1 & \left(N / N_u \geq b \right) \\ d \cdot \left(\dfrac{N}{N_u} \right) + \left(\dfrac{M}{M_{yu}} \right) = 1 & \left(N / N_u < b \right) \end{cases} \tag{4-6}$$

where $a = 0.354 + 0.396\xi$, $b = -1.203 + 1.272\xi$,

$c = 1.403 - 0.426\xi$, $d = 0.418 - 0.150\xi$

4.3.2 Method for calculating initial yield moment

The relationship between the initial yield moment M_{ya} (i.e. the corresponding A-point ordinate value in the moment-curvature trilinear model of UCFST columns in Fig. 4-10) and the complete yield moment M_{yu} was obtained by statistical analysis of the experimental and finite element results in this paper. The expression is as follows:

$$M_{ya}=0.6M_{yu} \tag{4-7}$$

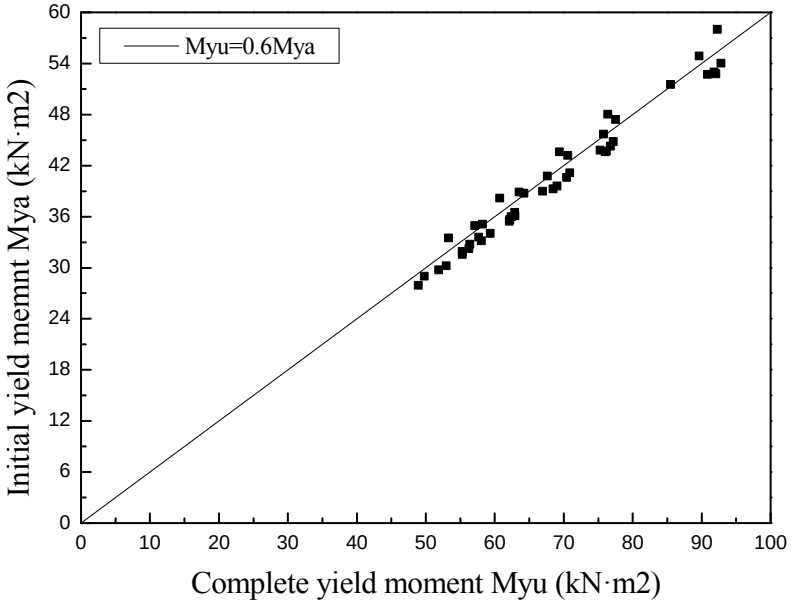

Fig. 4-10 Relationship between the initial yield moment M_{ya} and the complete yield moment M_{yu}

4.3.3 Accuracy verification

The complete yield moments and initial yield moments calculated by Eq. (4-6) and Eq. (4-7) were compared with the pseudo-static test and finite element results. The comparison results are listed in Table 4-3. And by using the formulas mentioned above, the finite element model results with different expansion parameters in Chapter 3 were calculated. All the results are expressed in Fig. 4-11 and Fig. 4-12.

From Table 4-3, it can be seen that the errors of Eq. (4-6) and Eq. (4-7) were within 9% compared with the results of pseudo-static test. From Fig. 4-10, it can be seen that

the calculation results of the formulas were mostly slightly smaller than those of the finite element and test results. It was safer to use the formula to calculate the bearing capacity of UCFST columns. Therefore, the above Eq. (4-6) and Eq. (4-7) can be applied to the calculation of the complete yield moment and initial yield moment of UCFST columns.

Table 4-3 Yield moment comparisons between the formula calculated results and the experimental and finite element results (kN·m)

Specimen number	Complete yield moment		Error	Initial yield moment		Error
	Experimental result	Calculated result	(%)	Experimental result	Calculated result	(%)
GU-T8-N03	77.88	74.62	-4.2	45.64	44.77	-1.9
GU-T8-N06	78.13	75.05	-3.9	47.23	45.03	-4.7
GU-T8-N11	78.38	75.77	-3.3	43.21	45.46	5.2
GU-T8-N17	80.42	76.63	-4.7	46.19	45.98	-0.5
GU-T8-N23	79.88	77.49	-3.0	46.87	46.49	-0.8
GU-T5-N11	56.12	51.52	-8.2	28.79	30.91	7.4
GU-T6-N11	64.34	59.6	-7.4	33.26	35.76	7.5
GU-T10-N11	91.8	92.04	0.3	55.78	55.22	-1.0

Note: Error = (Formula calculated value-test or finite element value)/test or finite element value ×100%.

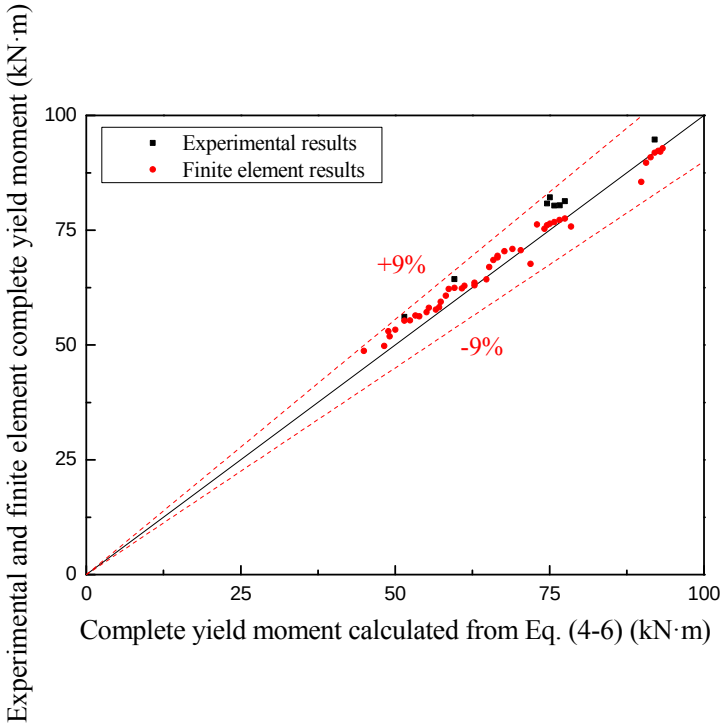

Fig. 4-11 Complete yield moment comparisons between results calculated by Eq. (4-6) and

the experimental and finite element results

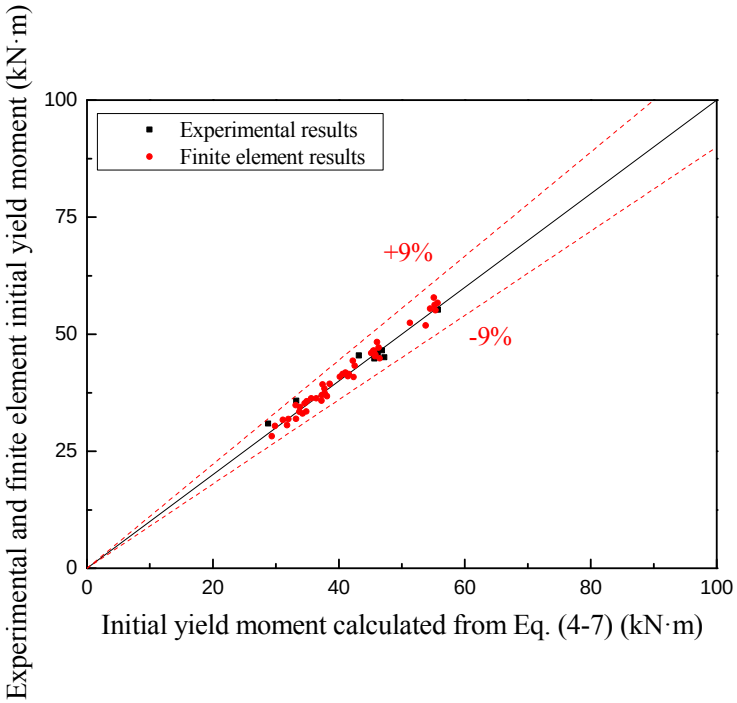

Fig. 4-12 Initial yield moment comparisons between results calculated by Eq. (4-7) and the experimental and finite element results

4.4 Complete yield curvature and initial yield curvature

4.4.1 Method for calculating yield curvature

Firstly, the initial yield curvature was calculated. In Sections 4.2 and 4.3 of this chapter, formulas for calculating the initial yield moment and the stiffness of the elastic phase have been obtained. Therefore, the initial yield curvature can be calculated according to the following formula:

$$\phi_{ya} = \frac{M_{ya}}{K_a} \tag{4-8}$$

Secondly, according to the test results in Chapter 2 and the parameters analysis in Chapter 3, it can be seen that the yield curvature of UCFST columns moment-curvature skeleton curve was mainly related to the axial compression ratio and steel ratio. Therefore, the yield curvature obtained by the above finite element model was statistically analyzed, and the results are shown in Fig. 4-13 with $\varphi_{yu}/\varphi_{ya}$ as the ordinate and n as the abscissa. Then the regression analysis was carried out

according to the results of the finite element method, and the regression curve was obtained as shown by the solid line in Fig. 4-13. The expression is as follows:

$$\frac{\phi_{yu}}{\phi_{ya}} = 3.473 - 6.152 \cdot n + 5.912n^2 \tag{4-9}$$

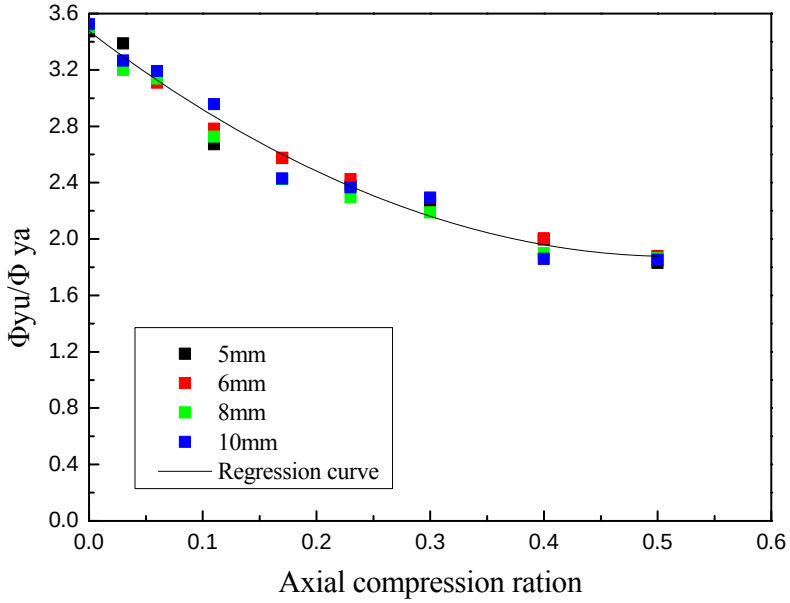

Fig. 4-13 Relationship curve of $\varphi_{yu}/\varphi_{ya}$ and n

4.4.2 Accuracy verification

The initial yield curvature and complete yield curvature calculated by Eq. (4-8) were compared with the quasi-static test results, and the results are listed in Table 4-4. The finite element model results with different extended parameters in Chapter 3 were calculated by using the above formulas, and all the results are shown in Fig. 4-14 and Fig. 4-15.

From Table 4-4, it can be seen that the error of the formula calculation results was within 8% compared with the experimental results, and the error of the formula calculation results was within 9% compared with the finite element calculation results, which showed that the formula calculation results were in good agreement with the finite element and experimental results. Therefore, the above Eq. (4-9) can be applied to the calculation of yield curvature of UCFST columns.

Table 4-4 Yield curvature comparisons between the formula calculated results and the experimental and finite element results

Specimen number	Complete yield curvature		Error (%)	Initial yield curvature		Error (%)
	Experimental result	Calculated result		Experimental result	Calculated result	
GU-T8-N03	0.07	0.072	2.9	0.021	0.021	0.3
GU-T8-N06	0.066	0.07	6.1	0.022	0.020	-7.3
GU-T8-N11	0.056	0.059	4.8	0.020	0.021	5.1
GU-T8-N17	0.056	0.054	-3.6	0.020	0.021	4.1
GU-T8-N23	0.052	0.05	-3.8	0.022	0.022	0.5
GU-T5-N11	0.05	0.053	6.0	0.016	0.017	7.4
GU-T6-N11	0.051	0.055	7.8	0.016	0.017	3.5
GU-T10-N11	0.064	0.068	6.3	0.022	0.024	6.4

Note: Error = (Formula calculated value-test or finite element value)/test or finite element value ×100%.

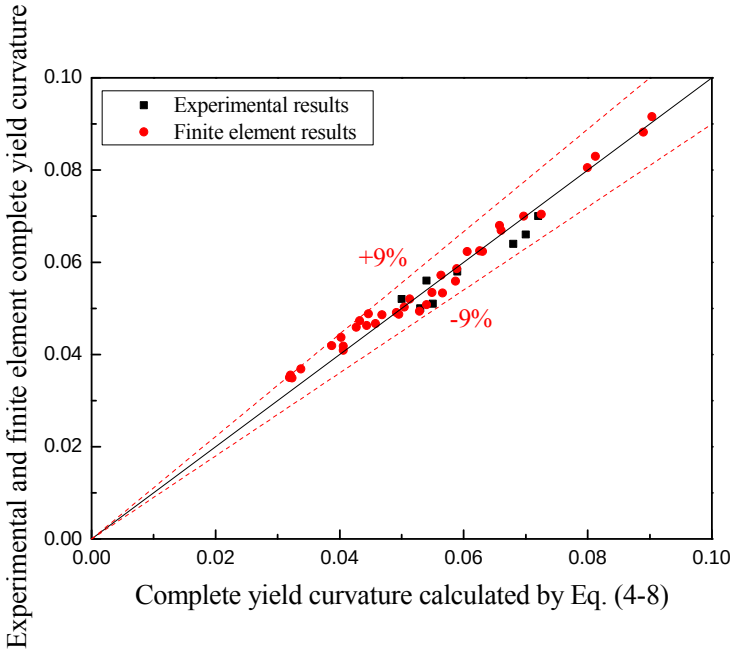

Fig. 4-14 Complete yield curvature comparisons between results calculated by Eq. (4-8) and the experimental and finite element results

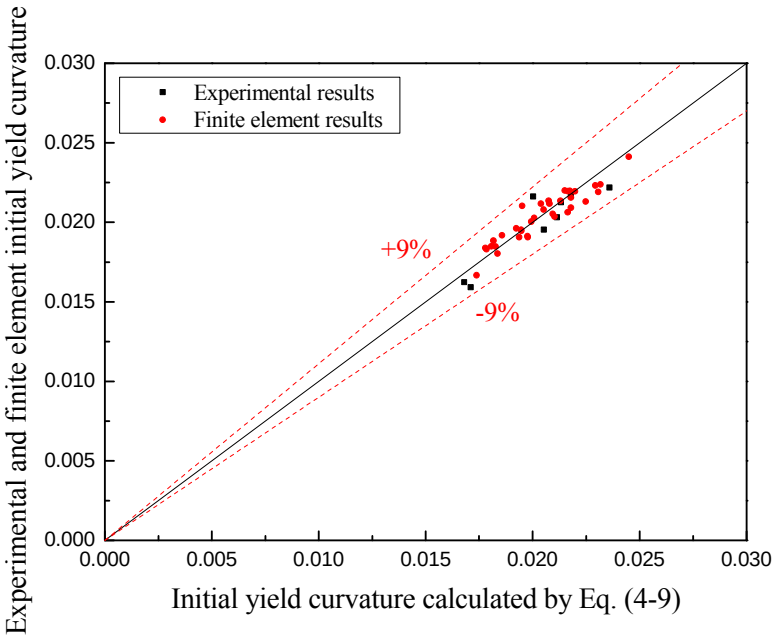

Fig. 4-15 Initial yield curvature comparisons between results calculated by Eq. (4-9) and the experimental and finite element results

4.5 Bending rigidity in the strengthening phase

4.5.1 Calculation method of strengthening stiffness

The slope of the connection line between point B and point C on the skeleton curve of UCFST columns on Fig. 4-1 was defined as the bending rigidity k_p, which was the slope between the yield moment point on the skeleton curve and the failure moment point. From references (Han, 2004; Zhong, 2006), it can be seen that the stiffness of the strengthening phase can be expressed by Eq. (4-10), and α_p is the strengthening coefficient. According to the parameter analysis in Chapter 3, the strengthening stiffness of UCFST columns moment-curvature skeleton curve was mainly related to the axial compression ratio and steel ratio. Therefore, referring to references (Han, 2004; Zhong, 2006), the strengthening stiffness obtained by the above finite element model was statistically analyzed, and the results are shown in Fig. 4-16 with $k_p/k_a(\alpha_p)$ as the ordinate and axial compression ratio n as the abscissa. Regression analysis was carried out and the regression curve was obtained as shown by the solid line in Fig. 4-16. The expression is as follows:

$$K_p = \alpha_p \cdot K_a \tag{4-10}$$

where $\alpha_p = 0.067 + 0.066n + 1.207n^2$.

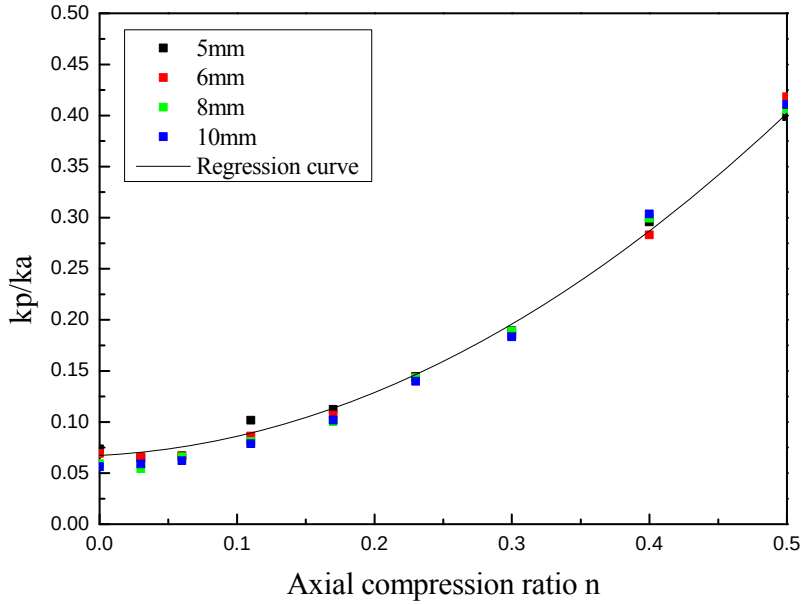

Fig. 4-16 Relationship curve between 38T $k_p/k_a(\alpha_p)$ and n

4.5.2 Accuracy verification

Eq. (4-10) was used to calculate the stiffness of the strengthening phase of the above-mentioned finite element model, and the calculated results were compared with the experimental results and the finite element results in Table 4-5 and Fig. 4-17. From Table 4-5, it can be seen that the error of the formula calculation results was within 10% compared with the experimental results, and the error of the formula calculation results was within 9% compared with the finite element calculation results, which showed that the formula calculation results were in good agreement with the finite element and experimental results. Therefore, the above Eq. (4-10) can be applied to the strengthening stiffness calculation of UCFST columns.

Table 4-5 Strengthening stiffness comparisons between the formula calculated results and the experimental and finite element results (kN·m^2)

Specimen number	Complete yield curvature		Error	Initial yield curvature		Error
	Experimental result	Calculated result	(%)	Experimental result	Calculated result	(%)
GU-T8-N03	140	153	9.3	141	153	8.5
GU-T8-N06	154	169	9.1	156	169	8.3
GU-T8-N11	182	190	4.4	175	190	8.6
GU-T8-N17	267	251	-6.0	231	251	8.7
GU-T8-N23	313	321	2.6	314	321	2.2
GU-T5-N11	160	159	-0.6	158	159	0.6
GU-T6-N11	179	174	-2.8	168	174	3.6
GU-T10-N11	212	224	5.7	207	224	8.2

Note: Error = (Formula calculated value-test or finite element value)/test or finite element value ×100%.

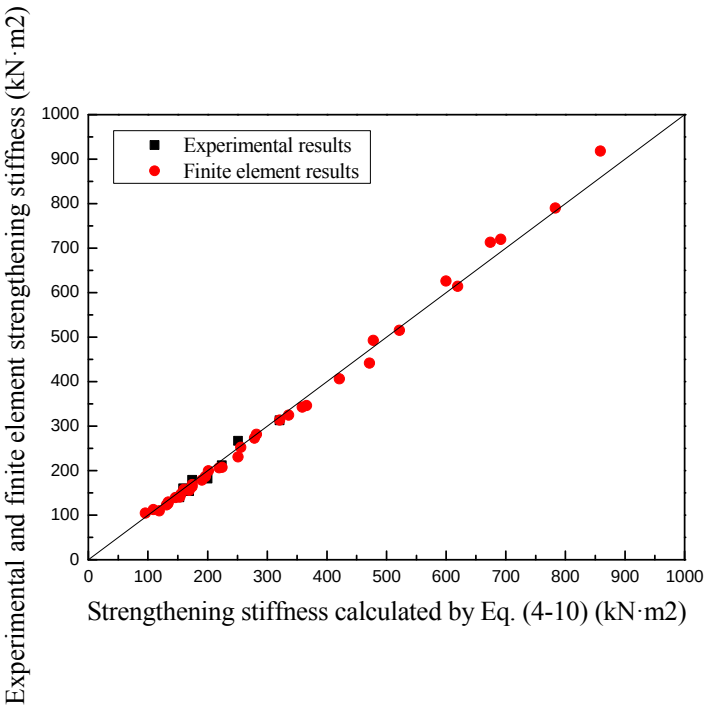

Fig. 4-17 Strengthening stiffness comparisons between results calculated by Eq. (4-10) and the experimental and finite element results

4.6 Verification of skeleton curve calculation model

4.6.1 Comparisons with pseudo-static test results

In this chapter, the elasticity stiffness, yield moment, yield curvature and stiffness of strengthening phase of the proposed tri-line curve model of UCFST columns were compared with the experimental and finite element results, and the error was less than 10%. In order to further verify the tri-line curve model of bending moment-curvature skeleton curve of UCFST columns proposed in this paper, the skeleton curves obtained by the simplified calculation method were compared with those obtained by experiments in Fig. 4-18. It can be seen that the trend and the slope of the curve was basically the same.

Therefore, the calculation model of the bending moment-curvature skeleton curve of UCFST columns presented in this paper was in good agreement with the experimental results, and can reflect the hysteretic behavior of UCFST columns to a certain extent.

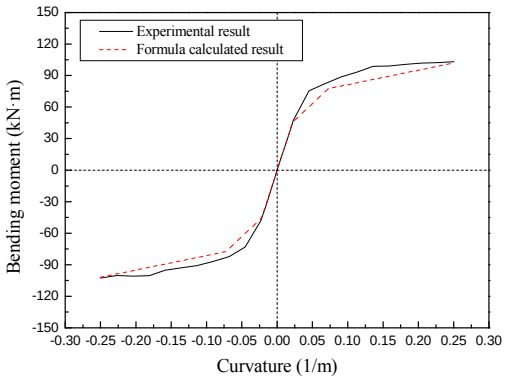

(a)20TGU-T8-N03

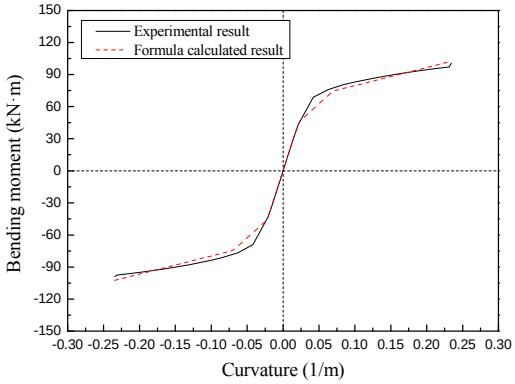

(b)GU-T8-N06

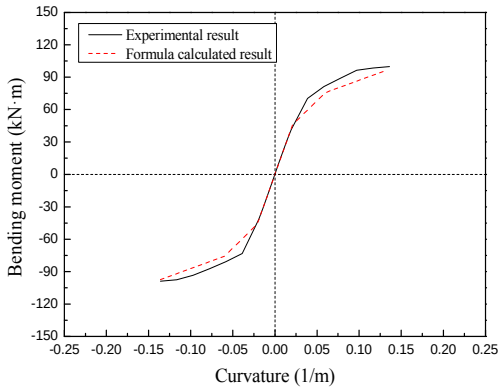

(c)GU-T8-N11

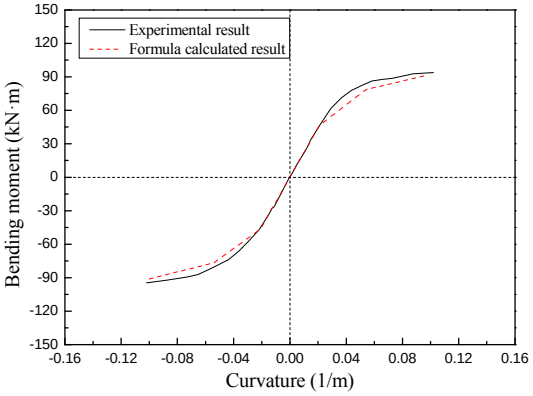

(d)GU-T8-N17

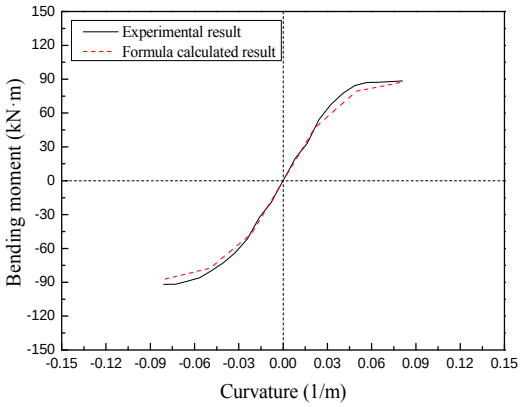

(e)GU-T8-N23

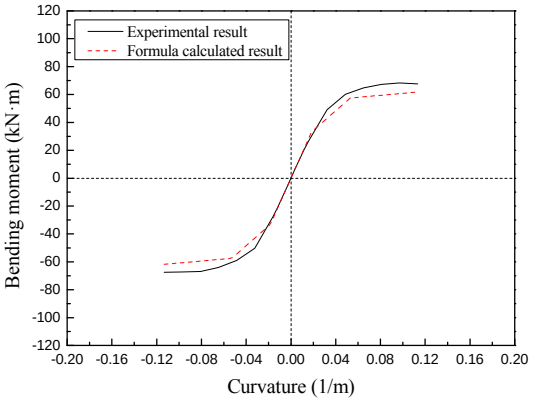

(f)GU-T5-N11

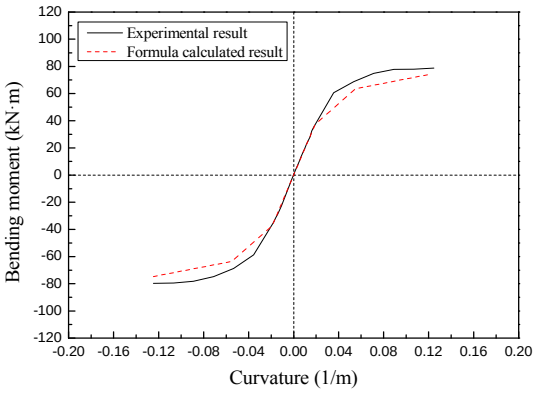

(g)GU-T6-N11

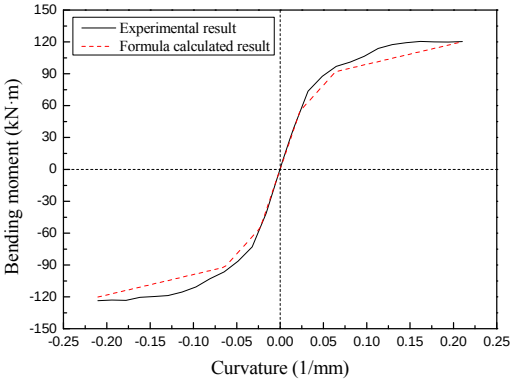

(h)GU-T10-N11

Fig. 4-18 Comparison of skeleton curves between experimental and formula calculation results

4.6.2 Comparisons with finite element analysis results

In order to further verify the accuracy of the simplified calculation formula, the

skeleton curves obtained by the finite element analysis were compared with the results obtained by the simplified calculation method in this paper, using different finite element models established by using the finite element parameters of Chapter 3 (i.e. the outer diameter of steel tube was 120 mm and 160 mm, the axial compression ratio was 0.1, 0.2, 0.3 and 0.4). Thus, the accuracy of the calculation method was verified more accurately. The specific parameters are shown in Table 4-6 and Table 4-7.

The elasticity stiffness, yield moment, yield curvature and stiffness of strengthening phase of the tri-line curve model of bending moment-curvature skeleton of UCFST columns were compared with the finite element results presented Section 4.1-4.6 of this chapter. The error was less than 10%. Fig. 4-19 compares the skeleton curves calculated by simplified calculation method and finite element model. It can be found that the shapes of the two curves basically coincided. Therefore, the accuracy of the skeleton curve model proposed in this paper can be judged, and the bending moment-curvature skeleton curve of UCFST columns can be calculated by the model.

Table 4-6 Parameter table of the model with 120 mm outward diameter steel tube

Length *L*(mm)	1900	Strength of UHPC（MPa）	135
Thickness *t* (mm)	8	Elasticity modulus of UHPC (MPa)	43000
Outside diameter *D* (mm)	120	Yield strength of Steel tube (MPa)	390
Axial compression ratio *n*	0.1、0.2、0.3、0.4	Elasticity modulus of steel tube (MPa)	201000

Table 4-7 Parameter table of the model with 160 mm outward diameter steel tube

Length *L*(mm)	1900	Strength of UHPC（MPa）	135
Thickness *t* (mm)	11	Elasticity modulus of UHPC (MPa)	43000
Outside diameter *D* (mm)	160	Yield strength of Steel tube (MPa)	390
Axial compression ratio *n*	0.1、0.2、0.3、0.4	Elasticity modulus of steel tube (MPa)	201000

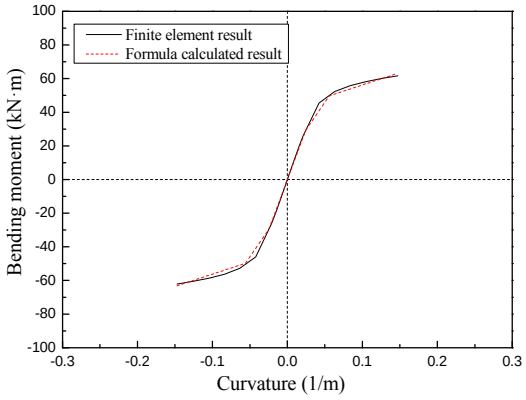

(a)GU-T8-N1

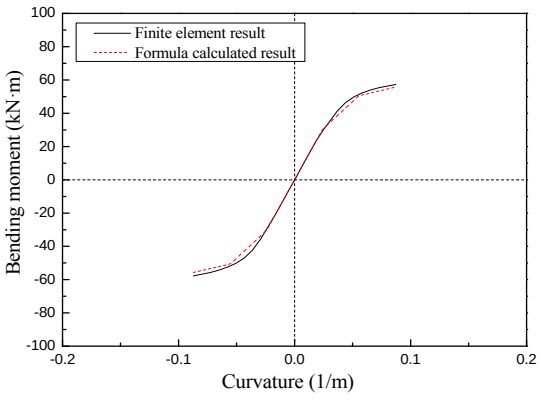

(b)GU-T8-N2

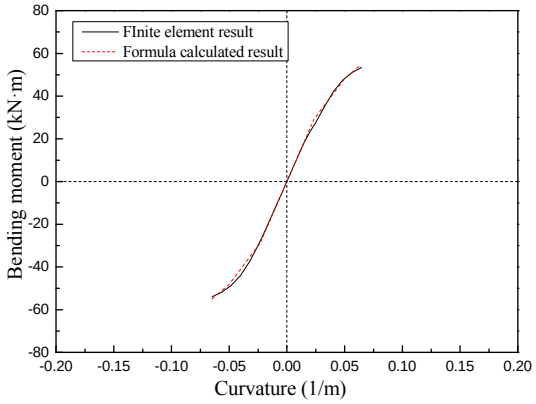

(c)GU-T8-N3

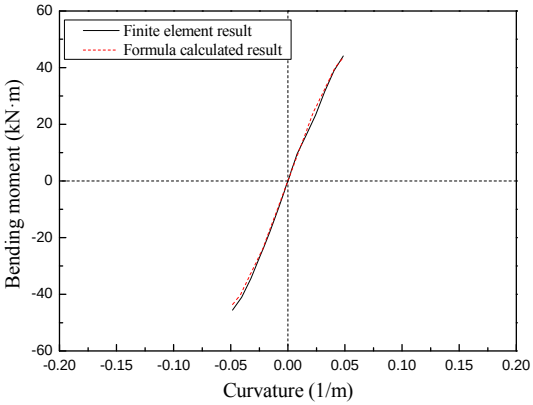

(d)GU-T8-N4

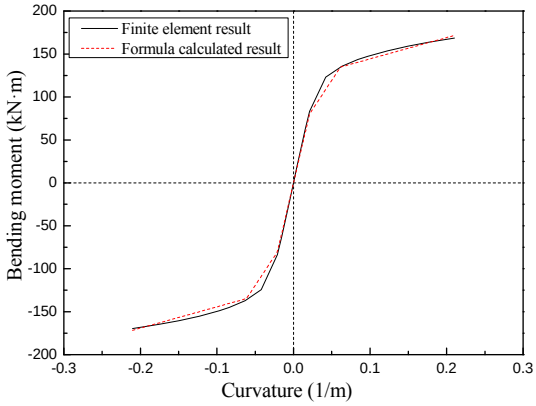

(e)GU-T11-N1

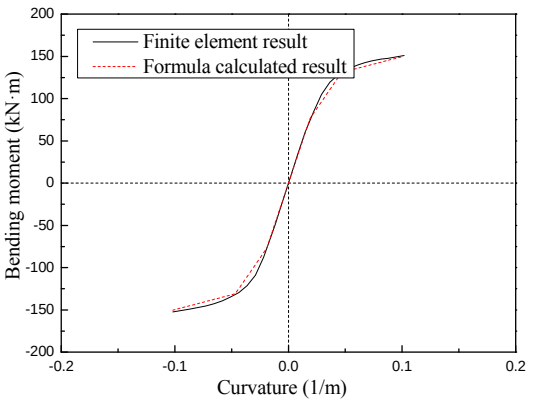

(f)GU-T11-N2

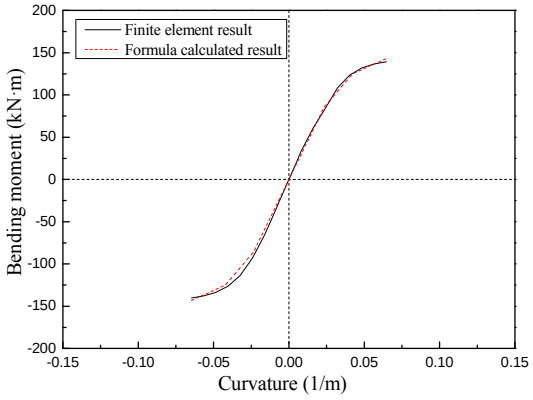

(g)GU-T11-N3

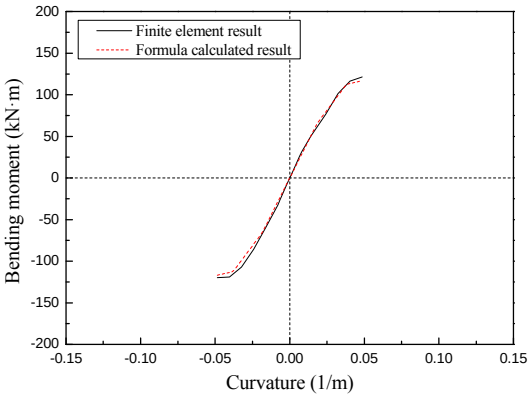

(h)GU-T11-N4

Fig. 4-19 Comparing skeleton curve of finite element method and formula calculation results

4.7 Summary of Chapter 4

The bending moment-curvature skeleton curve of UCFST columns was simulated by using a tri-line model. A simplified formula for calculating the characteristic points of the bending moment-curvature skeleton curve suitable for UCFST columns was derived. The applicability and accuracy of the above tri-line skeleton curve model were verified by comparing with the results of pseudo-static test and finite element analysis. The following conclusions were drawn:

(1) According to the analysis results of Chapter 3 in this paper, considering the influence of the axial compression ratio on the elasticity stiffness, the finite element calculation results were regressed, and the calculation formula for the elasticity stiffness of UCFST columns was determined. Comparing the elasticity stiffness calculated by this formula with that obtained by experiment and finite element method, the error was less than 11%. This shows the accuracy of the elasticity stiffness calculation formula proposed in this paper.

(2) The formulas for calculating the axial force-moment relationship of UCFST columns were fitted with the main parameters of axial compression ratio and steel ratio, and the simplified formulas for calculating the complete yield moment were obtained. Comparing the calculated results with the yield moment obtained by the test and finite element method in this paper, the error was less than 9%. It shows

that the formula proposed in this paper was suitable for calculating the complete yield moment of UCFST columns.

(3) Referring to the yield curvature calculation method of CFST columns, the initial yield moment was determined by statistics, and then the yield curvature calculation formula of UCFST columns was obtained by fitting. Comparing the yield curvature calculated by this formula with that obtained by experiment and finite element method in this paper, the error was less than 9%. It shows that the yield curvature formula proposed in this paper was suitable for calculating the yield curvature of UCFST columns.

(4) The main parameters affecting the stiffness of the strengthening phase were axial compression ratio and steel ratio. Referring to the calculation method of the stiffness of the strengthening phase of the moment-curvature skeleton curve of CFST columns, the simplified calculation formula of the strengthening stiffness of UCFST columns was fitted with axial compression ratio and steel ratio as the main influencing parameters. Compared with the strengthening stiffness obtained by experiment and finite element method, the error of the strengthening stiffness calculated by this formula was less than 10%. It shows that the strengthening stiffness calculation formula proposed in this paper was suitable for calculating the strengthening stiffness of UCFST columns.

(5) By using the simplified formulas for calculating the characteristic points of the moment-curvature skeleton curve of UCFST columns presented in this paper, the calculated results were in good agreement with the experimental and finite element results, and the relative error of the eigenvalues of the skeleton curve was less than 10%. Therefore, the skeleton-curve model can accurately simulate the hysteretic behavior of UCFST columns. It also shows that the moment-curvature skeleton curve proposed in this paper can be applied to practical engineering.

Chapter 5

Conclusions and Recommendations

5.1 Conclusions

In this paper, the hysteretic behavior of bending moment-curvature of UCFST columns subjected to cyclic loading was studied by means of experiment and finite element simulation. As a result, the tri-line moment-curvature skeleton curve suitable for UCFST columns was regressed by referring to the bending moment-curvature hysteretic model of CFST columns. Based on the results of this study, the following conclusions can be drawn:

(1) The hysteretic curves of UCFST columns were full and no pinching, and the moment-curvature skeleton curves did not show deterioration, which indicated that UCFST columns had good seismic behavior.

(2) The test results of eight UCFST columns showed that with the increase of the axial compression ratio, the bending capacity of the specimens increased firstly and then decreased, while the ductility and energy consumption decreased greatly. With the increase of steel ratio, the bending moment and ductility and energy dissipation of the specimens were greatly improved.

(3) Firstly, ABAQUS finite element analysis software was used to analyze the hysteretic behavior of UCFST columns, so as to better understand the working mechanism and failure mode. Secondly, OpenSEES was used to simulate the UCFST columns, and the accuracy of the finite element model was verified by comparing with the experimental results and ABAQUS simulation results. After verification of the test results, the parameters such as axial compression ratio,

steel ratio, steel yield strength and core concrete strength were expanded and supplemented on the basis of the test parameters, and the finite element model was established by OpenSEES to simulate and analyze.

(4) The elasticity stiffness of UCFST columns was mainly affected by steel ratio and concrete strength. Within a certain range, the elasticity stiffness increased in varying degrees with the increase of steel ratio or concrete strength. The elasticity stiffness increased firstly and then decreased with the increase of axial compression ratio. The results showed that steel ratio had the greatest influence on the elastic stiffness of UCFST columns.

(5) The yield moment of UCFST columns was affected by the parameters such as axial compression ratio, steel ratio, steel yield strength and concrete strength. Within a certain range, with the increase of axial compression ratio, the yield moment of UCFST columns showed a trend of firstly rising and then decreasing. With the increase of steel ratio, steel strength or concrete strength, the yield bending moment of UCFST columns increased in varying degrees.

(6) The curvature at the yield moment of UCFST columns was mainly affected by the parameters such as axial compression ratio, steel ratio and steel yield strength. Within a certain range, the yield curvature tended to decrease with the increase of axial compression ratio. With the increase of steel ratio or steel strength, the yield curvature decreased in different extent.

(7) The curvature ductility coefficient of UCFST columns was mainly affected by the parameters such as axial compression ratio, steel ratio and steel yield strength. Within a certain range, the curvature ductility coefficient decreased significantly with the increase of axial compression ratio while other parameters remained unchanged. With the increase of steel ratio or steel strength, the curvature ductility coefficient increased in varying degrees.

(8) It was verified that the calculation method of elasticity stiffness of CFST columns considering reduction of concrete bending stiffness was not suitable for UCFST columns. According to the analysis results of Chapter 3 in this paper, considering

the influence of axial compression ratio on the bending stiffness of the elastic phase, the finite element calculation results were regressed, and a formula for calculating the bending stiffness of the UCFST columns in the elastic phase was established. Comparing the calculated elasticity stiffness with the experimental results and the finite element method, the error was within 10%.

(9) It was verified that the formula of axial force-bending moment of CFST columns was not suitable for UCFST columns. The formula of axial force-bending moment of UCFST columns was fitted with the main parameters of axial compression ratio and steel ratio, and the simplified formula of yield bending moment of UCFST columns was obtained. Comparing the yield moment calculated by this formula with that obtained by the experiment and finite element method in this paper, the error was within 10%.

(10) Referring to the calculation method of yield curvature of CFST columns, the initial yield moment was determined by statistics, and then the yield curvature formula of UCFST columns was obtained by fitting. The yield curvature calculated by this formula was within 10% compared with the yield curvature obtained by the experiment and finite element method in this paper.

(11) Through parameter analysis, the main parameters affecting the stiffness of strengthening phase were the axial compression ratio and steel ratio. Referring to the calculation method of the strengthening stiffness of moment-curvature skeleton curve of CFST columns, the simplified calculation formula of the strengthening stiffness of UCFST columns was fitted by taking the axial compression ratio and steel ratio as the main influencing parameters. Compared with the yield curvature obtained by experiment and finite element method, the error of the strengthening stiffness calculated by this formula was within 10%.

(12) By using the simplified formulas for calculating the characteristic points of UCFST columns moment-curvature skeleton curve presented in this paper, the calculated results were in good agreement with the experimental and finite element results, and the relative error of the eigenvalues of the skeleton curve was

less than 10%. Therefore, the skeleton-curve model can accurately simulate the hysteretic behavior of UCFST columns. It also showed that the moment-curvature skeleton curve proposed in this paper can be applied in practice.

5.2 Recommendations for future research

In this paper, the bending moment-curvature skeleton curve of UCFST columns was preliminarily studied. In order to further understand the hysteretic behavior of UCFST columns, the following aspects can be studied:

(1) Constitutive model of confined concrete was adopted as the core UHPC constitutive model in this paper, and the UHPC constitutive model and loading and unloading rules need to be further studied.

(2) The hysteretic relationship of UCFST columns includes moment-curvature and load-displacement relationship. In this paper, only the moment-curvature hysteretic relationship of UCFST columns was studied, without considering the influence of slenderness ratio. Therefore, the load-displacement hysteretic relationship of UCFST columns needs to be studied accordingly.

(3) In this paper, the bending moment-curvature skeleton curve of UCFST columns was studied only by experiment and finite element method, and the restoring force model of UCFST columns can be further studied by theoretical deduction.

(4) Through the research of UCFST columns in this paper, it was found that thin-walled normal steel tube cannot restrain UHPC very well. Only thicker-walled steel tube can provide enough restraint for UHPC to a certain extent, but the cost of thicker-walled steel pipe is too high. Therefore, UHPC filled high strength steel tube (UCFHST) columns can be formed by replacing normal steel tube with high strength steel tube, and experimental study on this kind of composite structure can be carried out.

References

An, L.H. and Fehling, E. (2017). A review and Analysis of Circular UHPC Filled Steel Tube Columns under Axial Loading. *Structural Engineering & Mechanics*, 62(4): 417-430.

Aziz, O.Q. and Ahmed, G.H. (2012). *Mechanical Properties of Ultra High Performance Concrete (UHPC)*. Proceedings of the 12th International Conference on Recent Advances in Concrete Technology and Sustainability. American Concrete Institute, ACI Special Publication, pp331-346, Prague, Czech Republic.

Birtel, V. and Mark, P. (2006). *Parameterised Finite Element Modelling of RC Beam Shear Failure*. ABAQUS Users' Conference: 95-108.

Bonneau, O. and Pouhn, C. (1996). Reactive Powder Concrete from Theory to Practice. *Concrete International*, 18(4): 47-49.

Cai, S.H. and Di, X.T. (1985). Behaviour and Ultimate Strength of Concrete-Fined Steel Tubular Columns under Eccentric Loading. *Journal of Building Structures*, 6(4):32-42. (in Chinese)

Cai, S.H. and Jiao, Z.S. (1984). Behavior and Ultimate Strength of Short Concrete-Filled Steel Tubular Columns. *Journal of Building Structures*, 5(6): 13-29. (in Chinese)

Chen, B.C., Ji, T. Huang, Q.W., Wu, H.Z., Ding, Q.J., and Zhang, Y.Y. (2014), Review of Research on Ultra‐high Performance Concrete. *Journal of Architecture and Civil Engineering*, 31(3): 1-24. (in Chinese)

Ding, F.X., Zhang, P., Yu, Z.W. and Ou, J.P. (2009). Practical Calculation Method od Axial Force-Moment-Curvature Relationship for Concrete-Filled Circular Steel Tubular Beam-columns. *Journal of Harbin Institute of Technology*, (12): 142-146. (in Chinese)

Du, R.Y. (2014). Research on Ultimate Load-carrying Capacities of Reactive Powder Concrete (RPC) Box Girder and Arch. *Fuzhou: Fuzhou University*. (in Chinese)

Du, R.Y., Huang, Q.W. and Chen, B.C. (2013). Application and Study of Reactive Powder Concrete to Bridge Engineering. *World Bridges*, 41(1): 69-74. (in Chinese)

Fan, L.C. and Zhuo, W.D. (2001). Seismic Design of Bridge Ductility Beijing: *China Communications Publishing*. (in Chinese)

Federal, U.S. (2006). Highway Administration, Material Property Characterization of Ultra-High Performance Concrete. *Publication No. FHWA-HRT-06-103*.

Feng, J.W. (2008). Study on Mechanical Behavior of Reactive Powder Concrete Filled Steel Tubular Columns. *Beijing: Tsinghua University*. (in Chinese)

Fujinaga, T., Matsui, C., Tsuda, K. and Yamaji, K. (1997). *Structural Performance of Concrete Filled Tubular (CFT) Beam-Columns Under Cyclic Load (No. 2) Circular Specimen.* Summaries of Technical Papers of Annual Meeting Architectural Institute of Japan (C-1,Structures III), AIJ: 897-898.

Fujimoto, T., Mukai, A., Nishiyama, I. and Sakino, K. (2014). Behavior of Eccentrically Loaded Concrete-Filled Steel Tubular Columns. *American Society of Civil Engineers*, 130(2):203-212.

Ghafari, E., Costa, H., Julio, E. (2015). Critical Review on Eco-efficient Ultra High Performance Concrete Enhanced with Nano-materials. *Construction and Building Materials*, 101:201-208.

Gu, W.P. and Cai, S.H. (1991). Research on the Behavior and Loading Capacity of Slender Steel Tubular Columns Filled with High-Strength Concrete. *Building Science*, (3):5-10. (in Chinese)

GB/T 31387-2015. *Reactive Powder Concrete*. Beijing: Standards Press of China. (in Chinese)

Guo, J. (20117). Research on Processes and Properties of Alkali-Activated Cement Based Ultra-High Performance Concrete. *Fuzhou: Fuzhou University*. (in Chinese)

Han, L.H. (2004). Concrete Filled Steel Tube Structures. *Beijing: Science Press*. (in Chinese)

Han, L.H. (2004). Concrete Filled Steel Tubular Structure-Theory and Practice. *Beijing: Science Press*. (in Chinese)

Han, L.H., Yang, Y.F. and Tao, Z. (2003). Concrete-Filled Thin-Walled Steel SHS and RHS Beam-Columns Subjected to Cyclic Loading. *Thin-Walled Structures*,

41(9):801–833.

Han, L.H., Yang, Y.F., You, J.T. and Huang, H. (2004). Experimental and Theoretical Studies on the Hysteretic Behavior of Beam-Columns of Concrete-Filled Circular Steel Tubes. *China Journal of Highway and Transport*, 17(3):51-56. (in Chinese)

Li, R.Z., Qin, H. and Zhao, M. (2016). Analysis and Application of the Correlation Curve of Axial Force Bending Moment for the Beam-Columns of Circular Steel Tube Concrete. *Zhejiang Construction*, 33(5): 11-15. (in Chinese)

Liew, J.Y.R. and Xiong, D.X. (2012). Ultra-High Strength Concrete Filled Composite Columns for Multi-Storey Building Construction. *Advances in Structural Engineering*, 15(9): 1487-1504.

Luo, H. (2015). Research on Behavior of Reactive Powder Concrete-Filled Circular Steel Tube Stub Columns under Axial Compression. *Beijing: Beijing Jiaotong University*.

Lv, X.L. and Lu, W.D. (2000). Seismic Behavior of Concrete-filled Rectangular Steel Tubular Columns Under Cyclic Loading. *Journal of Building Structures*, 21(2):2-11. (in Chinese)

Mander, J.B., Priestley, M.J.N. and Park, R. (1988). Theoretical Stress-Strain Model for Confined Concrete. *Journal of Structural Engineering*, 114(8): 1804-1826.

Mazzoni, S., Mc, K.F., Scott, M.H. and Fenves, G. (2004). OpenSEES Users Manual. *PEER, University of California, Berkeley*, 18: 56-57.

Meng, S.Q., Chen, G.Z. (2003). Preliminary Study on Reactive Powder Concrete Filled Steel Tubes. *China Concrete and Cement Products*, (1): 5-8. (in Chinese)

Ministry of Housing and Urban-Rural Development of the People's Republic of China. JGJ/T 101-2015 *Specification for Seismic Test of Buildings*. China Architecture & Building Press. (in Chinese)

National Standards of the People's Republic of China. GB/T 50152-2012 *Standard for Test Method of Concrete Structures*. Beijing. (in Chinese)

National Standards of the People's Republic of China. GB/T228.1-2010 *Metallic Materials Tensile Testing Method at Room Temperature*. Beijing. (in Chinese)

National Standards of the People's Republic of China. GB50017-2014. *Code for Design of Steel Structure*. Beijing: China Planning Press. (in Chinese)

National Standards of the People's Republic of China. GB 50010-2010 *Code for Design of Concrete Structures*. China Architecture & Building Press. (in Chinese)

National Standards of the People's Republic of China. GB 50936-2014 Technical Code for Concrete Filled Steel Tubular Structures. China Architecture & Building Press. (in Chinese)

Ning, C.L. and Duan, Z.D. (2009). Research of Three Nonlinear Beam-Column Element of OpenSEES. Low Temperature Architecture Technology, 31(3):49-52. (in Chinese)

Patel, V.I., Hassanein, M.F., Thai, H.T., Abadi, A., Elchalakani, M. and Bai, Y. (2019). Ultra-High Strength Circular Short CFST Columns: Axisymmetric Analysis, Behaviour and Design. *Engineering Structures*, 179: 268-283.

Philippot, S. and Korb, J.P. (1998). Analysis of Microporsity and Setting of Reactive Powder Concrete by Proton Nuclear Relaxation. *Magnetic Resonance Imaging*, 16:515-518.

Prabha, S.L., Dattaterya, J.K., Neelamegam, M. and Seshagiri R.M.V. (2010). Stress Strain of RPC under Uniaxial Compression. *International Journal of Engineering Science and Technology*, 2(11): 6408-6416.

Qian, J.R., Wang, G. Zhao, Z.Z., and Kang, Z. (2004). Research on Section Moment-Curvature Relationship Curves of Steel Tube Confined High-Strength Concrete Members. *Industrial Construction*, 34(8):70-72. (in Chinese)

Saenz, L.P. (1964). *Discussion of "Equation the Stress-Strain Curve of Concrete," by P. Desayi and S. Krishnan*. In Proceedings of Americon Concrete Institute: 1229-1235.

Sakino, K. and Tomii, M. (1981). Hysteretic Behavior of Concretefilled Square Steel Tubular Beam-Columns Failed in Flexure.*Transactions of the Japan Concrete Institute*, 3: 439-446.

Schmidt, M., Fehling, E. (2005). Ultra-high-performance Concrete: Research,

Development and Application in Europe. *ACI Special Publication*, 228: 51-78.

Serras, D.N., Skalomenos, K.A., Hatzigeorgiou, G.D. and Beskos, D.E. (2016). Modeling of Circular Concrete-Filled Steel Tubes Subjected to Cyclic Lateral Loading. *Structures*, 8: 75-93.

Shen, J.M. (1993). Finite Element Analysis of Reinforced Concrete and Limit Analysis of Plates and Shells. *Beijing: Tsinghua University Press*.

Shi, Y.Z., Wang, D.H. Li, Q.C., Jia, Y.Z. and Xiao, Q. (2011). On the Influence of Steel Fiber Volume Fraction on Mechanical Properties of Reactive Powder Concrete. *Journal of Experimental Mechanics*, 26(3): 254-260. (in Chinese)

Wakabayashi, M. (1988). *Review of Research on Conerete Filled Steel Tubular Structures in Japan*. Proeeedings of the International Specialty Conference on Concerte Filled Fteel Tubular Structuer:5-11.

Wang, J.T., Sun, Q. and Li, J.X. (2019). Experimental Study on Seismic Behavior of High-Strength Circular Concrete Filled Thin-Walled Steel Tubular Columns. *Engineering Structures*, 182: 403-415.

Wang, J.T., Sun, Q., Wu, X.H. and Wu, Y.C. (2019). Experimental and Analytical Investigation on Seismic Behavior of Q690 Circular High‐Strength Concrete‐Filled Thin‐Walled Steel Tubular Columns. *Struct Design Tall Spec Build.*, 28: 1-19.

Wang, Y. (2013). Research on the Mechanical Performance of Concrete Filled Circular Steel Piers to Earthquake Action. *Xi'an: Chang'an University*.

Wang, Z. and Zhen, Y.H. (2000). Research on Hysteretic Behavior of High Strength Concrete Filled Steel Tubular Member under Compression and Bending. *Earthquake Engineering and Engineering Vibration*, 20(4):51-55. (in Chinese)

Wei, J.D. (2011). Long-span Bridge. *Zhengzhou: Zhengzhou University Press*. (in Chinese)

Wu, Y.H. and Lin, Z.Y. (2005). Experimental Study of Behavior on RPC Filled Steel Tubular Stub Columns under Axial Compression. *China Journal of Highway and Transport*, 18(1): 57-62. (in Chinese)

Xie, L.L., Ye, X.G., Zhong, X. and Jiang, Q. (2012). Parameter Research on Numerical Analysis of Low-Cyclic Loading Test of RC Columns. China Civil Engineering Journal, 45(S1): 273-277. (in Chinese)

Xie, X. (2005). Seismic Response and Earthquakes Resistant Design of Bridges. Beijing: *China Communications Publishing*. (in Chinese)

Yan, G.J. (2005). Study on Failure Criterion and Constitutive Relation of 200 MPa Reactive Powder Concrete (RPC200). *Beijing: Beijing Jiaotong University*.

Yan, G.J. and Yan, G.P. (2007). Experimental Study on Two-Way Tension-Compression Strength for Reactive Powder Concrete. China Safety Science Journal, 17(03): 162-165+1. (in Chinese)

Yan, W. (2015). Sectional Hysteretic Model of Concrete-Filled Circular Steel Tubes. *Harbin: Harbin Institute of Technology*.

Yan, Z.G., Zhang, W.Q. and An, M.Z. (2011). Analysis of Ultimate Loading Capacity for Circular RPC Filled Steel Tube Stub Columns under Axial Compression. *Journal of Beijing University of Technology*, 37(3): 361-367. (in Chinese)

Yang, J. (2013). Finite Element Analysis of Axially Loaded RPC Filled Long Circular Steel Tube Columns. *Beijing: Beijing Jiaotong University*.

Yang, W.S. (2003). Study on Mechanical Properties and Ultimate Bearing Capacity of Reactive Powder Concrete Filled Steel Tubes. *Changsha: Hunan University*. (in Chinese)

Yao, L.Y. (2005). Researches on Behavior of Eccentrically Loaded Stub Column and Axially Compressed Slender Column with RPC-Filled Circular Steel Tube. *Fuzhou: Fuzhou University*. (in Chinese)

Yao, Y. Li, G.Z. Gao, C.Y., Cao, Y. and Chen, L. (2015). Discussion on Design Value Selection of Axial Compressive Strength of Over C80 Concrete. Coal Engineering, 47(1):110-111. (in Chinese)

You, J.T. and Han, L.H. (2005). Experimental Study on High-Performance Concrete Filled Steel Tubular Column Subjected to Cyclic Loading. *Earthquake Engineering and Engineering Vibration*, 25(3):98-103. (in Chinese)

Yuan, H.H., Wu, Q.X., Chen, B.C. and Lv, Y.H. (2016). Aseismic Performance Test and Fem Analysis of Uniform Sectional CFST Lattice Column with Flat Lacing Tubes. *Engineering Mechanics*, (10): 226-235. (in Chinese)

Zdeb, T. and Sliwinski, J. (2011). The Influence of Selected Material and Technological Factors on Mechanical Properties and Microstructure of Reactive Powder Concrete (RPC). *Archives of Civil Engineering*, 57(2):227-246.

Zeng, J.X. (2015). Researches on Behavior of Eccentrically Loaded Slender Column of Circular Steel Tube RPC. *Fuzhou: Fuzhou University*. (in Chinese)

Zhang, J. (2003). Experimental Investigation on Behavior of Reactive Powder Concrete Filled Steel Stub-Columns. *Fuzhou: Fuzhou University*. (in Chinese)

Zhong, S.T. (2001). Application and Development in China of Concrete Filled Steel Tubular Structure. *Architecture Technology*, 32(2): 80-82. (in Chinese)

Zhong, S.T. (2006). Unified Theory of Concrete Filled Steel Tubular Structure: Research and Application. *Beijing: Tsinghua University Press.* (in Chinese)

Appendix I

(1) Load-displacement hysteresis curves of UCFST columns with different axial compression ratios

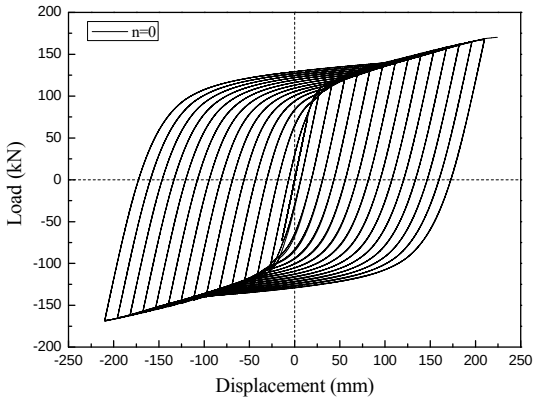

(a) GU-T8-N0

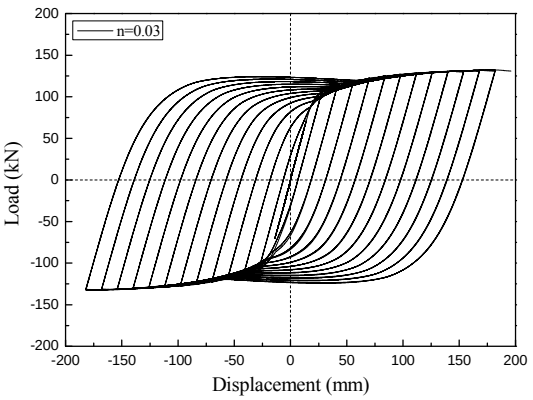

(b) GU-T6-N03

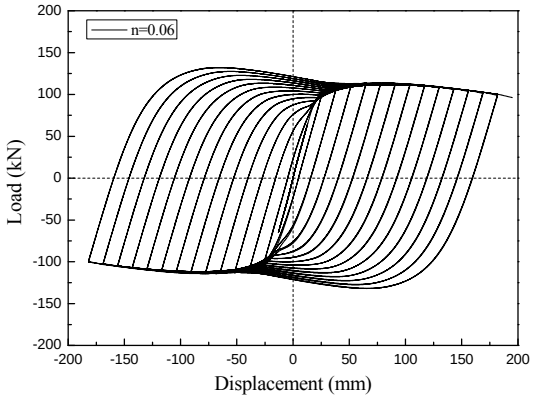

(c) GU-T6-N06

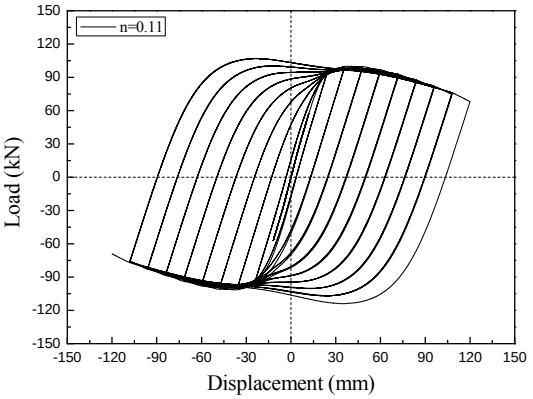

(d) GU-T8-N11

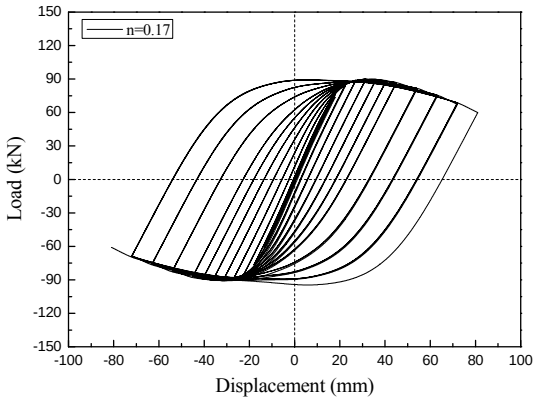

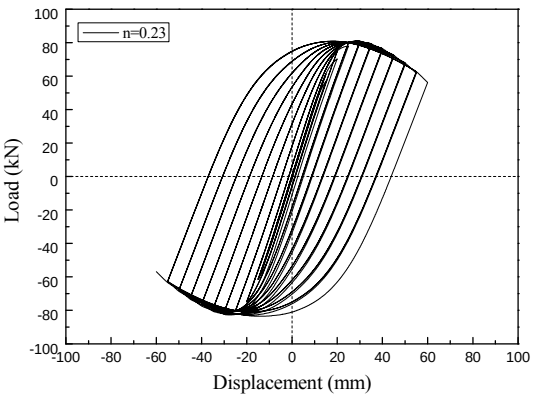

(e) GU-T8-N17

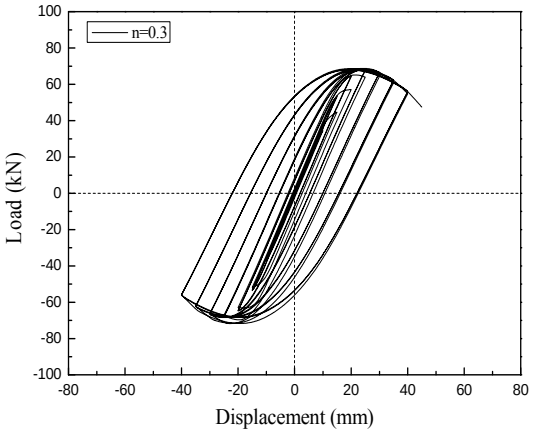

(f) GU-T8-N23

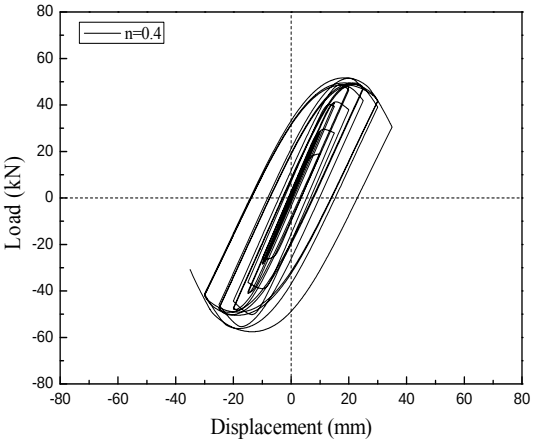

(g) GU-T8-N3

(h) GU-T8-N4

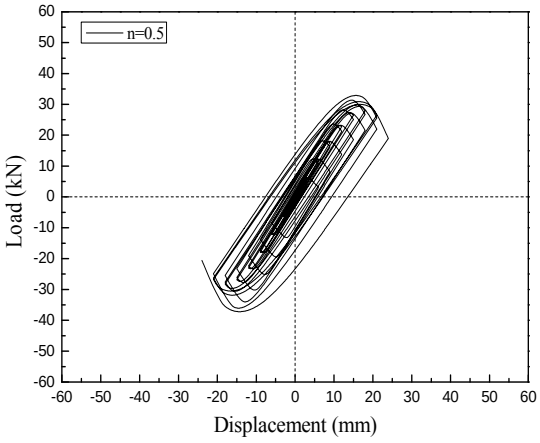

(i) GU-T8-N5

(2) Load-displacement hysteresis curves of UCFST columns with different steel content

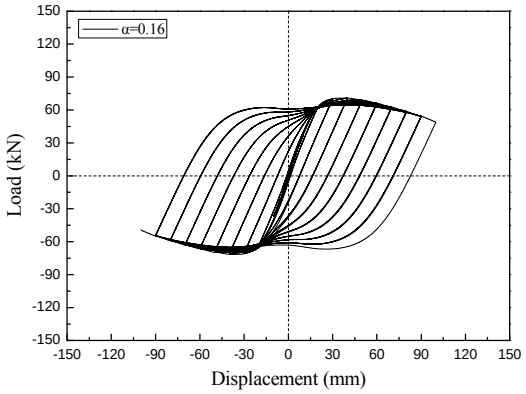

(a) GU-T5-N11

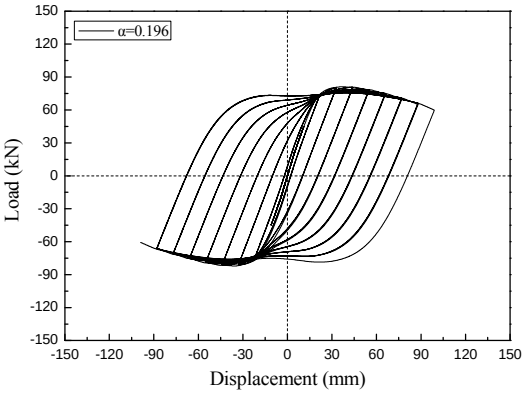

(b) GU-T6-N11

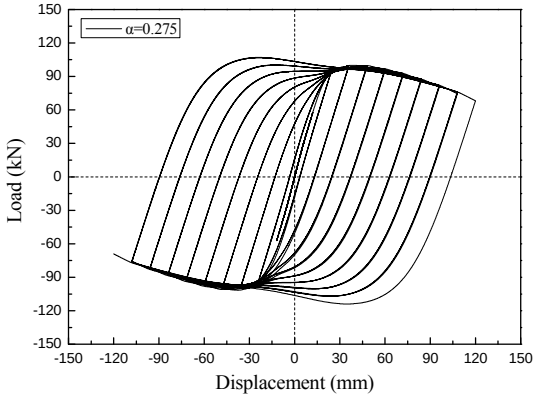

(c) GU-T8-N11

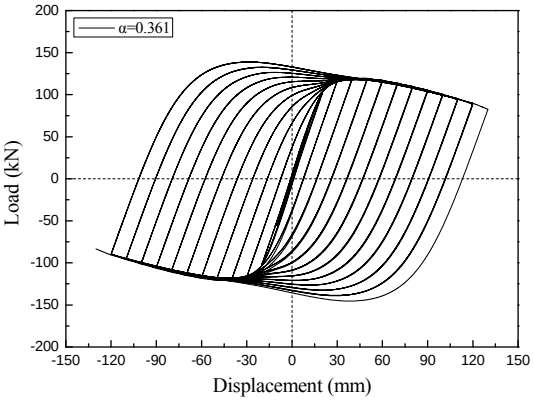

(d) GU-T10-N11

(3) Load-displacement hysteresis curves of UCFST columns with different steel yield strength

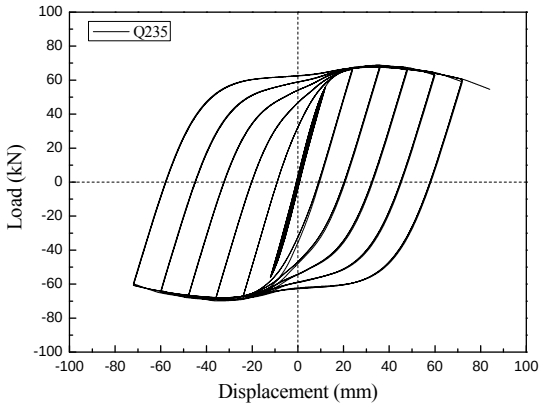

(a) GU-T8-N11

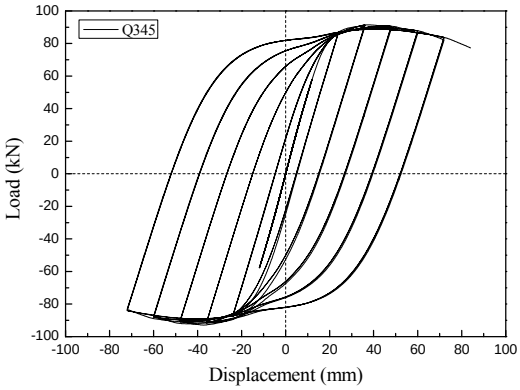

(b) GU-T8-N11

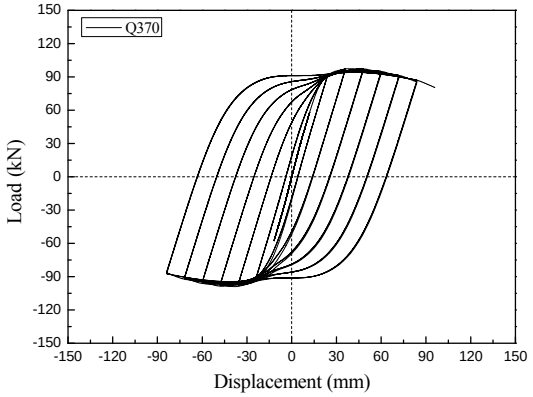

(c) GU-T8-N11

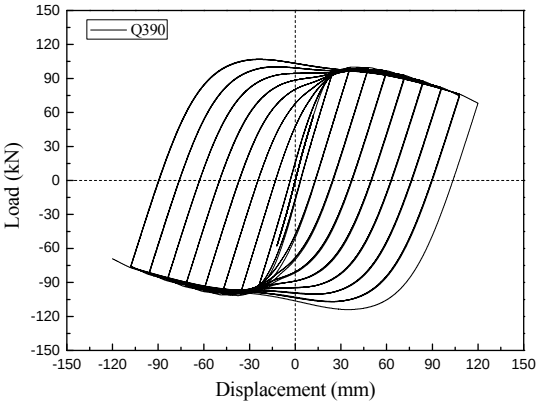

(d) GU-T8-N11

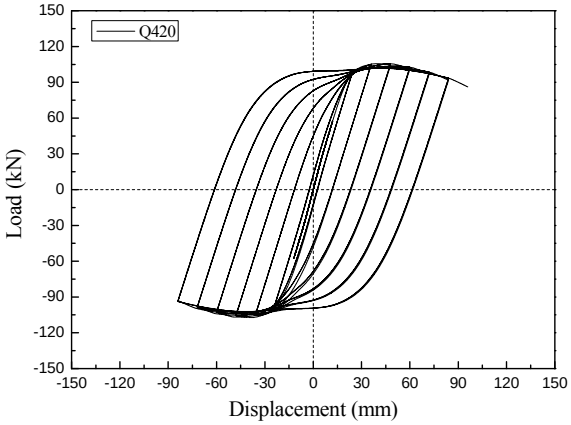

(e) GU-T8-N11

(4) Load-displacement hysteretic curves of UCFST columns with different core concrete strengths

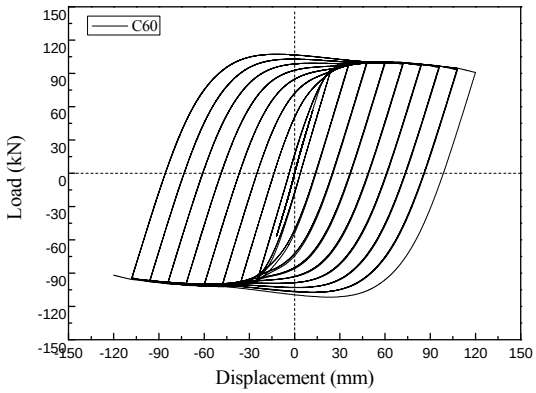

(a) GU-T8-N11

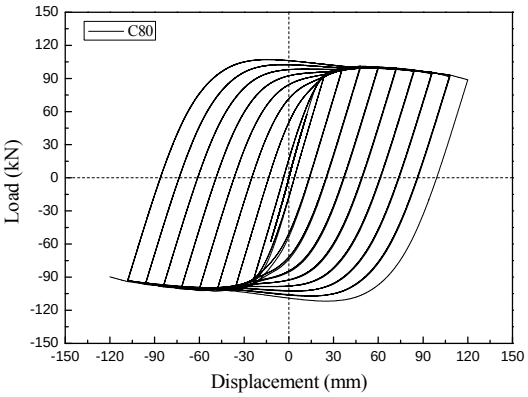

(b) GU-T8-N11

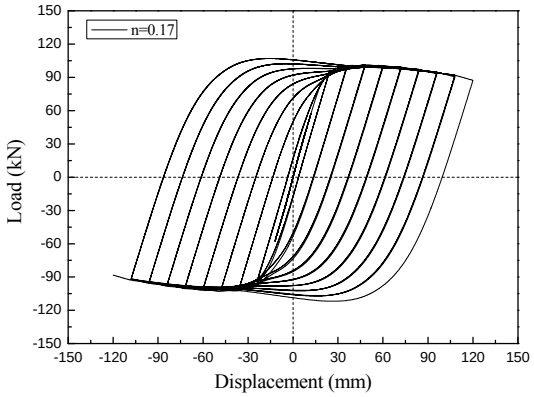

(c) GU-T8-N11

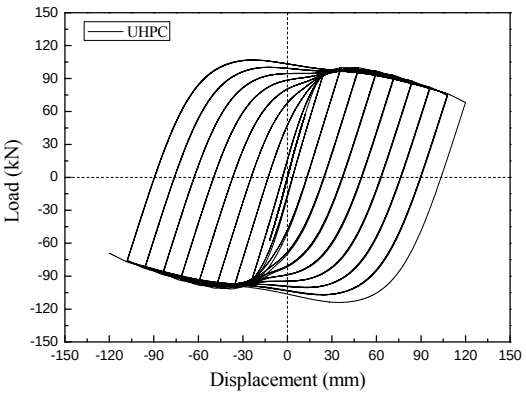

(d) GU-T10-N11

Acknowledgments

I am very grateful to Modena University and Fuzhou University for giving me this opportunity to carry out the joint training and study of the two universities. I would like to thank Prof. Angelo Marcello Tarantino and Prof. Alberto Muscio of Modena University and Prof. Bruno Briseghella of Fuzhou University for their guidance and help during my joint study. I would also like to thank Prof. Wei Jiangang, my mentor in China, for his support and encouragement to my joint training. Thank all the professors and teachers of Modena University for their help during my one year study in Modena. One year's study in Italy has made me see the cultural differences and similarities between different countries. I am very grateful to have this international learning experience, which will become the most valuable wealth in my life journey.

I also want to thank my parents and brother for their care and concern. And I want to thank my boyfriend for his encouragement and undersdanding. Their encouragements have kept me going in my doctoral career in these years.

Finally, I wish that Modena University and Fuzhou University can get better and better, and the further cooperation and exchanges be more pleasant.

Publications List

Journal Papers:

[1] Wei, J. G., **Zhou, J.**, Luo, X., et al. Experimental Study on Quasi-Static Behavior of Ultra-High Strength Concrete Filled High Strengh Steel Tubular Columns [J]. Engineering Mechanics. doi: 10.6052/j.issn.1000-4750.2020.06.0414. (in Chinese)

[2] Wei, J. G., **Zhou, J.**, Yang, Y., et al. Quasi-static Test on Ultra-High Strength Concrete Filled Steel Tube Columns [J]. Journal of Architecture and Civil Engineering, 2020, 37(5): 62-69. (in Chinese)

[3] Wei, J. G., **Zhou, J.**, Huang, J. N., et al. Experimental Study on the Cyclic Behavior of Ultra High Performance Concrete (UHPC)-Filled Steel Tube Beam-Columns [J]. Advances in Structural Engineering, 2020, 23(5):969-978.

[4] Chen, B. C., Wei, J. G., **Zhou, J.**, et al. App;ication of Concrete-Filled Steel Tube Arch Bridges in China: Current Status and Propects [J]. China Civil Engineering Journal, 2017, 50(6): 50-61. (in Chinese)

[5] Yang, Y., **Zhou, J.**, Wei, J. G., et al. Experimental Study on the Compression of Concrete Filled Steel Ttubular Latticed Columns with Variable Cross Section [J]. Steel and Composite Structures, 2016, 22(3): 663-675.

Conference Papers:

[1] Wei, J. G., **Zhou, J.**, Wu, Q. X., et al. Study on Bearing Capacity of Concrete-Filled Steel Tubular Composite Columns at Ultimate Service State [C]. The 8th International Conference of Asia Concrete Federation, Fuzhou, China, 4-7 November 2018, pp. 911-917.

[2] **Zhou, J.**, Wei, J. G., Huang, L., et al. Experimental Study on the Compression of Variable Concrete Filled Steel Tubular Laced Columns [C]. The 14th International Symposium on Structural Engineering, Beijing, China, 12-15 October 2016, pp. 1218-1223.

[3] Wei, J. G., **Zhou, J.**,Liu, J. P., et al. Application of Concrete-Filled Steel Tube Arch Bridges in China [C]. The 8th International Conference on Arch Bridges, Wroclaw, Poland, 5-7 October 2016, pp. 468-471.